

INVESTIGATION OF THE NEAR SURFACE MECHANICAL
BEHAVIOR OF SINGLE CRYSTAL ZnO BY
NANOINDENTATION

By

MATTHEW JOSEPH KLOPFSTEIN

Bachelor of Science
Mechanical Engineering
The Ohio State University
Columbus, OH
1991

Master of Arts
Economics
The Ohio State University
Columbus, OH
1992

Master of Science
Mechanical Engineering
Oklahoma State University
Stillwater, OK
1997

Submitted to the Faculty of the
Graduate College of the
Oklahoma State University
in partial fulfillment of
the requirements for
the Degree of
DOCTOR OF PHILOSOPHY
December, 2004

INVESTIGATION OF THE NEAR SURFACE MECHANICAL
BEHAVIOR OF SINGLE CRYSTAL ZnO BY
NANOINDENTATION

Thesis Approved:

Don A. Lucca

Thesis Advisor

B. E. Dine

William

James P. Winkler

A. J. S. S.

Dean of the Graduate College

ACKNOWLEDGMENTS

I would like to thank my advisor, Prof. D. A. Lucca for his encouragement, patience, guidance and assistance. I would also like to thank my committee members, Prof. E. A. Misawa, Prof. C. E. Price and Prof. J. P. Wicksted for their valuable comments and suggestions.

The financial support of the Division of Design, Manufacture and Industrial Innovation of the National Science Foundation, the Oklahoma Center for the Advancement of Science and Technology, and the Distinguished Graduate Fellowship program (Col. Tom J. Cunningham) is gratefully acknowledged.

The assistance and support of Mr. G. Cantwell and Mr. B. Haskins of Eagle-Picher Research Laboratory is gratefully acknowledged. The assistance of Dr. M. Nastasi, Dr. T. Hoechbauer, and Dr. A. Misra of Los Alamos National Laboratory is also gratefully acknowledged.

I would like to thank my colleagues, Mr. R. Ghisleni, Mr. O. Mejia and Dr. D. Hamby for their help and valuable suggestions.

Finally, I would like to thank my parents for their continuing support and encouragement.

TABLE OF CONTENTS

1	Introduction	1
2	Background	4
2.1	Properties and subsurface damage of ZnO	5
2.1.1	Assessment of subsurface damage in polished ZnO by ion channeling	7
2.2	Nanoindentation studies	9
2.2.1	Elastic modulus and hardness	10
2.2.2	Onset of plasticity — pop-in	19
2.2.3	Indentation size effect	20
2.3	Photoplastic effect	22
2.4	Electrical property changes with the presence of dislocations	24
2.5	Scanning Kelvin probe microscopy	25
3	Experimental	33
3.1	Sample preparation	33
3.2	Nanoindentation	35
3.3	Scanning Kelvin probe microscopy	37
3.4	Sample preparation for transmission electron microscopy	38
4	Results and Discussion	39
4.1	Effects of surface preparation on the near surface mechanical behavior	39
4.1.1	Comparison of hardness, elastic modulus, and pop-in	39
4.1.2	Transmission electron microscopy of prepared surfaces	44
4.2	Variation of near surface mechanical behavior with crystallographic orientation	45
4.3	Effects of illumination on the near surface mechanical behavior	48
4.4	Use of scanning Kelvin probe microscopy to observe indentation dislocation rosettes	52

5	Conclusions and Future Work	60
5.1	Conclusions	60
5.2	Proposed future work	62
	Bibliography	63
A	Determination of Area Function and Instrument Compliance for Nanoindentation	73
B	Indentation of a Transversely Isotropic Piezoelectric Halfspace	76
B.1	Development of equations	76
B.1.1	Indentation with a conducting conical indenter	83
B.1.2	Indentation with an insulating conical indenter	84
B.2	Summary of differences	85

LIST OF FIGURES

2.1	Photograph of ball and stick model of ZnO looking in the $\langle 10\bar{1}0 \rangle$ direction.	5
2.2	Photograph of ball and stick model of ZnO looking in the $\langle 11\bar{2}0 \rangle$ direction.	5
2.3	Photograph of ball and stick model of ZnO looking along the $\langle 0001 \rangle$ direction. . . .	6
2.4	Schematic diagram of the Berkovich indenter (left) and an AFM image of a Berkovich indenter (right).	9
2.5	Photograph of nanoindentation system used in the study. Close-up shows the force transducer with an indenter mounted to it.	10
2.6	Idealized load vs. displacement plot showing the unloading slope at the maximum depth, S and the contact depth, h_c	10
2.7	Schematic diagram of various depth definitions. (a) shows the indenter under load and (b) shows the surface after the indenter has been removed.	11
2.8	ϵ values for various indenter geometries.	11
2.9	Schematic diagram of indentation of a elastic half-space by an axisymmetric indenter. . . .	14
2.10	Schematic diagram of conical indenter under load.	15
2.11	Sudden increase in depth at a given load, “pop-in”, observed in the indentation of (001)GaAs. From Leipner et al. [53].	21
2.12	Example of indentation size effect in the indentation of (001)Ag/Au layered structure. The Berkovich indenter was aligned such that one of the edges of the triangular impression was in the $[110]$ direction or $[100]$ direction. From Ma and Clarke [56]. . .	21
2.13	Orientation of samples for bulk compression tests. zincblende samples are oriented for (111) slip (left) and wurtzite samples are oriented for either (0001) slip (left) or $\{10\bar{1}0\}$ slip (right). After Osip’yan et al. [21].	23
2.14	Schematic diagram of method of scanning Kelvin probe microscopy. The left part of figure shows the first pass of the probe to acquire the topography and the right part of figure shows the probe’s second pass to acquire the surface potential. After Bhushan and Goldade [72].	26

2.15	Energy band diagram for a metallic probe near n -type semiconductor separated by an insulating air gap. After Sze [74].	27
2.16	Schematic diagram of spatial dependence of potential around a dislocation. After Read [77].	28
2.17	Effect of above band gap illumination on the band structure of the near surface of an n -type semiconductor. (a) shows the band structure in darkness with surface states causing upward band bending. (b) shows the diffusion of photo-generated carriers to the surface. From Weaver and Wickramasinghe [75].	31
2.18	Schematic diagram of the time-dependent surface photovoltage response. After Bal- estra et al. [86].	32
3.1	Atomic force microscopy image of chemomechanical polished (0001)ZnO with lateral dimensions $5\text{ }\mu\text{m} \times 5\text{ }\mu\text{m}$ and vertical dimension of 50 nm. The surface roughness is about 0.3 nm rms.	35
3.2	Single loading-unloading sequence for small indentations (left) and multiple loading- unloading sequence for larger indentations (right).	36
3.3	Spectrum of light used for photoplastic and surface photovoltage experiments.	36
3.4	Schematic diagram of indentation pattern for indentations performed in darkness and with sample illumination. Typical spacing between indentations was $20\text{ }\mu\text{m}$	37
4.1	Load-depth curves obtained for chemomechanical polished (black circles) and etched (gray circles) (0001) surfaces.	40
4.2	Two neighboring indentations made in chemomechanical polished (0001)ZnO. The first indentation (black circles) exhibited pop-in whereas the second (gray circles) did not.	42
4.3	Load-depth curves for (0001) surfaces prepared by $1\text{ }\mu\text{m}$ mechanical polishing (gray circles) and chemomechanical polishing (black circles).	42
4.4	Hardness for (0001) surfaces with different surface preparations.	43
4.5	Cross-sectional TEM image of chemomechanical polished (0001)ZnO.	45
4.6	Cross-sectional TEM image of $1/4\text{ }\mu\text{m}$ mechanical polished (0001)ZnO. Dislocations extend approximately 80 nm below the surface.	45
4.7	Comparison of hardness for chemomechanical polished (0001) and (000 $\bar{1}$) surfaces.	46
4.8	Comparison of load-depth curves for chemomechanical polished (0001) and $\{10\bar{1}0\}$ surfaces.	47

4.9	Load-depth curves for chemomechanical polished (0001) , $\{10\bar{1}0\}$ and $\{11\bar{2}0\}$ surfaces.	47
4.10	Hardness for (0001) and $\{10\bar{1}0\}$ surfaces.	48
4.11	Comparison of indentations performed in etched $(0001)\text{ZnO}$ with illumination and in darkness showing the load at pop-in (a) in darkness and (b) with illumination. . . .	49
4.12	Hardness as a function of contact depth for etched $(0001)\text{ZnO}$ with sample illumination (circles) and in darkness (squares). Error bars denote the minimum and maximum of the data.	50
4.13	Comparison of indentations performed in chemomechanical polished $\{10\bar{1}0\}\text{ZnO}$ with illumination and in darkness showing the load at pop-in (a) in darkness and (b) with illumination.	51
4.14	Hardness as a function of contact depth for chemomechanical polished $\{10\bar{1}0\}\text{ZnO}$ with sample illumination (circles) and in darkness (squares). Error bars denote the minimum and maximum of the data.	51
4.15	Topography (top figure) and contact potential difference (bottom figure) of a $(000\bar{1})\text{ZnO}$ indented surface measured in darkness. The location of the indentation is shown in the contact potential difference figure by the white triangle.	53
4.16	Topography (top figure) and contact potential difference (bottom figure) of a $(000\bar{1})\text{ZnO}$ indented surface measured with illumination. The location of the indentation is shown in the contact potential difference figure by the white triangle.	53
4.17	Schematic diagram of some planes in hexagonal material. After Honeycombe [20]. .	54
4.18	Length of longest rosette arm vs. the square root of the maximum load of indentation minus the average load a pop-in on $(000\bar{1})\text{ZnO}$	55
4.19	Schematic diagram of the approximate location of the scan line that was measured repeatedly throughout time-dependent surface photovoltage experiment.	56
4.20	Measured contact potential difference in regions inside the rosette arm and outside the rosette arm as a function of the time after the sample was illuminated.	57
4.21	Simplified band structure diagram for the area outside the rosette. (a) shows the band structure in darkness and (b) with illumination. (c) shows the changes in the contact potential difference caused by the illumination.	58
4.22	Simplified band structure diagram for the area inside the rosette. (a) shows the band structure in darkness and (b) with illumination. (c) shows the changes in the contact potential difference caused by the illumination.	59

A.1 Total compliance minus frame compliance (0.002 nm/ μ N) vs. $1/\sqrt{A}$	75
--	----

LIST OF TABLES

2.1	Comparison of microhardness for different surfaces of ZnO. After Regel et al. [24]. . .	6
2.2	Elastic stiffness constants of ZnO at room temperature obtained by ultrasonic pulse technique. After Bateman [30].	8
2.3	Piezoelectric and dielectric constants of ZnO at room temperature obtained by resonance-antiresonance method. After Kobiakov [32].	8
2.4	Damage depth and equivalent amorphous layer for polished ZnO obtained by ion channeling. After Lucca et al. [19].	8
2.5	Elastic moduli in the three directions of indentation used in this study.	13
2.6	Indentation modulus, M_s , for indentation of {0001} surface of ZnO with a conical or spherical indenter. The range of values given for the case of an anisotropic piezoelectric half-space is based on different values for the elastic and piezoelectric properties. . .	20
3.1	Major impurities in SCVT ZnO as measured by GDMS [88].	34
4.1	Indentation modulus of samples at a depth of 150 nm for (0001)ZnO with various surface preparations.	44
B.1	Differences in the terms m_2 and m_3 of Giannakopoulos [111] and this work.	86

Chapter 1

Introduction

“Information of dislocations and plasticity in ZnO is surprising sparse, especially given that sizable ZnO single crystals are now available. Detailed studies on ZnO would be most welcome.”

— T. E. Mitchell and A. H. Heuer [1]

An understanding of a material’s response to mechanical loading (its mechanical behavior) is of fundamental importance. This understanding not only determines the suitability of a material for a given technological application but also provides insight into the material’s deformation processes such as active slip systems, ease of cross-slip, or critical resolved shear stress. A material’s mechanical behavior in the near surface can vary significantly from its bulk behavior. The near surface region of semiconductors is becoming increasingly important as device sizes get smaller and surface behavior becomes more dominant.

ZnO is a wide bandgap semiconductor which has potential uses such as short wavelength (blue-UV) LEDs and lasers and high power, high frequency electronic devices [2]. Although GaN-based devices currently dominate the short wavelength LED market, single crystal bulk ZnO is being pursued as a substrate material for both homoepitaxial films and heteroepitaxial GaN-based films [3–5]. Single crystal ZnO has also been used in Schottky diodes that were shown to be very resistant to proton irradiation [6] making them suitable for use in low-earth orbit. Polycrystalline ZnO films have been demonstrated for uses such as surface acoustic wave [7] and thin film bulk acoustic wave [8] filters, thin film transparent transistors [9], transparent contact electrodes for InGaN-based LEDs [10] and amorphous silicon solar cells [11], UV photodiodes [12] and heterojunction LEDs [13].

Although the opto-electronic properties of bulk ZnO have been vigorously studied [14–18], the mechanical behavior has not received much attention [1]. The objective of this work is to investigate

the near surface mechanical behavior of ZnO using nanoindentation. The near surface mechanical behavior includes the elastic modulus, hardness, the onset of yielding (“pop-in”) and changes in hardness as a function of the depth (indentation size effect).

Objectives

- Study the effects of surface preparation on the near surface mechanical behavior.

The effect of surface preparation on hardness is well known for many materials. There have been no previous studies on the effects of surface preparation on the near surface mechanical behavior of ZnO. In the present study surface preparations for the (0001) surface including chemical etching, chemomechanical polishing, and mechanical polishing with $1/4\ \mu\text{m}$ and $1\ \mu\text{m}$ diamond abrasives were investigated. Based on previous ion channeling studies of similar surfaces [19], these surface preparations will provide a range of near surface damage.

- Study the variation of the near surface mechanical behavior with crystallographic orientation.

For many hexagonal metals, slip on the {0001} planes is easier than on other planes [20]. Conditions favorable for slip on the {0001} planes can be achieved by selection of the indentation plane. By indenting on the $\{10\bar{1}0\}$ or $\{11\bar{2}0\}$ planes, slip should principally occur on the {0001} planes because these planes are perpendicular to the indentation surface. Chemomechanical polished (0001), (000 $\bar{1}$), $\{10\bar{1}0\}$ and $\{11\bar{2}0\}$ surfaces were studied to measure differences in the near surface mechanical behavior.

- Study the effect of illumination on the near surface mechanical behavior.

Illumination has been shown to change the flow stress of bulk ZnO [21] and hardness in the near surface of ZnSe [22] as measured by nanoindentation. The near surface hardness with sample illumination and in darkness was studied for etched (0001)ZnO and chemomechanical polished $\{10\bar{1}0\}$ ZnO.

- Demonstrate the use of scanning Kelvin probe microscopy to observe indentation dislocation rosettes.

Indentation followed by chemical etching has long been used to study the plasticity of single crystals. Etch pits of dislocations around the indentation form a pattern or

“rosette” which provides information about the slip systems of the material. Other techniques to observe indentation dislocation rosettes include plan view and cross-sectional transmission electron microscopy and cathodoluminescence. In the present study scanning Kelvin probe microscopy with sample illumination by a broadband light source was used to observe indentation rosettes in chemomechanical polished and etched $\{0001\}\text{ZnO}$.

The next chapter provides background information on the physical properties and previous studies of ZnO. In addition, the analysis of nanoindentation and the general technique of scanning Kelvin probe microscopy are presented. Chapter 3 presents experimental details of sample preparation, nanoindentation, and scanning Kelvin probe microscopy. In Chapter 4 results and discussion are presented and Chapter 5 gives conclusions and recommendations for future work.

Chapter 2

Background

The response of surfaces to mechanical loading has been studied for some time. The response to loading involves an elastic portion and a plastic portion which are typically convolved with each other. The elastic response can be quantified by the elastic modulus or elastic moduli in various directions. The plastic response includes active slip systems, interaction of dislocations, twinning and hardness. Some examples of mechanical loading of the surface are: processing conditions such as polishing or turning on a lathe, the stress imposed on a substrate by film growth, and equipment specifically designed to measure the response to mechanical loading. For example during nanoindentation the load on the indenter and the depth of penetration are continuously measured to determine the surface response to loading. The study of the surface response to loading is of significant interest, further for many semiconductors dislocations in the near surface can adversely effect the epitaxial growth of films, the electrical properties and the photoluminescence response of the surface.

The response of single crystal ZnO to mechanical loading has not received much attention. In this chapter background information on previous studies of the mechanical behavior of ZnO and techniques to evaluate near surface mechanical behavior is presented. First some of the physical properties of ZnO including its structure, hardness and elastic stiffness constants are given. The results of one study which has measured the near surface damage in single crystal ZnO introduced by various polishing processes are presented. Nanoindentation is increasingly being used to study the near surface mechanical behavior of materials. The analysis technique that determines the hardness and elastic modulus from nanoindentation data is presented for an isotropic material and for a transversely isotropic piezoelectric material such as ZnO. In addition to hardness and elastic modulus other behavior such as “pop-in” and indentation size effect have been observed in many materials during nanoindentation. Pop-in is often related to the onset of plasticity and the indentation size

effect may be related to the gradient of strain in the material. These are explained in more detail in this chapter. Illumination has been shown to effect mechanical behavior of many bulk II-VI semiconductors however the effects of illumination have not been investigated at smaller length scales in ZnO. A brief review of the effects of illumination on the response to mechanical loading is presented for bulk II-VI semiconductors. Near surface damage such as dislocations and point defects introduced by mechanical loading is known to alter the electrical characteristics of many semiconductors. One way to measure changes in the electrical characteristics at the nanometer scale is the use of scanning Kelvin probe microscopy (SKPM) which measures the potential difference between the probe and the sample with a lateral resolution approaching 50 nm. SKPM can be combined with nanoindentation to measure the damage introduced during nanoindentation. The technique of SKPM is presented along with some examples from the literature of uses of the technique.

2.1 Properties and subsurface damage of ZnO

ZnO most commonly exists in the hexagonal wurtzite structure although it can also form in the zincblende structure. The wurtzite structure has two distinct planes perpendicular to the $\langle 0001 \rangle$ direction, an oxygen terminated $(000\bar{1})$ plane and a zinc terminated (0001) plane. Figures 2.1, 2.2 and 2.3 show a ball and stick model of ZnO from various directions. In Figs. 2.1 and 2.2 the $\{0001\}$ planes are horizontal and in Fig. 2.3 the reader is looking down onto a $\{0001\}$ plane. The lattice spacing for ZnO is $c = 0.519$ nm and $a = 0.324$ nm [23].

The mechanical properties of single crystal ZnO are not well known because of the only recent availability of high-quality samples. Most of the previous work done on the assessment of the mechanical properties of ZnO was done on material that had a significant concentration of lithium

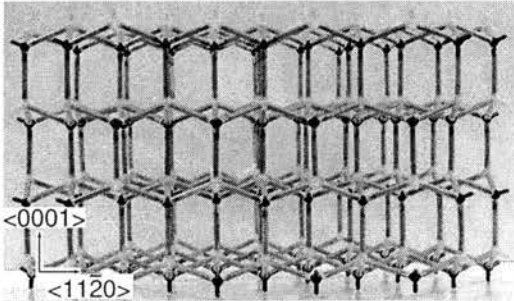


Figure 2.1: Photograph of ball and stick model of ZnO looking in the $\langle 10\bar{1}0 \rangle$ direction.

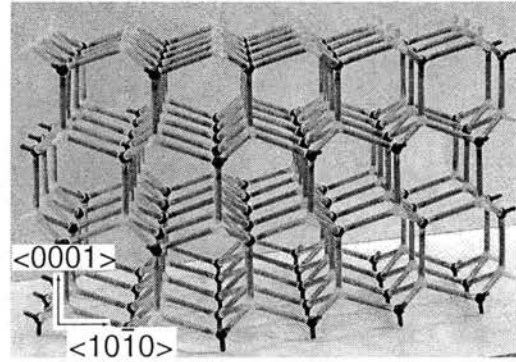


Figure 2.2: Photograph of ball and stick model of ZnO looking in the $\langle 1010 \rangle$ direction.

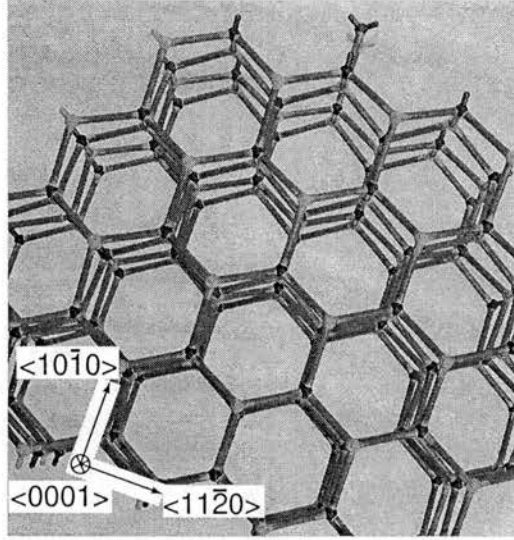


Figure 2.3: Photograph of ball and stick model of ZnO looking along the $\langle 0001 \rangle$ direction.

and/or sodium ions [24] and much of this work focused on bulk material not the near surface. There have been a few nanoindentation experiments performed with a spherical indenter [25,26] on single crystal ZnO.

Regel et al. [24] performed microhardness measurements on hydrothermally grown ZnO samples of different crystallographic orientations. In this study it is not stated which type of indenter was used for the experiment (presumably it was a Vickers indenter) nor is it stated at which load the hardness was evaluated. The samples were polished but it is not stated what type of polishing was performed. Table 2.1 shows the results for various crystallographic surfaces. The hardness of the basal (0001) plane was found to be about twice that for the prismatic planes, $\{10\bar{1}0\}$ and $\{11\bar{2}0\}$. A microhardness of 400 kg/mm^2 Vickers corresponds to about 4.3 GPa [27]. Ahearn et al. [28] studied the effects of bias voltage and pH on the hardness of (0001) and $\{10\bar{1}0\}$ ZnO. The experiments were performed with the sample in an electrolyte with the ability to apply a bias voltage to the sample. Without any bias voltage the Vickers hardness of the (0001) surface ranged from $240 - 260 \text{ kg/mm}^2$

Surface	Microhardness (kg/mm^2)
(0001)	400
$\{10\bar{1}1\}$	250
$\{10\bar{1}0\}$ and $\{11\bar{2}0\}$	200

Table 2.1: Comparison of microhardness for different surfaces of ZnO. After Regel et al. [24].

for pH between 8.5 – 12.2 and for the $\{10\bar{1}0\}$ surface the hardness ranged from 100 – 130 kg/mm² for pH between 6.5 – 11.5. Although the hardness values were about half of the values obtained by Regel et al. [24], the hardness of the basal plane was still about twice that of one of the prismatic planes. The differences in hardness are most likely caused by differences in the slip systems that are activated during indentation. Some of the slip planes that have been identified in ZnO include $\{0001\}$ [26], $\{10\bar{1}1\}$ [26], and $\{10\bar{1}2\}$ [29]. During indentation of the prismatic surfaces the force of the indenter is principally in the $\langle 0001 \rangle$ direction, so that slip will probably principally involve slip on the $\{0001\}$ planes. In many hexagonal metals slip at room temperature occurs most easily on the $\{0001\}$ planes [20].

The elastic constants of ZnO were measured by Bateman [30] using an ultrasonic pulse technique, Table 2.2. Using these elastic constants, the Voigt or Reuss aggregate average elastic modulus and Poisson’s ratio can be computed. The aggregate elastic modulus is 123 GPa (Reuss) to 124 GPa (Voigt) and Poisson’s ratio is 0.356 (Voigt) to 0.357 (Reuss) [31]. ZnO is a piezoelectric material with piezoelectric and dielectric constants given in Table 2.3. The piezoelectric and dielectric constants were determined by the ultrasonic resonance-antiresonance method [32]. The “S” superscript on the dielectric constants denotes that it is the dielectric constant value for a mechanically constrained sample.

Kucheyev et al. [25] used nanoindentation with a spherical indenter with a radius of 4.2 μm to examine the material properties of $(000\bar{1})\text{ZnO}$. It is not stated how the samples were polished. They measured a hardness between 4 – 5 GPa for a depth of 50 – 400 nm which is consistent with Regel et al. [24] and an elastic modulus of 100 – 111 GPa over the same depth range. The elastic modulus is less than one would expect from either the aggregate averages or the stiffness in the $\langle 0001 \rangle$ direction where $E_{\langle 0001 \rangle} = 139$ GPa. The authors give no explanation for this discrepancy however it may be caused by the method used to analyze the data. The data was analyzed using the partial load-unload method of Field and Swain [33]. This method fits only a single pair of data points and is therefore more susceptible to error [34] than the Oliver and Pharr [35] method (explained in Section 2.2.1).

2.1.1 Assessment of subsurface damage in polished ZnO by ion channeling

Surface preparation techniques can introduce dislocations and other defects in the near surface which may alter the mechanical behavior. For semiconductors, dislocations and defects can also alter the electrical properties [36–38] and the photonic properties [16]. Lucca et al. [19] used ion channeling to study the near surface damage in polished $(0001)\text{ZnO}$ and $(000\bar{1})\text{ZnO}$. The samples were prepared by

Elastic Stiffness	Value (GPa)
c_{11}	209.7
c_{12}	121.1
c_{13}	105.1
c_{33}	210.9
c_{44}	42.5
$c_{66} = \frac{1}{2}(c_{11} - c_{12})$	44.3

Table 2.2: Elastic stiffness constants of ZnO at room temperature obtained by ultrasonic pulse technique. After Bateman [30].

Piezoelectric and dielectric constant	Value
e_{31}	-0.62 C/m ²
e_{33}	0.96 C/m ²
e_{15}	-0.37 C/m ²
ϵ_{33}^S	7.8×10^{-11} F/m
ϵ_{11}^S	7.37×10^{-11} F/m

Table 2.3: Piezoelectric and dielectric constants of ZnO at room temperature obtained by resonance-antiresonance method. After Kobiakov [32].

either chemomechanical polishing, 1/4 μm diamond abrasive mechanical polishing or 1 μm diamond abrasive mechanical polishing. Table 2.4 shows the damage depth and the equivalent amorphous layer obtained for the samples. The damage depth is the extent of damage into the sample whereas the equivalent amorphous layer is related to the severity of damage. The equivalent amorphous layer is calculated from the number of displaced Zn (or O) atoms/cm² and the density of Zn (or O) atoms in ZnO. For the chemomechanical polished samples no damage was detected with this technique. The (0001) and (000 $\bar{1}$) surfaces were found to have similar damage depths except for the case of the 1 μm mechanical polish samples where the (0001) surface had slightly more severe damage.

	(0001)ZnO	(000 $\bar{1}$)ZnO
Process	Damage Depth (nm)	
1 μm mechanical polished	235	235
1/4 μm mechanical polished	115	115
chemomechanical polished	—	—
Process	Equivalent Amorphous Layer (nm)	
1 μm mechanical polished	45	38
1/4 μm mechanical polished	13	13
chemomechanical polished	—	—

Table 2.4: Damage depth and equivalent amorphous layer for polished ZnO obtained by ion channeling. After Lucca et al. [19].

2.2 Nanoindentation studies

Nanoindentation is an instrumented indentation technique that continuously records the depth of indentation and the force on the indenter. As in conventional hardness testing the indenter is made of a hard material such as diamond or sapphire. The shape of the indenter is typically spherical or pyramidal. Nanoindentation most often uses a three sided pyramidal indenter called a Berkovich indenter, Fig. 2.4, rather than a four sided pyramidal indenter used in conventional hardness testing. The Berkovich indenter was designed to yield the same cross-sectional area as a function of distance from the tip as a Vickers indenter, $A(h) = 24.5h^2$ where h is the distance from the tip. The nanoindentation system used in this study is shown in Fig. 2.5 and is typical of many nanoindentation systems. The system also includes a controller and data collection computer which are not shown in the figure. The particular system shown uses a three-plate parallel capacitor for both the application of force and the measurement of displacement. Other systems use a voice-coil for the force transducer and a capacitance sensor for displacement measurement [35].

Nanoindentation enables the probing of small volumes of materials to determine not only the elastic modulus and hardness of the near surface but more generally the response of the sample to loading. In many single crystal materials the onset of plasticity starts with a sudden increase in the indenter penetration at a given force called “pop-in”. Many materials exhibit an increase in hardness at decreasing indentation depths in nanoindentation testing called “indentation size effect” more fully explained below.

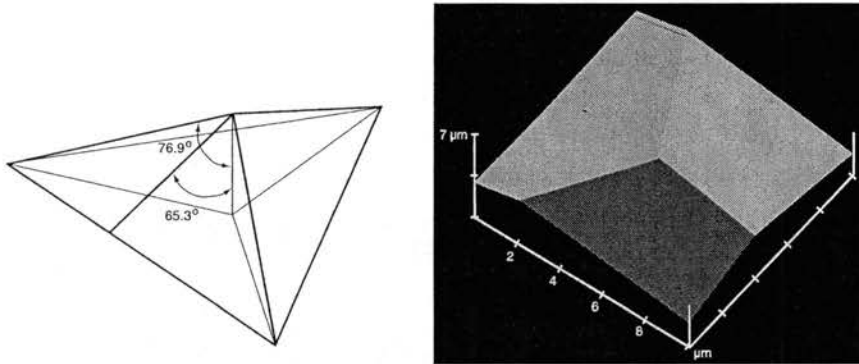


Figure 2.4: Schematic diagram of the Berkovich indenter (left) and an AFM image of a Berkovich indenter (right).

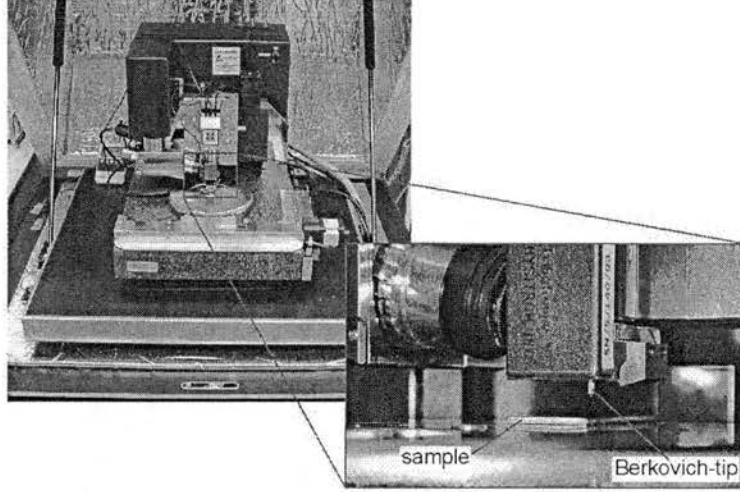


Figure 2.5: Photograph of nanoindentation system used in the study. Close-up shows the force transducer with an indenter mounted to it.

2.2.1 Elastic modulus and hardness

The most commonly used method of obtaining the elastic modulus and hardness from nanoindentation data is the method given by Oliver and Pharr [35]. Nanoindentation data is usually plotted as the applied load vs. indenter penetration as shown schematically in Fig. 2.6. During loading the material deforms elastically or elastically and plastically while during unloading the material behaves mainly elastically. To obtain the elastic modulus and hardness of the material solutions for the indentation of an elastic half-space are used to analyze the unloading curve. The slope of the unloading curve at the maximum depth, h_{\max} , is denoted by S and is related to the elastic modulus of the sample. The contact depth is the depth to which the indenter and the sample are in contact under load and is denoted by h_c . The relationship between the contact depth, the total depth, h ,

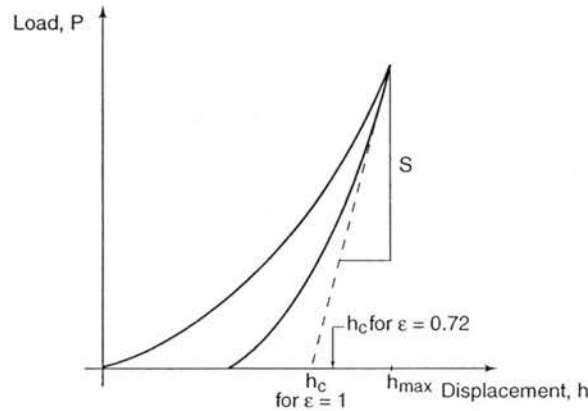


Figure 2.6: Idealized load vs. displacement plot showing the unloading slope at the maximum depth, S and the contact depth, h_c .

and the displacement of the surface at the perimeter of the indentation, h_s is shown in Fig. 2.7a. The final depth of the indentation, also called the plastic depth, is given by h_f , Fig. 2.7b. To calculate the contact depth h_c from experimental data, one needs to know h_s since h_{\max} is known and

$$h_{\max} = h_c + h_s. \quad (2.1)$$

To obtain the displacement of the surface at the perimeter of the indentation, h_s , the results of Sneddon [39] who analyzed the indentation of an elastic half-space with an axisymmetric indenter are used. Sneddon's results must be modified by replacing the elastic displacement by the total displacement minus the final or plastic depth, $(h - h_f)$. It can be shown that the displacement of the surface at the perimeter of the indentation can be given as [35]:

$$h_s = \epsilon \frac{P_{\max}}{S} \quad (2.2)$$

where ϵ for various indenter geometries is given in Table 2.8.

Oliver and Pharr [35] suggest that $\epsilon = 0.75$ is the best value to use for a Berkovich indenter. From the calculated h_s , and the measured h_{\max} , h_c can be calculated from Eq. 2.1. The stiffness of the sample S which is the slope of the unloading curve evaluated at the maximum depth is determined by fitting the unloading data to the power law relationship:

$$P = \alpha (h - h_f)^m \quad (2.3)$$

where α , h_f and m are fitting parameters. From the curve fit the slope at the maximum depth, S , can be calculated by differentiation, $\frac{dP}{dh} \big|_{h=h_{\max}} = \alpha m (h_{\max} - h_f)^{m-1}$. The reduced elastic modulus,

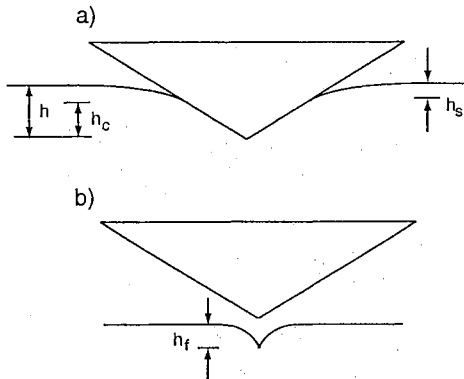


Figure 2.7: Schematic diagram of various depth definitions. (a) shows the indenter under load and (b) shows the surface after the indenter has been removed.

Geometry of Indenter	ϵ
Conical Indenter	$2 - \frac{4}{\pi} \approx 0.72$
Flat Punch	1
Paraboloid of Revolution	0.75

Figure 2.8: ϵ values for various indenter geometries.

E_r , is determined from the slope of the unloading curve, S and the contact area, A by the following:

$$E_r = \frac{\sqrt{\pi}}{2} \frac{S}{\sqrt{A}} \quad (2.4)$$

The reduced elastic modulus takes into consideration the fact that the indenter is not perfectly rigid and so the measured elastic modulus is a combination of the elastic modulus of the material and of the indenter. The elastic modulus of the material can be obtained by:

$$\frac{1}{E_r} = \frac{1 - \nu_s^2}{E_s} + \frac{1 - \nu_i^2}{E_i} \quad (2.5)$$

where ν_s is the Poisson's ratio for the sample, E_s is the elastic modulus of the sample and ν_i and E_i are the same values for the indenter. Typically diamond is used for the indenter material and it has $\nu_i = 0.07$ and $E_i = 1141$ GPa [31] so that the contribution of the indenter to measured elastic modulus is small. The contact area is determined from the contact depth, h_c , and the area function of the indenter. The area function of the indenter is determined from indentation into reference materials in a procedure outlined in Appendix A. The hardness of the sample is obtained from the maximum load and the contact area by the following:

$$H = \frac{P_{\max}}{A} \quad (2.6)$$

The evaluation of elastic modulus and hardness using nanoindentation has been applied to a variety of bulk materials and thin films as well. An example of a study on bulk materials is the work of Oliver and Pharr [35]. They report on the indentation of single crystal aluminum, tungsten, quartz and sapphire, soda-lime glass, and fused silica [35]. The materials were evaluated at maximum loads from 0.2 mN to 120 mN which corresponded to a depth of 20 nm to 5 μ m. The measured hardness values ranged from about 0.2 GPa for aluminum to 25 GPa for sapphire. The measured elastic modulus values ranged from about 70 GPa for aluminum, fused silica and soda-lime glass to 440 GPa for sapphire. The measured modulus values agreed to within 4% of the literature values [31] for all samples except quartz and sapphire which were 30% and 9% higher. Oliver and Pharr state that this discrepancy is because of the anisotropic nature of these materials.

The analysis of Oliver and Pharr presented above assumes the material is isotropic. As previously stated however ZnO is an anisotropic material that is also piezoelectric. Both the anisotropy and piezoelectric effect will influence the measured modulus. For indentation in anisotropic materials the analysis of the load-depth data is the same as for the isotropic case, however the interpretation of the reduced elastic modulus is different. The reduced elastic modulus, E_r , in Eq. 2.4 is replaced by the reduced indentation modulus M_r . The indentation modulus of the sample, M_s , is determined

from the reduced indentation modulus and the indentation modulus of the indenter, M_i , [40]:

$$M_r = \left(\frac{1}{M_s} + \frac{1}{M_i} \right)^{-1} \quad (2.7)$$

The indentation modulus of the sample is a function of the crystallographic plane that is indented, the elastic stiffness values, the piezoelectric constants and dielectric constants. Strictly speaking one should also take into consideration the anisotropy of the diamond indenter however there is little error in using the aggregate properties. Diamond is a cubic material with elastic constants, $c_{11} = 1076$, $c_{12} = 125$, $c_{44} = 575.8$ GPa [31]. The anisotropy factor $(2c_{44}/(c_{11} - c_{12}))$ gives a measure of the degree of anisotropy of a cubic single crystal where an isotropic crystal has an anisotropy factor of 1.0. The anisotropy factor for common metals include copper, 3.2, nickel, 2.5, and iron, 2.4. The anisotropy factor of diamond is 1.2 so little error is introduced by using the aggregate values of the elastic modulus and Poisson's ratio to compute the indentation modulus of the indenter, $M_i = E_i/(1 - \nu_i^2)$.

To quantify the effects of anisotropy and piezoelectricity on the indentation modulus of ZnO two models of indentation are considered. The first model neglects the piezoelectric effect and only considers indentation on the $\{0001\}$ planes because these are the planes of isotropy i.e., the elastic stiffness in any direction in the $\{0001\}$ planes is constant. The analysis of indentation on the $\{0001\}$ planes is easier because of this symmetry. The second model includes the piezoelectric effect but is also restricted to indentation on the $\{0001\}$ planes. Although solutions exist for indentation of a general anisotropic half-space [40–43], they were not considered for this work because for the three surfaces of ZnO indented, $\{0001\}$, $\{10\bar{1}0\}$ and $\{11\bar{2}0\}$ the differences among the elastic moduli in the directions normal to the planes are small, Table 2.5.

Indentation of a transversely isotropic elastic half-space

Analysis of indentation of a transversely isotropic half-space has been treated by many researchers using different mathematical methods [44–47]. This section presents the setup of the problem for an arbitrary axisymmetric indenter and results for indentation with a conical indenter. To obtain

Elastic Modulus	Value (GPa)
$E_{\langle 0001 \rangle}$	139
$E_{\langle 10\bar{1}0 \rangle}$	126
$E_{\langle 11\bar{2}0 \rangle}$	126

Table 2.5: Elastic moduli in the three directions of indentation used in this study.

the indentation modulus, a relationship between the load, P , and the depth of penetration, h , is required.

An axisymmetric rigid indenter is aligned such that the plane of indentation is the symmetric plane of a transversely isotropic material which is the $\{0001\}$ plane for ZnO. Figure 2.9 shows the geometry of the problem where cylindrical coordinates (r, θ, z) are used because of symmetry and the indenter profile is given by $f(r)$. From a force balance on a volume of material, the equilibrium conditions for the stresses (σ_{ij}) can be given by [48]:

$$\begin{aligned}\frac{\partial \sigma_{rr}}{\partial r} + \frac{\partial \sigma_{rz}}{\partial z} + \frac{\sigma_{rr} - \sigma_{\theta\theta}}{r} &= 0 \\ \frac{\partial \sigma_{rz}}{\partial r} + \frac{\partial \sigma_{zz}}{\partial z} + \frac{\sigma_{rz}}{r} &= 0\end{aligned}\tag{2.8}$$

The relationship between the stress and material displacement ($u_r, u_\theta = 0, u_z$) for a transversely isotropic medium can be given by [49]:

$$\begin{aligned}\sigma_{rr} &= c_{11} \frac{\partial u_r}{\partial r} + c_{12} \frac{u_r}{r} + c_{13} \frac{\partial u_z}{\partial z} \\ \sigma_{\theta\theta} &= c_{12} \frac{\partial u_r}{\partial r} + c_{11} \frac{u_r}{r} + c_{13} \frac{\partial u_z}{\partial z} \\ \sigma_{zz} &= c_{13} \left(\frac{\partial u_r}{\partial r} + \frac{u_r}{r} \right) + c_{33} \frac{\partial u_z}{\partial z} \\ \sigma_{rz} &= c_{44} \left(\frac{\partial u_r}{\partial z} + \frac{\partial u_z}{\partial r} \right)\end{aligned}\tag{2.9}$$

where c_{ij} are the elements of the elastic stiffness matrix. Equations 2.9 are substituted into Eq. 2.8 to obtain a set of two partial differential equations that can be solved using Hankel transforms [45]

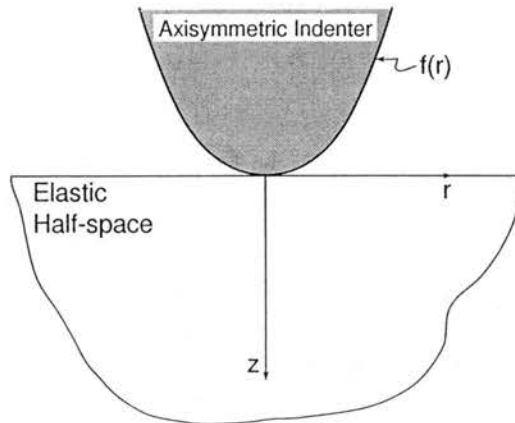


Figure 2.9: Schematic diagram of indentation of an elastic half-space by an axisymmetric indenter.

or other methods [44, 46, 47]. The boundary conditions for this problem are:

$$u_z(r, z=0) = f(r) + b \quad 0 \leq r \leq a \quad (2.10)$$

$$\sigma_{zz}(r, z=0) = 0 \quad r > a \quad (2.11)$$

$$\sigma_{zr}(r, z=0) = 0 \quad r \geq a \quad (2.12)$$

$$u_r, u_z \rightarrow 0 \quad \text{as } \sqrt{z^2 + r^2} \rightarrow \infty \quad (2.13)$$

Equation 2.10 gives the geometry of the deformed surface during indentation, $f(r)$ is the profile of the indenter and b is the penetration depth of the indenter at $r = a$. The indenter and half-space are in contact from $r = 0$ to $r = a$. The surface of the half-space outside the contact radius a does not have either normal stress, Eq. 2.11, or shear stress, Eq. 2.12. Eq. 2.13 states that the material displacements far from the indenter approach zero.

For a conical indenter the function $f(r)$ in Eq. 2.10 is given by $f(r) = \epsilon(1 - r/a)$. Fig. 2.10 shows a conical indenter with semi-angle α and total depth of penetration $b + \epsilon$. Hanson [46] solved this indentation problem using potential functions and gives results for all of the stresses and displacements. To obtain the indentation modulus, only the normal stress on the surface for $r \leq a$ is of interest. From Hanson [46] and Elliott [45] the normal stress on the surface can be given by:

$$\sigma_{zz}(r, z=0) = \frac{\epsilon}{\pi H a} \cosh^{-1} \left(\frac{a}{r} \right) \quad 0 \leq r \leq a \quad (2.14)$$

where H depends on material properties and is given by the following,

$$H = \frac{(\gamma_1 + \gamma_2) c_{11}}{2\pi (c_{11}c_{33} - c_{33}^2)}$$

The terms c_{ij} are the elastic constants and the terms $\gamma_{1,2}$ are obtained from the roots of the following equation:

$$c_{11}c_{44}n^2 + (c_{13}(c_{13} + 2c_{44}) - c_{11}c_{33})n + c_{33}c_{44} = 0$$

The terms $\gamma_{1,2}$ are computed from $\gamma_{1,2}^2 = n_{1,2}$. The total force on the indenter can be obtained by

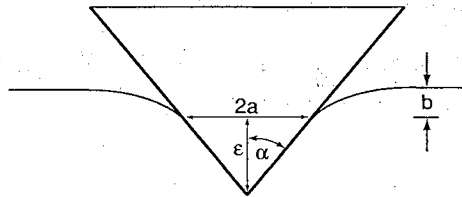


Figure 2.10: Schematic diagram of conical indenter under load.

integrating the normal stress over the contact area. This gives,

$$P = -2\pi \int_0^a \frac{\epsilon}{\pi H a} \cosh^{-1} \left(\frac{a}{r} \right) dr \quad (2.15)$$

$$P = -\frac{a\epsilon}{H} \quad (2.16)$$

In terms of the depth of penetration Eq. 2.16 can be given by:

$$P = \frac{2 \tan(\alpha)}{\pi^2 H} h^2 \quad (2.17)$$

To determine the indentation modulus of the sample (M_s) from Eqn. 2.17 the results of Pharr et al. [50] can be applied. They showed that results obtained for previous well-known indentation problems can be applied to any general relationship between the load and depth of penetration to obtain the indentation modulus of the sample. For example, consider the indentation of an isotropic medium by a flat ended rigid cylindrical punch. The indentation modulus in this case is known to be: $M_s = E_s/(1 - \nu_s^2)$ [50]. The indentation modulus is obtained from an expression for the load as a function of indenter penetration. The equation for the load and the depth of penetration can be given as [39]:

$$P = \frac{4\mu_s a}{(1 - \nu_s)} h \quad (2.18)$$

where μ_s is the shear modulus of the sample, a is the radius of the cylindrical indenter, and h is the depth of penetration. If this equation is differentiated with respect to h and the expression for the contact area ($A = \pi a^2$) is used the resulting equation is

$$\frac{dP}{dh} = \frac{4\mu_s \sqrt{A}}{(1 - \nu_s) \sqrt{\pi}} \quad (2.19)$$

For an isotropic material the shear modulus is related to the elastic modulus by $E = 2\mu(1 + \nu)$ so Eq. 2.19 becomes

$$\frac{dP}{dh} = \frac{2\sqrt{A}}{\sqrt{\pi}} \frac{E_s}{(1 - \nu_s^2)} \quad (2.20)$$

By comparing this equation to Eq. 2.4, the indentation modulus can be identified as $E_s/(1 - \nu_s^2)$. Note that because the indenter is assumed to be rigid the reduced indentation modulus depends only on the indentation modulus of the sample. For a general relationship between the load and depth of penetration, the same steps are followed. First differentiate the expression with respect to the depth then put the equation in the form of Eq. 2.20. Identify the part of the equation that is the indentation modulus of the sample.

Returning to the indentation of a transversely isotropic half-space, the differentiation of Eq. 2.17 with respect to h gives:

$$\frac{dP}{dh} = \frac{4 \tan(\alpha)}{\pi^2 H} h \quad (2.21)$$

Using relationships between a , h , and α , Eq. 2.21 can be written as

$$\frac{dP}{dh} = \frac{2}{\pi H} a \quad (2.22)$$

$$= \frac{2\sqrt{A}}{\sqrt{\pi}} \frac{1}{\pi H} \quad (2.23)$$

From Eq. 2.23 the indentation modulus can be identified as $1/\pi H$.

Indentation of a piezoelectric transversely isotropic elastic half-space

Because ZnO is a piezoelectric material, the indentation modulus will also contain a contribution from the piezoelectric effect. The model presented in this section, will predict how much the piezoelectric effect will influence the indentation modulus. Matysiak [51] presented a model for the indentation of piezoelectric materials with hexagonal symmetry which was based on the work of Kudriavtsev et al. [49]. The model of Matysiak was further developed by Giannakopoulos and Suresh [52] to include transversely isotropic materials and will be summarized below.

The problem setup is similar to the transversely isotropic case presented in the previous section however new terms and equations are needed to describe the piezoelectric effect. An axisymmetric rigid indenter is aligned such that the plane of indentation is the symmetric plane of a transversely isotropic material. Cylindrical coordinate (r, θ, z) , are used again. The equilibrium conditions for the stresses (σ_{ij}) are as before and are given by:

$$\begin{aligned} \frac{\partial \sigma_{rr}}{\partial r} + \frac{\partial \sigma_{rz}}{\partial z} + \frac{\sigma_{rr} - \sigma_{\theta\theta}}{r} &= 0 \\ \frac{\partial \sigma_{rz}}{\partial r} + \frac{\partial \sigma_{zz}}{\partial z} + \frac{\sigma_{rz}}{r} &= 0 \end{aligned} \quad (2.24)$$

and Maxwell's equation for this geometry is given by:

$$\frac{\partial D_r}{\partial r} + \frac{1}{r} D_r + \frac{\partial D_z}{\partial z} = 0 \quad (2.25)$$

where D_r and D_z are the electrical displacements in the r and z directions, respectively. For a linear dielectric material the electrical displacement \mathbf{D} can be given by $D_i = \epsilon_{ij} E_j$ where ϵ_{ij} are the dielectric constants and E_j are the components of the electric field. The components of the electric field, \mathbf{E} , are related to the electrical potential ϕ , by:

$$E_r = -\frac{\partial \phi}{\partial r} \quad E_z = -\frac{\partial \phi}{\partial z} \quad (2.26)$$

The constitutive equations for an elastic piezoelectric medium can be given by:

$$\begin{aligned}
\sigma_{rr} &= c_{11} \frac{\partial u_r}{\partial r} + c_{12} \frac{u_r}{r} + c_{13} \frac{\partial u_z}{\partial z} + e_{31} \frac{\partial \phi}{\partial z} \\
\sigma_{\theta\theta} &= c_{12} \frac{\partial u_r}{\partial r} + c_{11} \frac{u_r}{r} + c_{13} \frac{\partial u_z}{\partial z} + e_{31} \frac{\partial \phi}{\partial z} \\
\sigma_{zz} &= c_{13} \left(\frac{\partial u_r}{\partial r} + \frac{u_r}{r} \right) + c_{33} \frac{\partial u_z}{\partial z} + e_{33} \frac{\partial \phi}{\partial z} \\
\sigma_{rz} &= c_{44} \left(\frac{\partial u_r}{\partial z} + \frac{\partial u_z}{\partial r} \right) + e_{15} \frac{\partial \phi}{\partial r} \\
D_r &= e_{15} \left(\frac{\partial u_r}{\partial z} + \frac{\partial u_z}{\partial r} \right) - \epsilon_{11} \frac{\partial \phi}{\partial r} \\
D_z &= e_{31} \left(\frac{\partial u_r}{\partial r} + \frac{u_r}{r} \right) + e_{33} \frac{\partial u_z}{\partial z} - \epsilon_{33} \frac{\partial \phi}{\partial z}
\end{aligned} \tag{2.27}$$

where c_{ij} are the elements of the elastic stiffness matrix, e_{ij} are the piezoelectric constants, ϵ_{ij} are the dielectric constants, and the displacement of a material particle is given by u_r and u_z in the r and z directions. Notice in addition to two new equations for the electrical displacements, there are additional terms in the stress equations for the piezoelectric effect. Equations 2.27 are substituted into Eqs. 2.24 and 2.25 to obtain a set of three partial differential equations that can be solved using Hankel transforms. The boundary conditions for this problem can be divided into mechanical boundary conditions and electrical boundary conditions. The mechanical boundary conditions are the same as in the previous section:

$$u_z(r, z=0) = f(r) + b \quad 0 \leq r \leq a \tag{2.28}$$

$$\sigma_{zz}(r, z=0) = 0 \quad r > a \tag{2.29}$$

$$\sigma_{zr}(r, z=0) = 0 \quad r \geq a \tag{2.30}$$

$$u_r, u_z \rightarrow 0 \quad \text{as } \sqrt{z^2 + r^2} \rightarrow \infty \tag{2.31}$$

For the electrical boundary conditions two cases are considered: a conducting indenter and an insulating indenter [52]. For a conducting indenter the boundary conditions are:

$$\phi(r, z=0) = \phi_0 \quad 0 \leq r \leq a \tag{2.32}$$

$$D_z(r, z=0) = 0 \quad r \geq a \tag{2.33}$$

$$\phi \rightarrow 0 \quad \text{as } \sqrt{z^2 + r^2} \rightarrow \infty \tag{2.34}$$

Equation 2.32 states that the electrical potential on the surface of the sample in contact with the indenter is equal to the electrical potential of the indenter, ϕ_0 . The electric displacement in the z direction is zero outside the contact area as shown in Eq. 2.33 and the regularity condition i.e., the

potential goes to zero far from the indenter, is given in Eq. 2.34. For an insulating indenter the regularity condition is the same however the surface has no electric displacement in the z direction,

$$D_z(r, z=0) = 0 \quad r \geq 0 \quad (2.35)$$

$$\phi \rightarrow 0 \quad \text{as } \sqrt{z^2 + r^2} \rightarrow \infty \quad (2.36)$$

The constitutive equations (Eqs. 2.27) along with the mechanical and electrical boundary conditions comprise the system of equations to be solved. Appendix B presents in detail the method of solving these equations, the solution for a conical insulating indenter will be given here. The geometry of the indenter is the same as before, Fig. 2.10. For an indenter that is an insulator the load on the indenter can be given by:

$$P_{\text{insulating}} = \frac{4h^2 \tan(\alpha)}{\pi} \frac{M_8 M_5 - M_6 M_7}{M_2 M_7 - M_1 M_8} \quad (2.37)$$

where the values M_i are derived from the material properties and are given in Appendix B. Equation 2.37 has similar form as the case of indentation in a transversely isotropic material Eq. 2.17. To obtain the indentation modulus Eq. 2.37 is differentiated with respect to h

$$\begin{aligned} \frac{dP_{\text{insulating}}}{dh} &= \frac{8h \tan(\alpha)}{\pi} \frac{M_8 M_5 - M_6 M_7}{M_2 M_7 - M_1 M_8} \\ &= \frac{2\sqrt{A}}{\sqrt{\pi}} \frac{2(M_8 M_5 - M_6 M_7)}{M_2 M_7 - M_1 M_8} \end{aligned} \quad (2.38)$$

From Eq. 2.38 the indentation modulus can be identified as $\frac{2(M_8 M_5 - M_6 M_7)}{M_2 M_7 - M_1 M_8}$.

Table 2.6 shows a comparison of the indentation modulus for different indentation models. If the elastic half-space is assumed to be isotropic the indentation modulus is given by $E/(1 - \nu^2)$ where the elastic modulus and Poisson's ratio are the Reuss or Voigt aggregate values [31]. For the anisotropic case without piezoelectric effect included the indentation modulus is given by $1/\pi H$. For the anisotropic case with piezoelectric effect the indentation modulus is $\frac{2(M_8 M_5 - M_6 M_7)}{M_2 M_7 - M_1 M_8}$. The range of values given in the table for this case corresponds to the elastic and piezoelectric constants given in Tables 2.2 and 2.3 and those given by Dieulesaint and Royer [23]. The modulus obtained for the case of piezoelectric anisotropy is 7 – 10% larger than the isotropic case.

2.2.2 Onset of plasticity — pop-in

One behavior that is often observed in the nanoindentation of single crystal materials is “pop-in” [53]. Pop-in is the sudden increase in depth at a given load as shown in Fig. 2.11. Leipner et al. [53] attribute the observed pop-in in GaAs to the nucleation of dislocations. They performed

Assumed Half-space Properties	Indentation Modulus M_s (GPa)
Isotropic	141
Anisotropic not piezoelectric	147
Anisotropic piezoelectric	151 – 155

Table 2.6: Indentation modulus, M_s , for indentation of $\{0001\}$ surface of ZnO with a conical or spherical indenter. The range of values given for the case of an anisotropic piezoelectric half-space is based on different values for the elastic and piezoelectric properties.

transmission electron microscopy (TEM) on samples which had been indented with loads just above that required for pop-in and observed dislocation loops in a “rosette” around the indentation. The rosette was a cloverleaf pattern with four sets of loops emanating from the indentation along the $\langle 110 \rangle$ directions. In another study of pop-in, Miyahara et al. [54] observed pop-in in electropolished (001)W however pop-in was not observed when they indented mechanically polished (001)W. They stated the difference in pop-in behavior was because of the difference in the dislocation density between the electropolished and mechanically polished samples. The dislocation density of the electropolished sample was about $4 \times 10^{-3} \mu\text{m}^{-2}$ obtained by measurements of etch pits. The dislocation density of the mechanically polished sample could not be measured because the dislocation density was so high that the etch pits overlapped each other. Because of the significantly higher dislocation density of the mechanically polished sample there may be dislocations in the volume beneath the indenter so these dislocations can be moved or act as sources for dislocations starting at very low loads. The low density of dislocations for the electropolished sample suggests that under the indenter there may be no dislocations before pop-in. Kucheyev et al. [25] observed multiple pop-in events during nanoindentation of (0001)ZnO with a spherical indenter. For a single indentation with a maximum load of 100 mN up to five pop-in events were observed. To explain the multiple pop-ins they proposed that the initial pop-in corresponds to the nucleation of dislocations which then move in the directions of easy slip. At some point these dislocations become pinned and new dislocations must be created which corresponds to the next pop-in event.

2.2.3 Indentation size effect

In nanoindentation studies hardness is often found to increase as the depth of penetration decreases which is referred to in the literature as “indentation size effect (ISE)”. Some materials exhibit

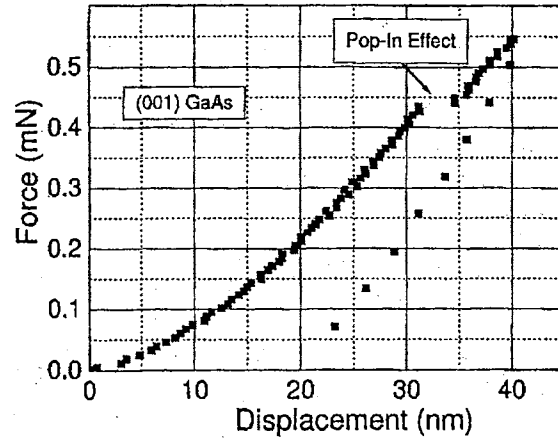


Figure 2.11: Sudden increase in depth at a given load, “pop-in”, observed in the indentation of (001)GaAs. From Leipner et al. [53].

what is called “reverse indentation size effect” [55] where the material is found to soften with decreasing depth of penetration but this is much less common. Figure 2.12 shows hardness results for the indentation of a silver/gold/silver layered structure [56]. The layered structure consisted of a (001)NaCl substrate with a 50 μm Ag layer, 50 nm Au and 1.2 μm Ag on top. The hardness increases from 400 MPa at the deepest depths to about 700 MPa at a plastic depth of about 100 nm. ISE is most often explained by strain gradient plasticity [57,58] which assumes that strain gradients are accommodated by “geometrically necessary” dislocations and uniform strain is accommodated by “statistically stored” dislocations [59]. Ma and Clarke [56] presented a simplified version of strain

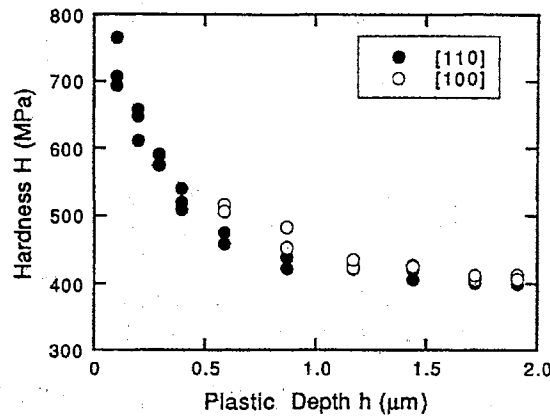


Figure 2.12: Example of indentation size effect in the indentation of (001)Ag/Au layered structure. The Berkovich indenter was aligned such that one of the edges of the triangular impression was in the [110] direction or [100] direction. From Ma and Clarke [56].

gradient plasticity as it applies to the nanoindentation of metals. The flow stress (τ) of the material is related to the dislocation density by the following [56]:

$$\tau = CGb\sqrt{\rho_S + \rho_G} \quad (2.39)$$

where G is the shear modulus of the material, b is the magnitude of the Burger's vector, C is a constant which is typically taken to be $\frac{1}{3}$, ρ_S is the density of statistically stored dislocations and ρ_G is the density of geometrically necessary dislocations. An estimate for the density of geometrically necessary dislocations is given by [56]:

$$\rho_G \approx \frac{4\gamma}{bD} \quad (2.40)$$

where γ is an average strain and D is the diameter of the indentation impression. The hardness is taken to be about 3 times the flow stress. Equation 2.40 can then be substituted into Eq. 2.39 to yield:

$$H \approx Gb\sqrt{\rho_S + \frac{4\gamma}{bD}} \quad (2.41)$$

Thus the hardness is inversely proportional to the square root of the diameter of the indentation. Using approximated values for the density of statistically stored dislocations and the average strain, Ma and Clarke [56] were able to obtain agreement with their indentation results. This model gives a plausible explanation for the indentation size effect but is difficult to apply directly to indentation data because the density of statistically stored dislocations and the average strain must be known.

2.3 Photoplastic effect

The increase (or decrease) of hardness or flow stress with illumination, referred to as the positive (or negative) photoplastic effect (PPE), has been reported for a variety of semiconductors. In a review article, Osip'yan et al. [21] summarize results for the photoplastic effect in bulk II-VI semiconductors. Typically the change in flow stress with illumination is measured during uniaxial compression tests on samples with dimensions of a few millimeters. Figure 2.13 shows the orientation of the samples for zincblende samples (left) and wurtzite samples (left and right). The zincblende samples are oriented for slip on the (111) planes while the wurtzite samples can be oriented for slip on either the basal planes $\{0001\}$ or the prismatic planes $\{10\bar{1}0\}$. The photoplastic effect has been observed for both zincblende II-VI compounds (ZnSe, ZnTe, CdTe) and wurtzite II-VI compounds (CdS, CdSe, ZnO) [21]. The observed increase of the flow stress with illumination is 10% – 30% for most of the II-VI semiconductors. For most of the II-VI semiconductors the maximum change in the flow stress occurs using light with energy slightly less than the band gap of the material. The photoplastic effect

has also been found time dependent. Carlsson and Svensson [60] observed that the photoplastic effect in ZnO persisted for about 15 sec. after the light source was turned off.

Osip'yan et al. [21] state that the reason for the positive PPE is the accumulation of electrons on dislocations as they move through the crystal. The charged dislocations interact electrostatically either with other charged dislocations or other charged defects within the crystals. This increases the amount of force required to move a dislocation thus increasing the hardness of the sample. They estimate that a dislocation in II-VI compounds must travel about $10\text{ }\mu\text{m}$ for it to acquire equilibrium charge. Wolf et al. [22,61] observed a positive PPE in ZnSe using nanoindentation. The illumination source was a tungsten halogen lamp with a flux of about 50 mW/cm^2 on the sample [22]. They indented (111)ZnSe over the depth range from 40 nm to 450 nm and found a 10% increase in hardness over this entire depth range. For the shallow indentations it seems unlikely that the dislocations would travel $10\text{ }\mu\text{m}$ and acquire equilibrium charge. Wolf et al. [22] proposed that the dislocations are charged by surface states of the ZnSe at shallow depths and at deeper depths the dislocations acquire charge by moving thorough the crystal. Wolf et al. [22] also observed an increase in the load at which elasto-plastic deformation begins with illumination. Although ZnSe was not found to exhibit pop-in, they were able to elastically load the sample up to a threshold value beyond which elasto-plastic deformation began. They found that in darkness the critical load for elasto-plastic deformation was $34 \pm 3\text{ }\mu\text{N}$ and with illumination the critical load was $44 \pm 3\text{ }\mu\text{N}$ [22]. No reason for this difference was given.

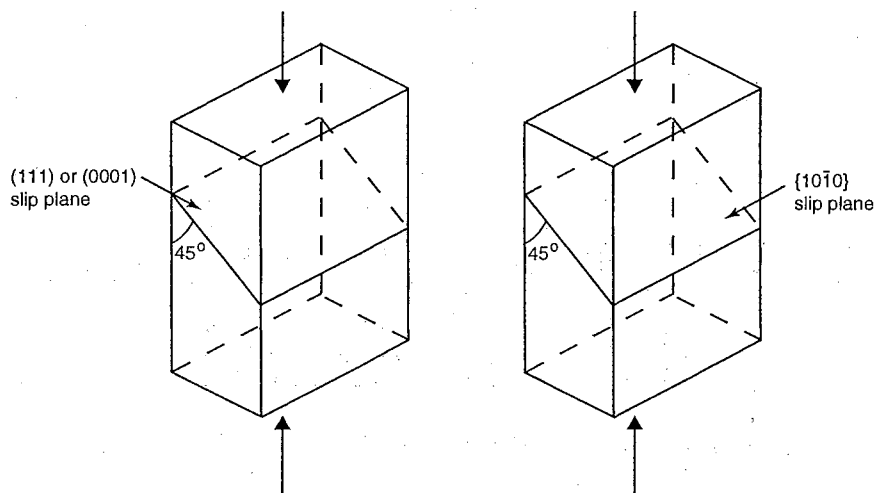


Figure 2.13: Orientation of samples for bulk compression tests. zincblende samples are oriented for (111) slip (left) and wurtzite samples are oriented for either (0001) slip (left) or $\{10\bar{1}0\}$ slip (right). After Osip'yan et al. [21].

2.4 Electrical property changes with the presence of dislocations

The relationship between the presence of defects in a material and changes in the electrical properties of the surface has been studied for some time. Changes in the local atomic bonding resultant from defects have a direct influence on the surface electrical properties. For example, dangling bonds associated with dislocations can act as acceptor-like sites [36,62] which can influence electrical properties by trapping carriers so that the free carrier concentration is reduced. Also, a space charge region is developed around trapped carriers, e.g., electrons, which changes the local carrier concentration and band structure. Alberts et al. [36] measured the carrier concentration of various p -type $\text{Al}_x\text{Ga}_{1-x}\text{As}$ layers on a (001)Si substrate prepared using organometallic vapor phase epitaxy. For a 4 μm thick film the presence of dislocations and microtwins near the $\text{Al}_x\text{Ga}_{1-x}\text{As}/\text{Si}$ interface was confirmed using cross-sectional TEM. In this region the hole concentration, obtained by electrochemical capacitance-voltage (C-V) measurement, was found to increase two orders of magnitude. Similar results have been obtained with ZnSe films on GaAs [63,64]. The trapping of electrons in n -type ZnSe lead to a decrease in the carrier concentration of about one order of magnitude near the ZnSe/GaAs interface. Girault et al. [37] introduced dislocations in $n\text{-Hg}_{0.8}\text{Cd}_{0.2}\text{Te}$ by uniaxial plastic deformation at room temperature, and found that at small deformations the carrier concentration decreased while at higher deformations the carrier concentration increased. A possible explanation given for the increase was the generation of donor-type point defects at higher deformations. Guergouri et al. [62] studied the effects of dislocations introduced by indentation on $p\text{-Cd}_{0.96}\text{Zn}_{0.04}\text{Te}$. From C-V curves measured before and after indentation, the carrier concentration was found to increase from $9.25 \times 10^{12} \text{ cm}^{-3}$ to $2.4 \times 10^{13} \text{ cm}^{-3}$.

Whereas traditional materials analysis techniques, including secondary ion mass spectrometry (SIMS), spreading resistance profiling (SRP), and capacitance-voltage (C-V) measurements have long been used for the characterizations of the electrical properties of surfaces mentioned above, they are limited by one-dimensional capability and spatial resolution. The maturation of atomic force microscopy (AFM) has brought on the development of a variety of techniques, based on the AFM, which enable the measurement a variety of properties including work function, electric field strength, resistance and capacitance. The scanning probe microscope now enables these measurements to be performed with two-dimensional spatial resolution down to 10 nm [65]. The capability for high lateral spatial resolution allows for mapping local properties changes within the plane of the finished

surface or can provide the possibility for cross-sectioned samples (e.g., cleaved crystals) to be scanned across their thickness enabling damage-depth information to be obtained.

Scanning surface potential microscopy, also known as scanning Kelvin probe (SKPM) microscopy [66] measures the contact potential difference (difference in work functions) between the probe and the sample. The technique is explained in more detail in Sec. 2.5 however a brief explanation follows. To measure the contact potential difference, an AC voltage with DC offset is applied to a metal-coated probe, and the sample, probe, and a well-controlled air gap between the probe and sample act as a capacitor. The associated electric field results in a force between the probe and sample, which at the frequency of the applied voltage, is proportional to the difference between the DC offset voltage and the contact potential difference between the sample and probe. A feedback loop is used to adjust the DC offset voltage to null the force at the frequency of the applied AC voltage. The offset voltage is equal to the contact potential difference between the sample and probe. A method for correcting for the possible distortions in measured potential which may occur because of topography has been reported [67].

In a study of a cleaved GaAs/AlAs multiple quantum well and a cleaved InAlAs/InGaAs heterostructure, surface potential on layers as thin as 40 nm was able to be measured [68]. Lateral resolution as small as 10 nm has been reported [65]. Agreement between measurements of the location of a Si p - n junction made by scanning capacitance microscopy and scanning Kelvin probe microscopy has been reported [69].

2.5 Scanning Kelvin probe microscopy

Scanning Kelvin probe microscopy (SKPM) is based on the Kelvin method [70] to determine the work function difference between a probe and sample. In SKPM a metal coated or heavily doped semiconductor probe is used in an atomic force microscope which operates in “tapping mode” (intermittent contact mode). Topography and surface potential data are collected on two consecutive passes of the probe over a given area, as shown in Fig. 2.14. After the topography of the surface is measured the probe is raised a user defined amount above the surface, usually 10 – 70 nm, to measure the surface potential. On this pass a voltage ($V_{dc} + V_{ac} \cos(\omega t)$) is applied to the probe which because of the capacitance between the sample and probe causes a force on the probe in the vertical or z -direction given by [71]:

$$F_z = -\frac{1}{2} \frac{\partial C}{\partial z} V^2 \quad (2.42)$$

where C is the capacitance between the sample and probe and V is the potential difference between the sample and probe. The van der Waals forces between the probe and sample have been neglected in Eq. 2.42 because they are about one order of magnitude less [73] than the capacitive forces for typical probe-sample separation distances used. The potential difference between the probe and the sample is given by [71]:

$$V = V_{dc} + V_{ac} \cos(\omega t) + \Delta V \quad (2.43)$$

where ΔV is the potential difference between the probe and sample without an external voltage applied. To determine ΔV , the probe and sample can be analyzed as a metal-insulator-semiconductor system [74]. From the energy band diagram for this case, shown in Fig. 2.15, ΔV is equal to $(\phi_{\text{probe}} - \chi - qV_n - \Delta\phi)$ where ϕ_{probe} is the work function of the probe, χ is the electron affinity of the sample, qV_n is the difference in the Fermi energy level and the conduction band in the bulk, and $\Delta\phi$ is the amount of band bending. Substituting Eq. 2.43 into Eq. 2.42 gives the total force on the

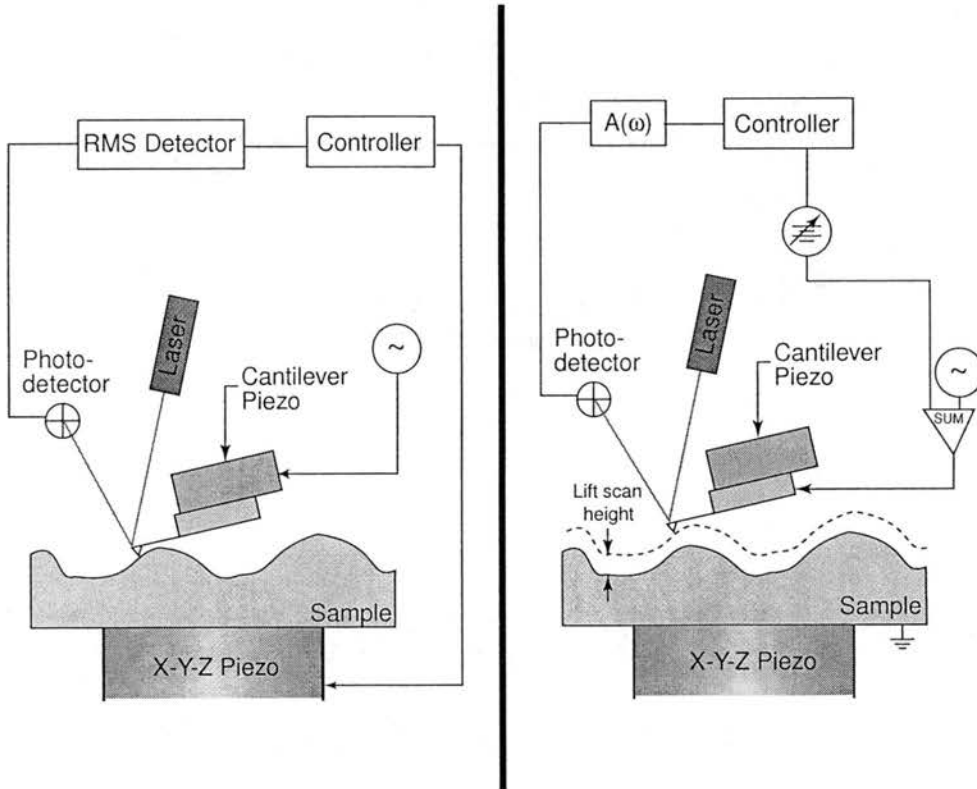


Figure 2.14: Schematic diagram of method of scanning Kelvin probe microscopy. The left part of figure shows the first pass of the probe to acquire the topography and the right part of figure shows the probe's second pass to acquire the surface potential. After Bhushan and Goldade [72].

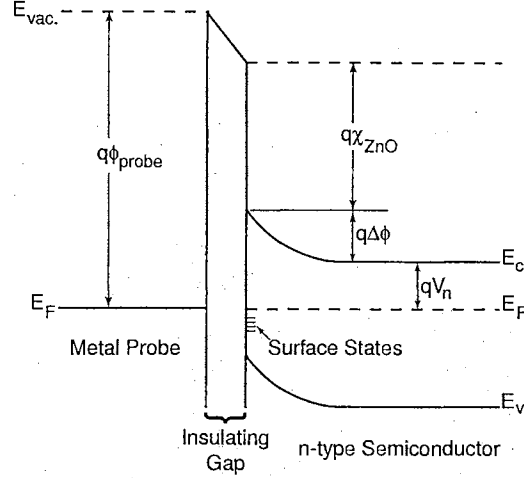


Figure 2.15: Energy band diagram for a metallic probe near n -type semiconductor separated by an insulating air gap. After Sze [74].

probe which has a constant component, a component at frequency ω and a component at 2ω .

$$F_z = -\frac{1}{2} \frac{\partial C}{\partial z} \left\{ (V_{dc} + \Delta V)^2 + \frac{1}{2} V_{ac}^2 + 2(V_{dc} + \Delta V) V_{ac} \cos(\omega t) + \frac{1}{2} V_{ac}^2 \cos(2\omega t) \right\} \quad (2.44)$$

The amplitude of the component at frequency ω is equal to:

$$F_{z,\omega} = -\frac{\partial C}{\partial z} V_{ac} (V_{dc} + \Delta V) \quad (2.45)$$

To obtain the contact potential difference between the probe and the sample, ΔV , a feedback loop on the dc component of the applied voltage to the probe (V_{dc}) is adjusted to null the force at frequency ω . When this occurs the applied V_{dc} is equal to:

$$-(\phi_{\text{probe}} - \chi - qV_n - \Delta\phi) \quad (2.46)$$

In scanning Kelvin probe microscopy, the null voltage is recorded at discrete points to obtain a surface map of the contact potential difference. Equation 2.46 shows that the surface potential measurement is relative to the work function of the probe. Scanning Kelvin probe microscopy is sensitive to anything that shifts either the Fermi level (qV_n) or the amount of band bending ($\Delta\phi$) e.g., chemical contamination or damage [75].

Koley and Spencer [76] used scanning Kelvin probe microscopy to investigate grown-in dislocations in an n -GaN film and a $\text{Al}_{0.35}\text{Ga}_{0.65}\text{N}/\text{GaN}$ heterostructure. Both the GaN film and the $\text{Al}_{0.35}\text{Ga}_{0.65}\text{N}/\text{GaN}$ heterostructure contained small pits on the surface which were identified as screw or mixed screw-edge dislocations based on previous studies. The pits were approximately 2 nm deep and had a full width at half maximum (FWHM) of 40 – 50 nm. The surface potential around these pits was found to be higher than the surrounding area. On the $\text{Al}_{0.35}\text{Ga}_{0.65}\text{N}/\text{GaN}$

heterostructure the magnitude of the increase was 0.1 – 0.2 V and on the GaN film the increase of the surface potential was 0.3 – 0.5 V. The width of the increase in the surface potential was 100 – 200 nm (FWHM) for the $\text{Al}_{0.35}\text{Ga}_{0.65}\text{N}/\text{GaN}$ heterostructure and 20 – 50 nm (FWHM) for the GaN film. Koley and Spencer explained the increase in surface potential around the dislocations using a model similar to Read's model [77]. In Read's model dislocations act as acceptor sites with energy slightly below the Fermi energy level. The dislocation becomes negatively charged as electrons populate the acceptor sites which causes the bands to bend near the dislocation by an amount $q\Delta\phi$, Fig. 2.16.

Krtschil et al. [78] investigated the changes in surface potential around dislocations in GaN films with different dopants. Three 1 – 2 μm thick films with the following dopants were studied: undoped, $n \approx 10^{16} \text{ cm}^{-3}$; Si doped, $n \approx 10^{17} - 10^{18} \text{ cm}^{-3}$; Mg doped, $p \approx 1 - 2 \times 10^{17} \text{ cm}^{-3}$. The surface of the sample contained pits which were identified as the termination of dislocations. For the Mg doped sample there was an increase in the surface potential around the dislocations however on the Si doped sample no changes in the surface potential around the dislocations was observed. On the undoped sample some of the pits showed an increase in surface potential while others had no change in surface potential. Krtschil et al. suggest that the dopant atoms may decorate the dislocations and compensate the charge on dislocations. For the case of the Mg doped samples the increase in surface potential is explained by Mg^- accumulating around the dislocation core and overcoming the positive core charge. For the Si doped samples Si^+ accumulate around the dislocation core and compensate the negative core charge exactly. Krtschil et al. suggest that the undoped sample has impurities that may accumulate on the dislocation giving either a negative or neutral charge depending on the impurity. Krtschil et al. do not explain why in the case of the Mg doped sample the dislocation core would be positively charged whereas in the case of the Si doped sample the dislocation core would be negatively charged.

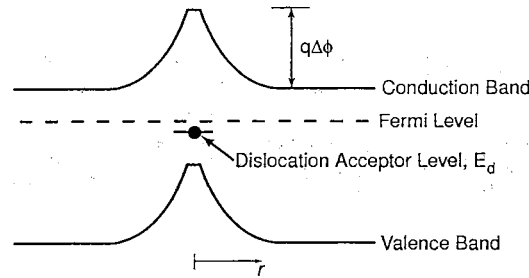


Figure 2.16: Schematic diagram of spatial dependence of potential around a dislocation. After Read [77].

Another possible explanation for the change in surface potential around dislocations in hexagonal piezoelectric crystals is the piezoelectric effect. In the theoretical paper by Shi et al. [79] two types of dislocations in GaN were considered: screw dislocations with Burgers vector $\mathbf{b}_s = \langle 0001 \rangle$ and edge dislocations with $\mathbf{b}_e = \frac{1}{3}\langle 11\bar{2}0 \rangle$. These two dislocations were chosen because the equations for the displacement of the atoms around the dislocation are well known and have a simple form [80]. For the screw dislocation the piezoelectric polarization in cylindrical coordinates (r, θ, z) was found to be:

$$\mathbf{P}_s = \frac{b_s e_{15}}{2\pi r} \hat{\theta}$$

where e_{15} is a piezoelectric constant and the z direction is in the $\langle 0001 \rangle$ direction. The surface charge is given by $\sigma_b = \mathbf{P} \cdot \hat{\mathbf{n}}$ and the volume charge by $\rho_b = -\nabla \cdot \mathbf{P}$ [81] where $\hat{\mathbf{n}}$ is the outward pointing surface normal unit vector. The unit normal is $\hat{\mathbf{z}}$ so there is no surface charge and the polarization is not divergent so the volume charge is also zero. For the case of the edge dislocation the polarization around the dislocation is given by:

$$\mathbf{P}_e = \frac{b_e e_{31}(1-2\nu)}{2\pi(\nu-1)} \frac{\sin \theta}{r} \hat{\mathbf{z}}$$

where $\nu = \frac{c_{12}}{(c_{12}+c_{11})}$. The divergence of this polarization is again zero however the surface charge when the dislocation intersects the surface is non-zero. The surface charge density is given by:

$$\sigma_b = \frac{b_e e_{31}(1-2\nu)}{2\pi(\nu-1)} \frac{\sin \theta}{r}$$

For GaN Shi et al. [79] calculated a surface charge density on the order of 10^{11} e/cm^2 at a radius of 100 nm from the dislocation core. Although this analysis does not analyze other possible dislocations in hexagonal piezoelectric crystals, it demonstrates that the piezoelectric effect may have an influence on the surface potential.

Bai et al. [82,83] studied the charge on stationary dislocations by measuring the surface potential around indentations and scratches in (110)ZnS. The samples were prepared by cleaving to expose a (110) surface. The indentation in the surface was a Vickers indentation with a size of approximately 20 μm on a side which corresponds to a depth of 4 μm . Bai et al. assumed that the charge density in the near surface is independent of depth and then calculated the charge density using the two dimensional Poisson's equation, $\frac{\partial^2 V(x,y)}{\partial x^2} + \frac{\partial^2 V(x,y)}{\partial y^2} = -\frac{\rho_e(x,y)}{\epsilon_r}$ where $V(x,y)$ is the measured surface potential, ρ_e is the charge density, ϵ is the permittivity, and x,y are the lateral coordinates. They estimated the dislocation density from the topographical data using $\rho_d(x,y) = \frac{\partial^2 z(x,y)}{\partial x \partial y} \frac{1}{b_z}$ where $\rho_d(x,y)$ is the dislocation density, z is the height of the sample, x,y are the lateral coordinates and b_z is the magnitude of the Burgers vector in the z direction. The charge on dislocations

was calculated at every data point by dividing the charge density by the dislocation density. The maximum charge density was found to be -1.5×10^{-10} C/m for S(g) dislocations and 1×10^{-10} C/m for Zn(g) dislocations. These values are the same order of magnitude as previous reported values on the charge of moving dislocations in ZnS, -3×10^{-10} C/m for S(g) dislocations [84]. This same group reported similar results for dislocations around scratches in (110)ZnS [82].

Weaver and Wickramasinghe [75] combined scanning Kelvin probe microscopy with illumination of the sample with above band gap energy to measure the surface photovoltage of silicon and gallium arsenide. Figure 2.17 shows the band diagram for a doped n -type semiconductor in darkness (a) and with illumination (b). In darkness the filled surface states cause the conduction and valence bands to bend upward. With above band gap illumination electron-hole pairs are generated and the photo-generated holes are attracted to the electrons in the surface states and recombine with them lessening the band bending. When the conduction and valence bands are flat the sample is said to be saturated or at the flat band potential. The change in the amount of band bending is measured by SKPM and is called the surface photovoltage. The surface photovoltage is sensitive to changes in the rate of generation of carriers, the rate of recombination, and the amount of band bending at the surface [75]. These changes can be caused by dislocations, doping, trapped charge or passivation [75]. Weaver and Wickramasinghe demonstrated the use of surface photovoltage to detect n - and p -type dopants in Si and a crack in p -type Si. A crack in the silicon sample intersected the surface at an angle such that part of the crack tip was not detected with the topography measurement but was detected with the surface photovoltage. They also measured differences in the surface photovoltage of a polished GaAs wafer. Based on the shape of the region with a change in the surface photovoltage, they interpreted it as caused by dislocation loops beneath the surface of the wafer.

Whereas Weaver and Wickramasinghe [75] used above band gap illumination and measured the surface photovoltage at the nanometer length scale, others have used below band gap illumination and measured the surface photovoltage at the micrometer or larger length scale [85]. Balestra et al. [86] presented a model for the analysis of the time dependence of the surface photovoltage when using below band gap illumination in order to determine some of the surface state parameters. These surface state parameters include the concentration of electrons in the surface states with and without illumination, the density of unoccupied surface states with illumination, and the capture cross-section for photons of the surface states. The model makes the following assumptions: 1) there are no minority carriers with or without illumination, 2) there is no appreciable change in the bulk free electron density with illumination, 3) the only free carrier generation process is the transition of electrons from surface states into the conduction band, 4) there is a Schottky-type depletion layer

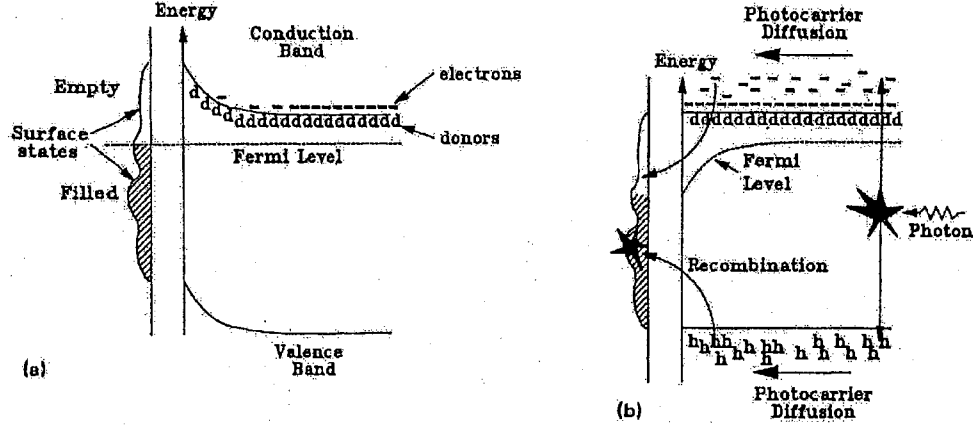


Figure 2.17: Effect of above band gap illumination on the band structure of the near surface of an n -type semiconductor. (a) shows the band structure in darkness with surface states causing upward band bending. (b) shows the diffusion of photo-generated carriers to the surface. From Weaver and Wickramasinghe [75].

at the surface, and 5) the surface photovoltage for $h\nu \approx E_c - E_t$ is primarily because of transitions from surface states with energy E_t . Figure 2.18 shows a schematic diagram of the time-dependent surface photovoltage response. The sample is initially in darkness and the flat band potential is given by V_s^0 , when the light is turned on at $t = t_0$, the surface potential increases to a steady-state value of V_s^1 . After steady-state is reached the light is turned off at $t = t_1$ and the surface voltage decreases. In order to obtain the density of occupied surface states, the light intensity I and the flat band potential V_s^0 must be known. The density of occupied surface states in darkness is given by:

$$n_t^0 = \frac{\alpha}{2} \frac{\delta v_s^1}{|v_s^0|^{1/2}} \frac{1}{1 + v_s^1/v_s^0}$$

where α is a constant given below and the lower case v 's are dimensionless surface voltages. The dimensionless surface voltages are given by $v_s = qV_s/kT$ where q is the charge of an electron, k is the Boltzmann constant and T is the absolute temperature. The superscript 0 refers to the sample in darkness, and the superscript 1 refers to the illuminated sample. The constant α is given by $\alpha = \sqrt{2\epsilon kT n_b}/q^2$ where ϵ is the dielectric permittivity of the semiconductor and n_b is the electron concentration in the bulk of the semiconductor. The density of occupied surface states with illumination is given by $n_t^1 = -n_t^0 \frac{v_s^1}{v_s^0}$. Lagowski et al. [87] used these results to calculate the surface state parameters for basal and prismatic surfaces of CdS. They found a surface state at an energy level of 1.1 eV ($E_c - E_t$) for the prismatic surfaces that was not found on either the cadmium or sulfur surfaces that had been etched however on some of the mechanically polished cadmium and sulfur surfaces this surface state was observed. They attribute this surface state to surface defects that are probably intrinsic to the prismatic surfaces.

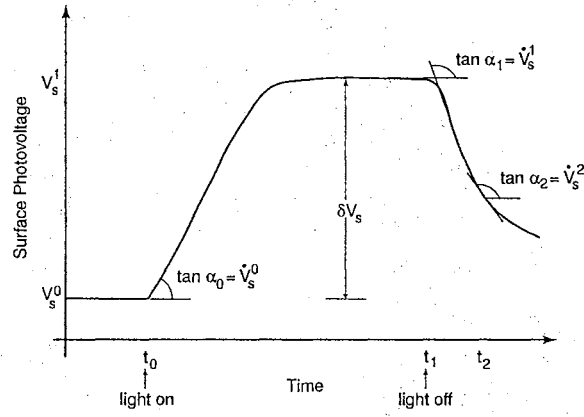


Figure 2.18: Schematic diagram of the time-dependent surface photovoltage response. After Balestra et al. [86].

Chapter 3

Experimental

This chapter presents methods for the preparation of the ZnO surfaces used in the experiments and the experimental procedure involved in evaluating the surfaces. The surface preparation techniques were chemomechanical polishing, etching and mechanical polishing with either $1/4\ \mu\text{m}$ or $1\ \mu\text{m}$ diamond abrasives. The principal technique used to investigate the near surface was nanoindentation which measures the near surface response to mechanical loading including elastic modulus and hardness. Scanning Kelvin probe microscopy was used to observe dislocation rosettes around indentations. Transmission electron microscopy (TEM) was used to determine the extent of near surface damage in some of the polished samples. Cross-sectional TEM samples were prepared at OSU and investigated at Los Alamos National Laboratory.

3.1 Sample preparation

Hexagonal (wurtzite) ZnO grown by the seeded chemical vapor transport (SCVT) method, and supplied by Eagle-Picher was used for all of the experiments. A ZnO crystal possesses two distinct polar faces normal to the $\langle 0001 \rangle$ axis, a Zn-terminated (0001) face (Zn face) and an O-terminated ($000\bar{1}$) face (O face). Both faces were studied in the present work. In addition, surfaces parallel to the prismatic planes, $\{10\bar{1}0\}$ and $\{11\bar{2}0\}$, were investigated. The samples had an etch pit density of $1 - 2 \times 10^5\ \text{cm}^{-2}$, and were of nominal dimensions $8 - 10\ \text{mm} \times 10\ \text{mm} \times 0.7\ \text{mm}$. The samples were not intentionally doped but were *n*-type with a carrier concentration on the order of $10^{17}\ \text{cm}^{-3}$. The purity of the ZnO samples was 99.9999 % or better as measured by glow discharge mass spectroscopy (GDMS) [88]. The major impurities, those over 10 parts per billion atomic (ppba), and their average concentration measured in six repeat measurements using four different

samples are shown in Table 3.1. The oriented wafers were sawn from a boule and then etched in 5 vol% trifluoroacetic acid (F_3CCOOH) and de-ionized H_2O ($15 \text{ M}\Omega\text{-cm}$) to remove about $25 \mu\text{m}$ from the saw-damaged surface. The wafers were processed on both sides by first lapping and then chemomechanical polishing. This provided flat, minimally damaged surfaces which could be then further processed. Lapping was performed using a commercial lapping machine with a cast iron wheel and a $9 \mu\text{m}$ Al_2O_3 /de-ionized H_2O slurry resulting in an additional $50 \mu\text{m}$ of material removal from each side. This was followed by chemomechanical polishing using a commercial polishing machine and a slurry of a 1:8 ratio of sodium hypochlorite:colloidal silica (9.1 pH). Approximately $25 \mu\text{m}$ of material from each side was removed under low load conditions of $1.7 \times 10^{-2} \text{ MPa}$. The (0001) surfaces were prepared with the following polishing preparations: 1) mechanical polishing with $1 \mu\text{m}$ diamond abrasive/de-ionized H_2O slurry, 2) mechanical polishing with $1/4 \mu\text{m}$ diamond abrasive/de-ionized H_2O slurry and 3) chemomechanical polishing as described above. Mechanical polishing was performed using a nylon pad and a pressure of $1.4 \times 10^{-2} \text{ MPa}$. Etched surfaces were prepared after chemomechanical polishing by etching in trifluoroacetic acid/de-ionized H_2O . The $(000\bar{1})$, $\{10\bar{1}0\}$ and $\{11\bar{2}0\}$ surfaces were prepared by chemomechanical polishing. Figure 3.1 shows an atomic force microscopy image of a chemomechanical polished (0001)ZnO surface. Typical surface roughnesses were $<1 \text{ nm rms}$ over a $1 \mu\text{m}^2$ scan area for the etched (0001) surfaces and all chemomechanically polished surfaces, and $<5 \text{ nm rms}$ for the mechanically polished surfaces.

Element	Concentration (ppba)
B	50
C	50
N	98
Na	16
Al	26
Si	528
Cl	29
Ga	83
In	30
Sn	23

Table 3.1: Major impurities in SCVT ZnO as measured by GDMS [88].

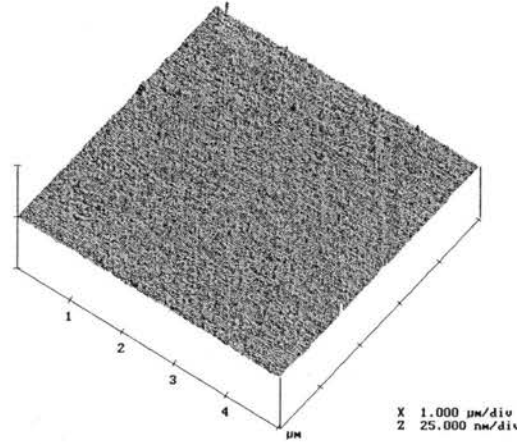


Figure 3.1: Atomic force microscopy image of chemomechanical polished (0001)ZnO with lateral dimensions $5\text{ }\mu\text{m} \times 5\text{ }\mu\text{m}$ and vertical dimension of 50 nm. The surface roughness is about 0.3 nm rms.

3.2 Nanoindentation

Nanoindentation was performed using a load-controlled commercial nanoindenter (Hysitron TriboScope®, Hysitron Inc.) in conjunction with an atomic force microscope system. The indentation system uses a three plate parallel capacitor to apply the load to the sample and to measure displacement. The resolution of the system is 1 nN for the vertical force and less than 1 nm for the vertical displacement. The maximum force is about 10 mN and the maximum indenter displacement is 20 μm . A Berkovich diamond indenter, Fig. 2.4, was used for all indentations. To obtain the area function of the indenter and frame compliance of the instrument, the system was calibrated by indenting into reference materials using the procedure outlined in Appendix A. Prior to performing each experiment, the instrument and sample were allowed to thermally equilibrate for 10 – 12 hours inside a thermal enclosure. The instrument's drift rate was checked before each indentation to confirm that it was less than 0.1 nm/sec averaged over a five second interval. The raw data were then corrected for the measured drift rate. Both single and multiple loading test cycles were performed, where single loading was used principally to investigate the initial stages of indentation, and multiple loading was used to investigate hardness and modulus dependence with penetration depth. Figure 3.2 shows a schematic diagram of the loading curves. The single loading sequence typically consisted of loading and unloading at 50 $\mu\text{N}/\text{sec}$ with a 5 sec hold at the peak load to allow any time dependent plastic effects to diminish. The multiple loading sequence consisted of loading and unloading for three successive times at 100 $\mu\text{N}/\text{sec}$ (500 $\mu\text{N}/\text{sec}$ for peak loads $>1000\text{ }\mu\text{N}$) with a 5 sec hold at the peak load and a 2 sec hold between loading sequences.

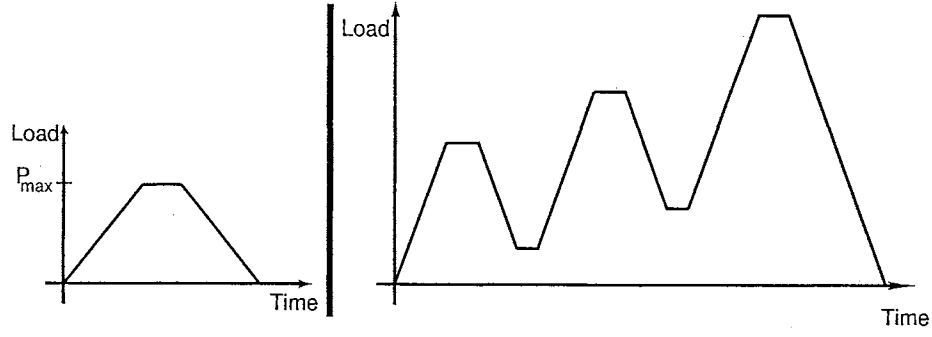


Figure 3.2: Single loading-unloading sequence for small indentations (left) and multiple loading-unloading sequence for larger indentations (right).

For nanoindentation experiments measuring the photoplastic effect and the surface photovoltage experiments the light source was a 30 W quartz-halogen fiber optic light. The light had three intensity settings and the power at each setting was measured with a Coherent LM10 power meter. To obtain the flux the measured power was divided by the area of the power meter detector. The measured flux of each setting was: low, 12 mW/cm²; medium, 20 mW/cm²; and high, 40 mW/cm²; unless otherwise stated the high setting was used for the experiments. The spectral characterization of the light was measured with a 0.5 m monochromator and the results are shown in Fig. 3.3. The small steps in the plot at higher wavelengths (> 520 nm) is an artifact of the measurement system. The intensity of light with wavelength shorter than the room temperature band gap of ZnO, approximately 380 nm, is small compared to the intensity of light with wavelength greater than 380 nm.

The nanoindentation experiments with illumination were performed as follows. Indentations

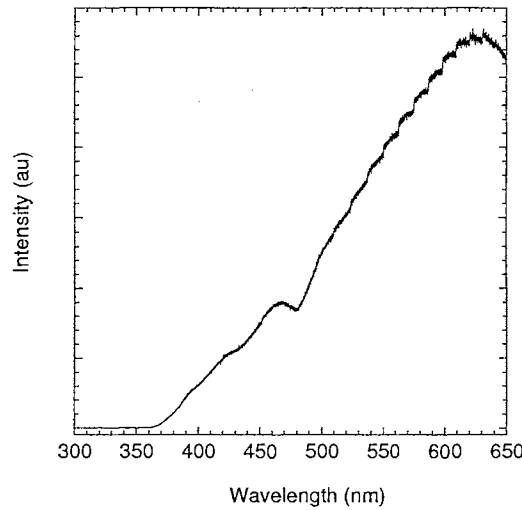


Figure 3.3: Spectrum of light used for photoplastic and surface photovoltage experiments.

in darkness, typically with a spacing of $20\ \mu\text{m}$ between indentations, were performed first. The sample was illuminated at least two hours prior to further indentation. The indentations with illumination were performed typically $20\ \mu\text{m}$ from the indentations that were made in darkness as shown in Fig. 3.4. The measured temperature increase inside the indentation enclosure caused by the light was about 6 K. For the surface photovoltage experiments the sample was typically scanned in darkness first and then immediately scanned with the sample illuminated.

3.3 Scanning Kelvin probe microscopy

Scanning Kelvin probe microscopy was performed using a commercial scanning probe microscope (DimensionTM 3100, Digital Instruments (now Veeco) Inc.). Two types of probes were initially used for the experiments, Co-Cr coated probes and n -Si probes. The Si probes had a carrier concentration of about $5 \times 10^{15}\ \text{cm}^{-3}$ and a nominal tip radius of 20 nm. For the surface photovoltage measurements, the Si probes were not used because the effect of the light on the probe would be convolved with any measured changes in the sample. The surface topography and the contact potential difference are obtained on two consecutive passes of the probe over the sample surface. On the first pass the surface topography is measured, on the second pass the probe is raised a user-defined amount and the contact potential difference is measured. For these experiments the probe was typically raised 30 nm above the surface. On the second pass a voltage, $V_{dc} + V_{ac} \sin(\omega t)$ is applied to the probe. Typically a value of 5 – 6 V was used for the component V_{ac} . The dc component, V_{dc} , was controlled by a feedback loop to null the force on the probe at frequency ω (Sec. 2.5).

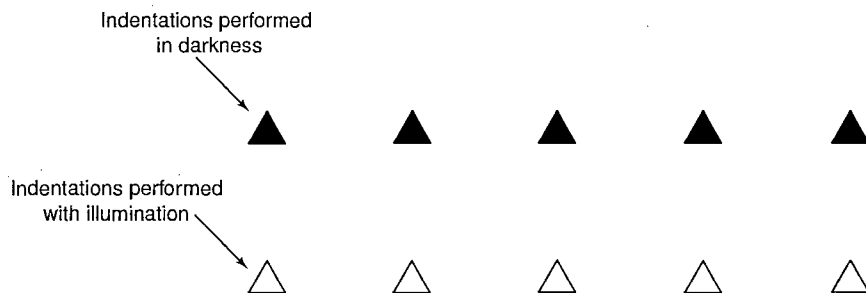


Figure 3.4: Schematic diagram of indentation pattern for indentations performed in darkness and with sample illumination. Typical spacing between indentations was $20\ \mu\text{m}$.

3.4 Sample preparation for transmission electron microscopy

Chemomechanical polished and $1/4\text{ }\mu\text{m}$ mechanical polished (0001)ZnO samples were prepared using standard preparation techniques. Briefly, the samples were cut to size with a wire saw and polished by hand using a Tripod polisher to hold the samples. The samples were polished on diamond impregnated films with successively smaller grit size from $30\text{ }\mu\text{m}$ grit size to $1\text{ }\mu\text{m}$ grit size. This reduced the sample thickness to about $80 - 100\text{ }\mu\text{m}$. The sample thickness was reduced to electron transparency using ion milling. Argon ions were used with an energy of 4.5 keV for rough milling and 3 keV for final milling.

Chapter 4

Results and Discussion

The near surface mechanical behavior of ZnO was investigated principally by nanoindentation. The effects of surface preparation on the near surface mechanical behavior were investigated for (0001)ZnO. The variation of the mechanical behavior with crystallographic direction was studied by comparing the results of chemomechanical polished (0001)ZnO with chemomechanical polished (000 $\bar{1}$), {10 $\bar{1}$ 0} and {11 $\bar{2}$ 0} surfaces. The changes in the near surface mechanical behavior with exposure to “white” light was investigated for etched (0001) surfaces and chemomechanical polished {10 $\bar{1}$ 0} surfaces. The structure of dislocations around indentations in chemomechanical polished (0001) and (000 $\bar{1}$) surfaces was studied using scanning Kelvin probe microscopy.

4.1 Effects of surface preparation on the near surface mechanical behavior

In order to study the effect of surface preparation on the mechanical behavior of ZnO nanoindentation experiments were performed on chemomechanical polished, 1/4 μm and 1 μm diamond abrasive mechanical polished, and etched (0001)ZnO. The surfaces were prepared as outlined in Sec. 3.1 and the data analyzed as in Sec. 2.2.1.

4.1.1 Comparison of hardness, elastic modulus, and pop-in

Figure 4.1 shows two indentations with a maximum load of 500 μN in chemomechanical polished and etched (0001) surfaces. The abrupt increase in penetration at a given load (P_{crit}), referred to as “pop-in” [89], has been observed in many semiconductors and metals as discussed in Sec. 2.2.2. For the etched and chemomechanically polished surfaces, pop-in was observed in all the experiments

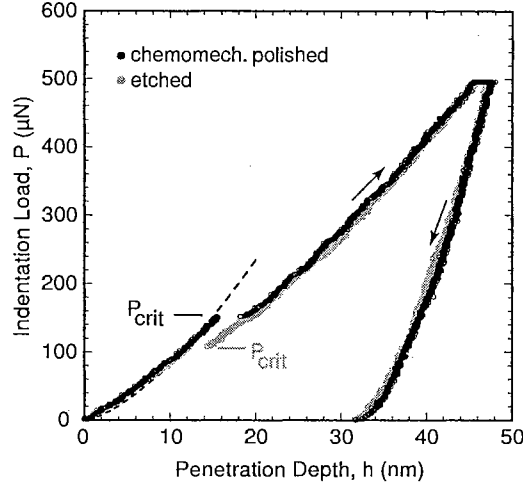


Figure 4.1: Load-depth curves obtained for chemomechanical polished (black circles) and etched (gray circles) (0001) surfaces.

performed, and the conditions of load and indentation depth at which it occurred were found to be highly repeatable. In all cases, pop-in occurred at a lower critical load for the etched surfaces ($118 \pm 11 \mu\text{N}$) as compared to the chemomechanically polished surfaces ($155 +4/-5 \mu\text{N}$), where the deviation from the average is expressed here as the maximum and minimum values obtained for five repeat indentations. The nature of the pop-in observed in ZnO can be examined by considering the initial portion of the loading curve. For indentations performed with a maximum load below the critical load at pop-in, the strain produced was found to be totally recoverable. This was confirmed by the fact that the loading curve was re-traced during unloading returning to zero indentation depth, and also by measurement of the surface topography immediately after indentation with the AFM which showed no residual impression. One can further examine the loading region prior to pop-in by considering the Hertzian solution for a non-rigid spherical indenter in contact with an elastic halfspace, i.e., $P = \frac{4}{3}E_r R^{1/2} h^{3/2}$ where R is the radius of the spherical indenter and E_r is the reduced elastic modulus given by

$$\frac{1}{E_r} = \frac{1 - \nu_s}{E_s} + \frac{1 - \nu_i}{E_i}.$$

For shallow indentations, the shape of the Berkovich indenter can be considered spherical, and its radius determined by matching the areas of an ideal sphere to that obtained by the calibration of the indenter tip. Using the measured elastic modulus and $R = 214 \text{ nm}$ as determined above, the loading region was found to follow the elastic solution, shown in Fig. 4.1 as the dashed line. This purely elastic behavior suggests that the release of strain energy at pop-in corresponds to a dislocation nucleation event [89], and the initial yield point. To further support this statement, one

can estimate the maximum shear stress under the indenter at the onset of pop-in using the same elastic solution above, which is given as [90]: $\tau_{\max} = (0.31/\pi)(6P_{\text{crit}}E_r^2/R^2)^{1/3}$. Using the measured values for P_{crit} one obtains values of τ_{\max} of 6.8 GPa for the (0001) etched surface and 7.2 GPa for the (0001) chemomechanically polished surface. A simple estimate of the theoretical shear stress required to cause interatomic slip, $\tau_{\text{theo}} = G/2\pi$ (where $G = 45.3 - 45.8$ GPa [31] is the reported aggregate average shear modulus of ZnO) results in a value of $\tau_{\text{theo}} = 7.2 - 7.3$ GPa and indicates agreement with the estimated maximum shear stress under the indenter. It is interesting to note that a defect density of $2 \times 10^5/\text{cm}^2$ (etch pit density $1 - 2 \times 10^5/\text{cm}^2$ for the crystals used in the study) implies the unlikelihood of encountering a defect during indentation at very small depths (2 nm total defect length per μm^3), which is consistent with the material's observed behavior as a defect free crystal.

Figure 4.2 shows two consecutive, neighboring indentations made on a chemomechanically polished surface; the presence of the first indentation was found to suppress the occurrence of pop-in in the second. The initial indentation which was made with a maximum load of 500 μN was seen to exhibit pop-in. When a second indentation was made which neighbored, but did not overlap the first, pop-in was not observed. The presence of dislocation sources produced by the first indentation, which provide nucleation sites for dislocation motion, is the likely cause. This result is consistent with the results of Miyahara [54] who also observed that a neighboring indentation suppressed the occurrence of pop-in during the nanoindentation of single crystal tungsten. Figure 4.2 also shows that the depth of penetration for the second indentation is less than that for the first indentation. This suggests that the hardness is higher for the second indentation which is most likely caused by the increase in dislocation density caused by the first indentation.

In Fig. 4.3, load-depth curves are shown for a (0001) surface which was chemomechanically polished and one which was mechanically polished with 1 μm diamond abrasive. In contrast to the chemomechanically polished surface, the initial loading curve for the mechanically polished surface does not follow elastic behavior, exhibiting plastic deformation from the very beginning of indentation. In addition, no pop-in event is observed. These results were found to be highly repeatable, and were seen for all experiments on the mechanically polished surfaces (both 1/4 μm and 1 μm diamond abrasive). Error bars using maximum and minimum values for five repeat indentations are shown at both the low and high end of loading. The immediate onset of plastic deformation and the absence of pop-in is again attributed to the presence of defects resultant from mechanical polishing. This is consistent with other observations of the suppression of pop-in with mechanical surface preparation [54,91].

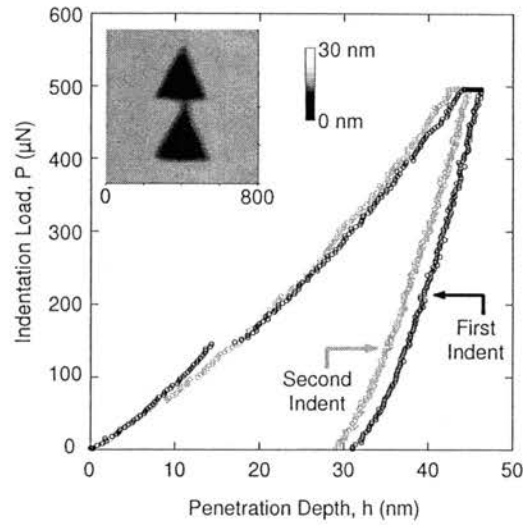


Figure 4.2: Two neighboring indentations made in chemomechanical polished (0001)ZnO. The first indentation (black circles) exhibited pop-in whereas the second (gray circles) did not.

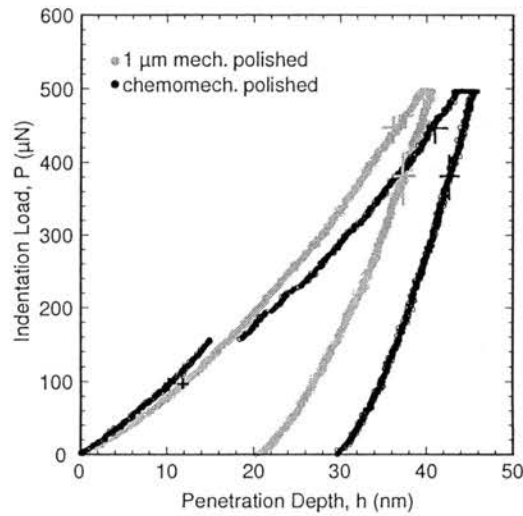


Figure 4.3: Load-depth curves for (0001) surfaces prepared by 1 μm mechanical polishing (gray circles) and chemomechanical polishing (black circles).

Hardness values obtained for the (0001) surfaces are shown in Fig. 4.4. The results are shown with respect to contact depth, h_c , the depth at which the indenter was in contact with the surface at the values of load and area used to calculate hardness. Hardness is seen to decrease with increasing depth for all surface preparations, referred to as the indentation size effect, and may have a physical basis as described by strain gradient plasticity [56], further explained in Sec. 2.2.3. The hardness at a given depth is seen to increase with increasing severity of surface preparation, ordered from the etched surface (minimally damaged), to chemomechanically polished, to mechanically polished with 1/4 μm abrasive and finally 1 μm abrasive (most damaged). The etched surface is minimally damaged because the chemical etchant preferentially reacts with material around dislocations. This leaves pits in the surface where dislocations were and outside the pits the near surface is free of dislocations however point defects and changes in the stoichiometry may exist in this region. Indentation was also performed on the chemomechanically polished (0001) surface at the maximum instrument load which corresponded to a depth of about 260 nm, and revealed an average value of 3.5 GPa indicating that hardness approached a constant value with increased depth. This value is consistent with the hardness reported by Regel et al. [24] of 3.9 GPa for the (0001) surface.

The indentation modulus was determined for all prepared surfaces over the same depth range as for the hardness. The indentation modulus is defined as $M_s = \left(\frac{1}{M_r} - \frac{1-\nu_i^2}{E_i} \right)^{-1}$ where M_r is the measured reduced indentation modulus and ν_i and E_i are Poisson's ratio and elastic modulus of the diamond indenter. Results at a depth of 150 nm are shown in Table 4.1. Surface preparation was seen to have no discernible effect on modulus (151 – 153 GPa) with the exception that the most

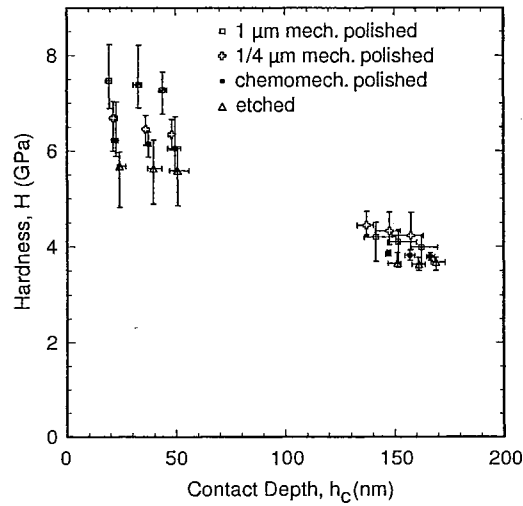


Figure 4.4: Hardness for (0001) surfaces with different surface preparations.

severe surface preparation (1 μm abrasive mechanical polished) exhibited a lower modulus (131 GPa). Overall, the measured values are consistent with the theoretical values shown in Table 2.6 with the inclusion of the piezoelectric effect ($M_s = 151 - 155$ GPa). Values obtained for depths of 50 nm for all surfaces were about 8% higher, but showed no trend with surface preparation. The lower value of indentation modulus for the 1 μm mechanical polished sample may in part be caused by a lowering of the piezoelectric effect. Zhao et al. [92] compared the measured piezoelectric coefficient (d_{33}) for bulk single crystal (0001)ZnO and ZnO nanobelts which were free from dislocations. They found that the ZnO nanobelts had a significantly higher piezoelectric coefficient and suggest that it may have been caused defects in the bulk ZnO but also state that it may have been cause by different boundary conditions. Further study is required to determine the cause for the lower indentation modulus of the 1 μm mechanical polished samples.

4.1.2 Transmission electron microscopy of prepared surfaces

Because the near surface indentation hardness was found to increase with increasing severity of surface preparation, more information about the near surface of the prepared samples was sought by using cross-sectional TEM. TEM samples were prepared at OSU as discussed in Sec. 3.4 for examination at Los Alamos National Laboratory. Results for (0001)ZnO samples prepared by chemomechanical polishing and 1/4 μm abrasive mechanical polishing are shown in Figs. 4.5 and 4.6. The chemomechanical polished sample shows no dislocations. The 1/4 μm abrasive mechanical polished sample shows non-uniform dislocations loops to a depth of 80 – 100 nm which is comparable to the depths obtained by ion channeling [19].

Preparation	Indentation Modulus of Sample, M_s (GPa)
etched	$151 \pm 7\%$
chemomechanical polished	$151 \pm 5\%$
1/4 μm mechanical polished	$153 \pm 3\%$
1 μm mechanical polished	$131 \pm 8\%$

Table 4.1: Indentation modulus of samples at a depth of 150 nm for (0001)ZnO with various surface preparations.

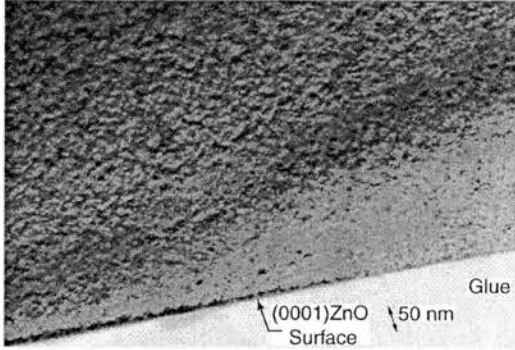


Figure 4.5: Cross-sectional TEM image of chemomechanical polished (0001)ZnO.

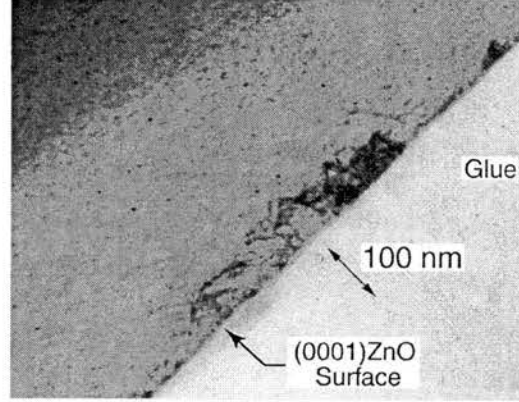


Figure 4.6: Cross-sectional TEM image of $1/4 \mu\text{m}$ mechanical polished (0001)ZnO. Dislocations extend approximately 80 nm below the surface.

4.2 Variation of near surface mechanical behavior with crystallographic orientation

To study how the near surface mechanical behavior varies with crystallographic orientation, (000 $\bar{1}$) chemomechanical polished, {10 $\bar{1}$ 0} chemomechanical polished and {11 $\bar{2}$ 0} chemomechanical polished surfaces were investigated. Indentation of the chemomechanical polished (000 $\bar{1}$) surface was performed with the same maximum indentation loads as the (0001) surface. All of the indentations in (000 $\bar{1}$) surfaces exhibited pop-in. The average load at which pop-in occurred was $151 \pm 17 \mu\text{N}$, where the deviation is one standard deviation obtained from 21 indentations. This is in agreement with the value obtained for the (0001) surface ($155 \pm 4/-5 \mu\text{N}$). Figure 4.7 shows a comparison of the hardness values obtained for the (000 $\bar{1}$) and (0001) surfaces for contact depth, h_c from about 20 nm to 260 nm. Hardness values for the two surfaces agree with each other at the shallow indentation depths and the deepest depth. For the indentations with a contact depth of 150 – 170 nm, the (0001) surface is slightly harder. Differences in hardness have been reported for other polar materials including, GaP [93], GaAs [94] and InSb [95]. Differences in hardness at the shallowest indentation depths, less than 60 nm, may not be observed because of scatter in the data. At the deepest indentation depth differences in the near surface may only contribute a small portion to measured hardness values. The indentation modulus for the (000 $\bar{1}$) surface at a depth of 150 nm was $152 \text{ GPa} \pm 10\%$ which is similar to the value obtained for the (0001) surface at this depth. The indentation modulus increased approximately 12% for a depth of 50 nm.

Figure 4.8 shows the load-depth curves obtained for a chemomechanically polished {10 $\bar{1}$ 0} sur-

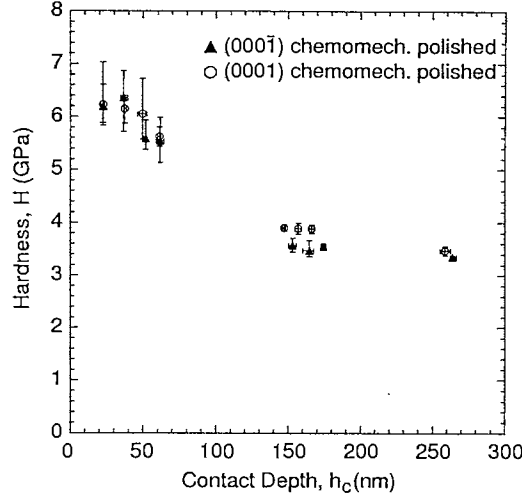


Figure 4.7: Comparison of hardness for chemomechanical polished (0001) and (0001 $\bar{1}$) surfaces.

face and a (0001) surface. Both surfaces exhibit pop-in at about the same critical load, however the lengths of the pop-in excursions differ significantly. The critical load for pop-in on the {10 $\bar{1}$ 0} surface was measured to be $169 \pm 30/-16 \mu\text{N}$. The average length of pop-in for the {10 $\bar{1}$ 0} surface is 9 nm compared to 4 nm for the (0001) surface. The longer pop-in length shows that the {10 $\bar{1}$ 0} surface is capable of accommodating more strain before dislocation motion is arrested by the opposing backstress created by dislocation pile-up [96]. The deeper penetration into the surface for the same applied maximum load illustrates lower hardness for the {10 $\bar{1}$ 0} surface. Deeper indentations confirmed this as well. Shown in Fig. 4.9 is a comparison of the (0001), {10 $\bar{1}$ 0} and the {11 $\bar{2}$ 0} chemomechanically polished surfaces. No discernible differences in pop-in, hardness or elastic modulus were measured between the {10 $\bar{1}$ 0} and the {11 $\bar{2}$ 0} surfaces.

Hardness values obtained for the {10 $\bar{1}$ 0} surface compared to (0001) surfaces are shown in Fig. 4.10. As was the case for the (0001) surfaces, the {10 $\bar{1}$ 0} surface exhibited the indentation size effect. The lower value of hardness for the {10 $\bar{1}$ 0} surface, indicated in Figs. 4.8 and 4.9 can also be seen here. Hardness values obtained for the {10 $\bar{1}$ 0} and {11 $\bar{2}$ 0} surfaces, showed no measurable difference. The measured value of hardness for the {10 $\bar{1}$ 0} surface at 190 nm of 2.1 GPa is also in agreement with the result of Regel et al. [24] of 2.0 GPa.

The indentation modulus was determined for the {10 $\bar{1}$ 0} and {11 $\bar{2}$ 0} surfaces over the same depth range as for the hardness. The indentation modulus at a depth of 126 nm was $151 \pm 7/+11 \text{ GPa}$ for both of these surfaces which was similar to that observed for the (0001) and (0001 $\bar{1}$) surfaces. The indentation modulus was about 9% higher at a depth of 62 nm which is also consistent with the results for the (0001) and (0001 $\bar{1}$) surfaces.

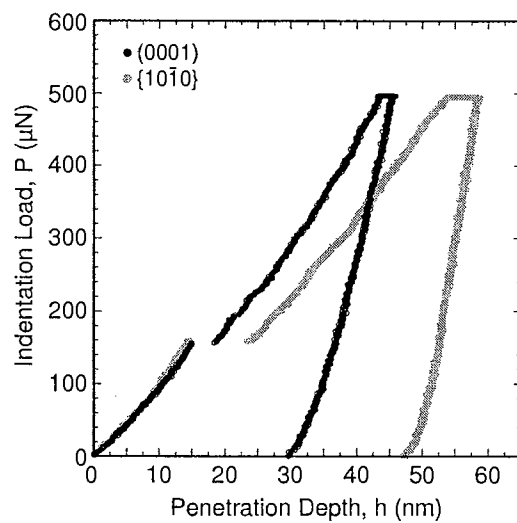


Figure 4.8: Comparison of load-depth curves for chemomechanical polished (0001) and $\{10\bar{1}0\}$ surfaces.

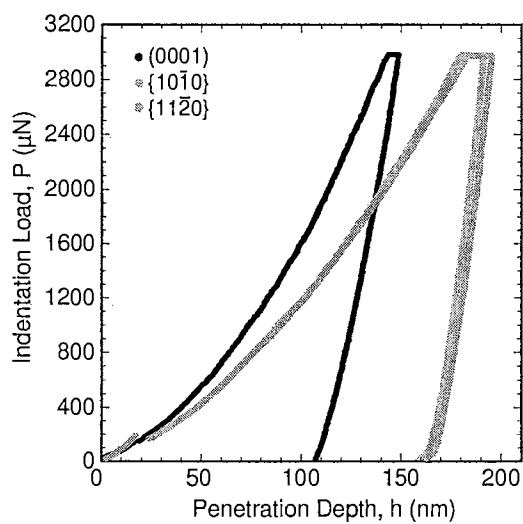


Figure 4.9: Load-depth curves for chemomechanical polished (0001), $\{10\bar{1}0\}$ and $\{11\bar{2}0\}$ surfaces.

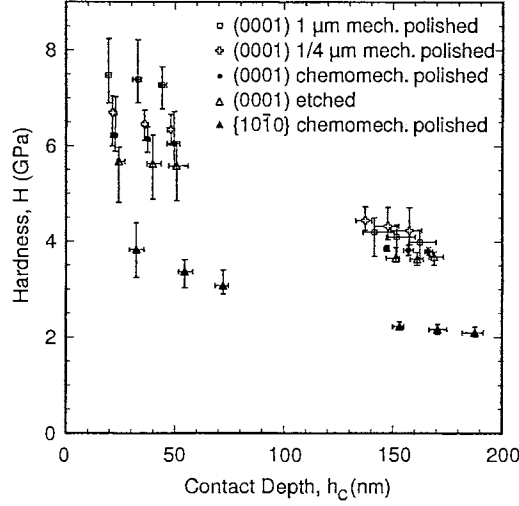


Figure 4.10: Hardness for (0001) and $\{10\bar{1}0\}$ surfaces.

4.3 Effects of illumination on the near surface mechanical behavior

Illumination is known to alter the hardness or flow stress of many bulk II-IV semiconductors as shown in Sec. 2.3, however only (111)ZnSe has been investigated in the near surface [22,61]. In this section the change in the near surface hardness of etched (0001)ZnO and chemomechanical polished $\{10\bar{1}0\}$ ZnO are reported. The light source used in the experiments was a quartz-halogen lamp with fiber optics. The intensity as a function of wavelength for this lamp is shown in Fig. 3.3, Sec. 3.2. The light source produced a flux of approximately 40 mW/cm² on the sample and the temperature rise caused by it was measured by a thermocouple in the indentation chamber to be less than 6 K.

Figure 4.11 shows two 500 μ N peak load indentations on the (0001) surface made with sample illumination and in darkness. In both cases pop-in is observed, (a) and (b) in Fig. 4.11. Single pop-in events were observed for all indentations. The average load and standard deviation at the onset of pop-in was $167 \pm 14 \mu$ N in darkness and $233 \pm 22 \mu$ N with sample illumination for fifteen indentations. A similar delay in the onset of plasticity with illumination was also observed by Wolf et al. [22] for the nanoindentation of (111)ZnSe. Although (111)ZnSe did not exhibit pop-in, there was a critical load below which no plastic deformation was observed. Existing models for the nucleation of dislocations during nanoindentation e.g., [97–100], are not able to explain the increase in load at pop-in which occurs during illumination. All of these models involve the stress state of the material and they do not address changes that could be caused by illumination. Figure 4.11 also shows less

indenter penetration with sample illumination implying an increase in the hardness with illumination i.e., a positive photoplastic effect (PPE).

Figure 4.12 shows hardness as a function of contact depth with sample illumination and in darkness. In both cases the indentation size effect, an increase in hardness with decreased indentation depth, is seen. The hardness in darkness was found to increase from an average of 3.1 GPa at a contact depth of 272 nm to an average of 5.6 GPa at a contact depth of 28 nm which is consistent with the previous results on etched (0001)ZnO. Hardness at the largest depth, 3.1 GPa, is consistent with 400 kg/mm² HV [24] (\approx 4.3 GPa) measured by microindentation. The hardness of the illuminated sample increased from an average value of 3.1 GPa at 274 nm to an average of 6.7 GPa at 24 nm. To a depth of 100 nm the hardness of the illuminated sample is found to be 7% to 20% greater than that measured in darkness. Beyond this depth no observable difference in hardness is found. The positive PPE is most often attributed to the charging of dislocations as they move through the crystal and acquire electrons from defects which have energy levels within the band gap [21]. The charged dislocations can then interact electrostatically with each other and/or the crystal lattice which can produce a hardening of the material [22]. For bulk II-VI materials, estimates of the length of travel needed for a dislocation to acquire equilibrium charge are about 10 μ m [21]. The present results are less than the 30% to 40% increase in flow stress observed in bulk compression tests of ZnO [60] however they are consistent with the 10% increase in near surface hardness observed in (111)ZnSe for similar illumination conditions [22]. The observation of a positive PPE effect at length scales significantly smaller than that required for dislocation charging was attributed by Wolf et al. [22]

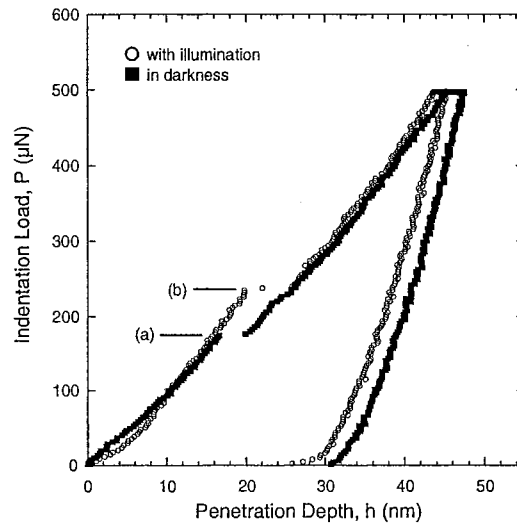


Figure 4.11: Comparison of indentations performed in etched (0001)ZnO with illumination and in darkness showing the load at pop-in (a) in darkness and (b) with illumination.

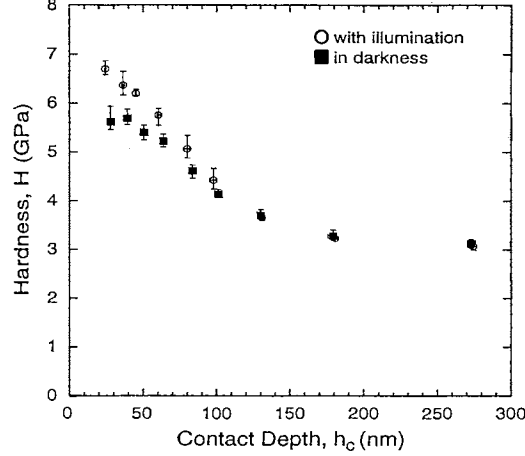


Figure 4.12: Hardness as a function of contact depth for etched (0001)ZnO with sample illumination (circles) and in darkness (squares). Error bars denote the minimum and maximum of the data.

to the much shorter dislocation travel distances required due to the high density of surface states which have energy levels within the band gap. We attribute the apparent absence of the PPE in the depth region greater than 100 nm to a reduced effect of the surface states on dislocation charging in this region and insufficient bulk charging resultant from short travel distances.

Figure 4.13 shows two 500 μN peak load indentations on the $\{10\bar{1}0\}$ surface made with sample illumination and in darkness. In both cases pop-in is observed, (a) and (b) in Fig. 4.13. For this surface single pop-in events were observed for all indentations performed in darkness however occasionally with the sample illuminated multiple pop-in events were observed. Because this only happened four times in approximately 30 indentations, the indentations with multiple pop-in events were excluded from further analysis. The average load and standard deviation at the onset of pop-in was $155 \pm 7 \mu\text{N}$ in darkness and $193 \pm 22 \mu\text{N}$ with sample illumination for fifteen indentations.

Figure 4.14 shows hardness as a function of contact depth for the $\{10\bar{1}0\}$ surface with sample illumination and in darkness. In both cases the indentation size effect is observed. The hardness in darkness was found to increase from an average of 1.4 GPa at a contact depth of 385 nm to an average of 3.3 GPa at a contact depth of 40 nm. Hardness at the largest depth, 1.4 GPa, is about half that of the measured hardness at the largest depth for the (0001) surface, 3.1 GPa. The hardness of the illuminated sample increased from an average value of 1.4 GPa at 388 nm to an average of 3.5 GPa at 39 nm. To a depth of about 130 nm the average hardness of the illuminated sample is found to be 4% to 9% greater than that measured in darkness. Beyond this depth no observable difference in hardness is found. The percent increase in hardness is less than that observed for the

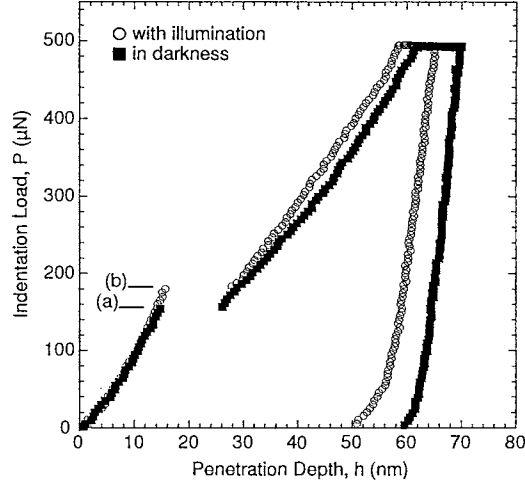


Figure 4.13: Comparison of indentations performed in chemomechanical polished $\{10\bar{1}0\}$ ZnO with illumination and in darkness showing the load at pop-in (a) in darkness and (b) with illumination.

(0001) surface and most likely is caused by differences in the charging of dislocations involved for the indentation on the different planes. Based on the rosette pattern shown in Sec. 4.4 and cross-sectional TEM of spherical nanoindentations [26], indentations on the (0001) surface most likely involve slip on the $\{0001\}$ and $\{10\bar{1}1\}$ or $\{10\bar{1}2\}$ planes. For indentation on the $\{10\bar{1}0\}$ surface, slip involves principally the $\{0001\}$ planes because these slip planes are perpendicular to the direction of indentation. A plausible explanation for the larger photoplastic effect observed on the $\{0001\}$ surface than the $\{10\bar{1}0\}$ surface is that dislocations on the $\{10\bar{1}1\}$ or $\{10\bar{1}2\}$ planes charge more than dislocations on the $\{0001\}$ planes.

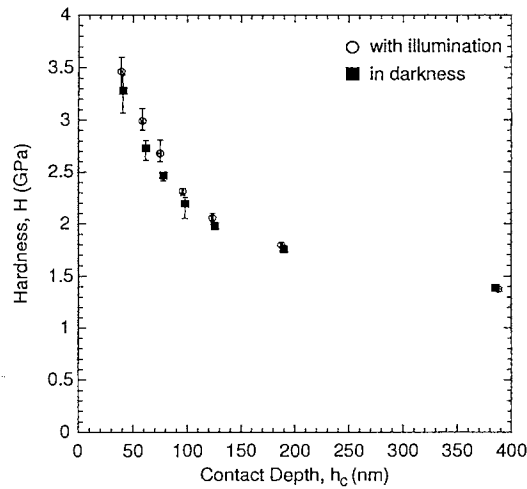


Figure 4.14: Hardness as a function of contact depth for chemomechanical polished $\{10\bar{1}0\}$ ZnO with sample illumination (circles) and in darkness (squares). Error bars denote the minimum and maximum of the data.

4.4 Use of scanning Kelvin probe microscopy to observe indentation dislocation rosettes

Indentation followed by chemical etching has long been used to study the plasticity of single crystals. Etch pits around the indentation form a pattern or “rosette” which provides information about the slip systems of the indented material. Other techniques to observe indentation dislocation rosettes include plan view and cross-sectional transmission electron microscopy (TEM) and cathodoluminescence (CL). In this section we demonstrate the use of scanning Kelvin probe microscopy with sample illumination by a quartz-halogen lamp to observe indentation rosettes in chemomechanical polished and etched $\{0001\}\text{ZnO}$.

Figure 4.15 shows the topography (top) and contact potential difference (bottom) around an indentation with a maximum load of $500\text{ }\mu\text{N}$ on a chemomechanical polished $(000\bar{1})\text{ZnO}$ surface acquired with the sample in darkness. The lateral size of the images is $5\text{ }\mu\text{m} \times 5\text{ }\mu\text{m}$ and the depth of the indentation is approximately 25 nm . The topography shows a mostly flat surface around the indentation with some debris near the bottom of the image. The roughness of the area excluding the indentation is about 1 nm rms . Slip lines, which have been observed around indentations in other materials such as $(100)\text{MgO}$ $[101]$, were not observed around indentations in ZnO . The contact potential difference does not show any pattern around the indentation however some of the debris does have a relatively low surface potential. For all contact potential difference figures the average value of the contact potential difference has been subtracted out so that small variations may be shown.

Figure 4.16 shows the topography (top) and contact potential difference (bottom) of the same indentation as in Fig. 4.15 however the measurements were obtained with the sample illuminated. The data in Fig. 4.16 was obtained immediately after the measurement in darkness. The topography of Fig. 4.16 shows that the scanning probe microscope scanner has moved slightly but the topography is otherwise the same as in Fig. 4.15. The contact potential difference shows a central zone of lower potential around the indentation and six arms emanating from the indentation. This rosette pattern is consistent with etch pit rosettes observed around Vickers microindentations on $(0001)\text{ZnO}$ $[102]$ and $(000\bar{1})\text{ZnO}$ $[24]$. The observed rosette pattern is also consistent with the rosette pattern around spherical nanoindentations in $(0001)\text{ZnO}$ observed by room-temperature monochromatic cathodoluminescence $[26]$. The direction of the rosette arms was determined by an indirect method. When $(0001)\text{ZnO}$ is etched in trifluoroacetic acid, aligned hexagonal etch pits form on the surface.

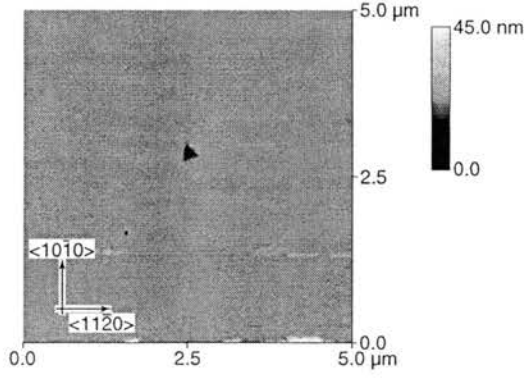


Figure 4.15: Topography (top figure) and contact potential difference (bottom figure) of a $(000\bar{1})\text{ZnO}$ indented surface measured in darkness. The location of the indentation is shown in the contact potential difference figure by the white triangle.

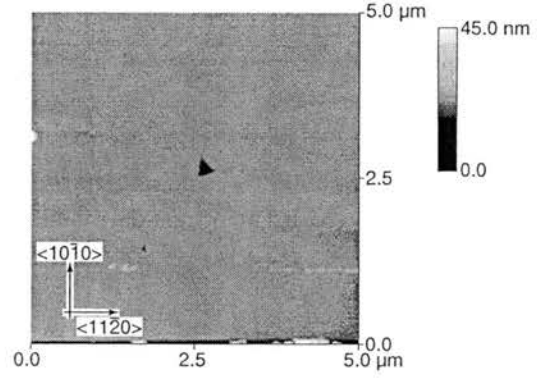


Figure 4.16: Topography (top figure) and contact potential difference (bottom figure) of a $(000\bar{1})\text{ZnO}$ indented surface measured with illumination. The location of the indentation is shown in the contact potential difference figure by the white triangle.

From previous back-reflection Laue measurements performed by our industrial partner, the edges of the hexagonal etch pits are known to be in the $\langle 11\bar{2}0 \rangle$ direction. After noting the direction of the rosette arms relative to the edge of the sample, the sample was etched in trifluoroacetic acid and the $\langle 11\bar{2}0 \rangle$ direction was ascertained. The rosette arms in Fig. 4.16 are aligned in the $\langle 11\bar{2}0 \rangle$ directions. The direction of the observed rosette arms is consistent with the results of Czernuszka and Pratt [29] who performed Vickers indentations at 200°C on $(0001)\text{ZnO}$ and observed the rosette with panchromatic cathodoluminescence. The observed direction of the rosette arms is consistent with two previously observed slip systems in ZnO. Bradby et al. [26] performed cross-sectional transmission electron microscopy on spherical nanoindentations in $(0001)\text{ZnO}$ and observed slip on the basal planes and the $\{10\bar{1}1\}$ planes. Czernuszka and Pratt [29] performed panchromatic cathodoluminescence on the cross-section of Vickers indentations and observed slip on the $\{10\bar{1}2\}$ planes. Figure 4.17 shows the $\{10\bar{1}1\}$ (GHM, in figure) and $\{10\bar{1}2\}$ (GHN, in figure) pyramidal

planes. Both the $\{10\bar{1}1\}$ and the $\{10\bar{1}2\}$ planes intersect the $\{0001\}$ planes along the $\langle 11\bar{2}0 \rangle$ directions and because of the two-dimensional nature of the SKPM measurement technique it can not be determined on which of these planes slip occurred.

Although impurity atom decoration effects of the dislocations around the indentation can not be ruled out as the cause of the change in the contact potential difference, we attribute the rosette pattern to band bending in the area around dislocations as in Read's model [77], Sec. 2.5. Simpkins et al. [103] and Koley and Spencer [104] used models similar to Read's to describe the contact potential difference near dislocations in GaN. Illumination is believed to increase the charging of dislocations and hence increase band bending by freeing electrons in surface states which are then attracted to acceptor sites of near surface dislocations, as was concluded for the case of the near surface photoplastic effect observed in the nanoindentation of $(0001)\text{ZnO}$ [105] and $(111)\text{ZnSe}$ [22]. Figures 4.15 and 4.16 show the results for a chemomechanical polished $(000\bar{1})$ surface, similar results were obtained for chemomechanical polished and etched (0001) surfaces. The rosette pattern remained for about 1 – 2 hours after the lamp had been turned off and the sample was in darkness. An after-effect was also observed in photoplastic compression tests of ZnO [60] which was on the order of tens of seconds. The after-effect in compression tests is believed to be caused by initially charged dislocations moving through the crystal and losing excess electrons to trapping centers [106]. In the SKPM experiments the charged dislocations are stationary and require more time to lose excess electrons.

To further investigate the rosette pattern, a set of indentations was made with maximum loads

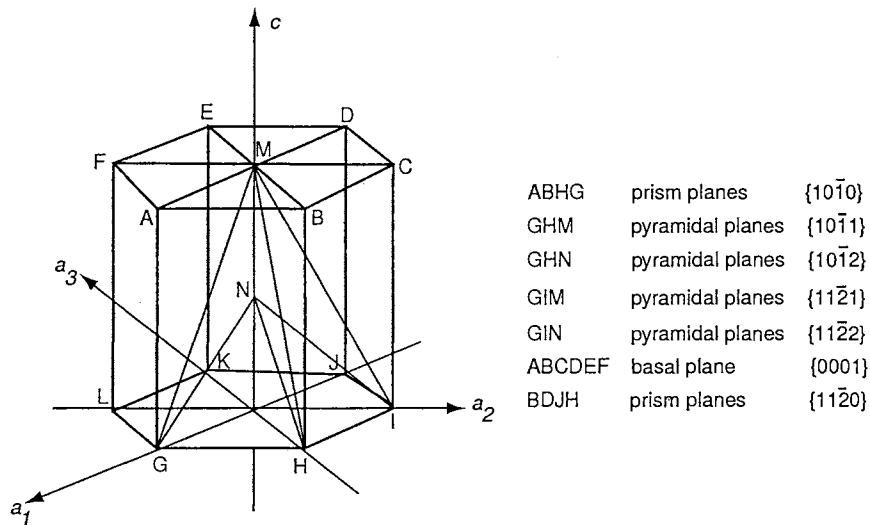


Figure 4.17: Schematic diagram of some planes in hexagonal material. After Honeycombe [20].

between 300 and 1500 μN on chemomechanical polished (000 $\bar{1}$)ZnO with two indentations made at each load. From a simplified version [107] of Johnson's [90] hemispherical hydrostatic model of elasto-plastic indentation, the plastic zone radius, c , is given by: $c = \sqrt{\frac{3F_{\text{max}}}{2\pi Y}}$ where F_{max} is the maximum indentation force and Y is the yield strength. The indentations on (000 $\bar{1}$) chemomechanical polished surfaces all exhibited pop-in, i.e., there is a well-defined elastic region before elasto-plastic deformation begins. To account for the elastic region, the maximum force in the above equation was replaced by the difference between the maximum force and the average load at which pop-in occurred. The plastic zone radius was approximated by the length of the longest rosette arm because there was less relative error in its measurement. There were errors in determining the center of the indentation and the end of the rosette arm which were the same for the shortest rosette arm and the longest so the percent error was smaller for the longest rosette arm. Figure 4.18 shows the length of the longest rosette arm as a function of the square root of the maximum indentation force minus the average load at pop-in and the best-fit line through the data. The y -intercept of the line is nearly zero ($-0.08 \mu\text{m}$) and from the slope a yield strength of 31 MPa is obtained. From compression test stress-strain data for ZnO obtained by Carlsson [108], one can estimate a yield strength of 50 – 60 MPa. Although the hemispherical hydrostatic model of indentation assumes the material is isotropic, it produces a yield strength that is of the correct order of magnitude.

Preliminary experiments on the time dependence of the surface photovoltage of the indentation rosette were performed to compare the regions of lower surface photovoltage (rosette arms) which

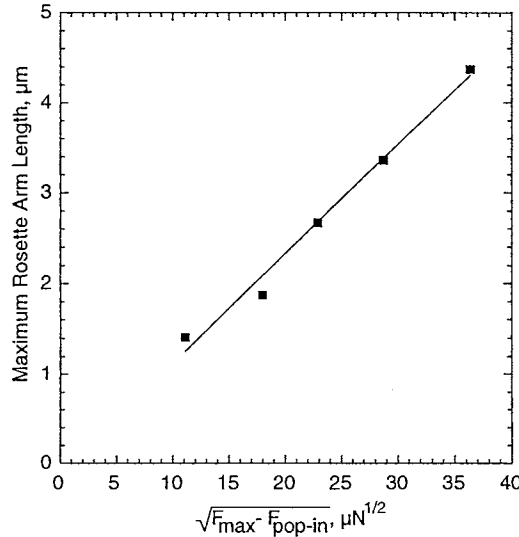


Figure 4.18: Length of longest rosette arm vs. the square root of the maximum load of indentation minus the average load a pop-in on (000 $\bar{1}$)ZnO.

have a higher density of dislocations to the regions with a higher surface photovoltage which are away from the rosette arms and have a lower density of dislocations. To examine the time dependence of the surface photovoltage the same area was scanned, to eliminate the normal variability of surface potential with location on the sample. This was achieved by setting the scanning probe microscope (SPM) to scan the same line repeatedly, thus the SPM measured the change of surface potential with time not location. The scan line was chosen such that it was away from the indentation and contained areas of both the rosette arm and the surrounding area, see Fig. 4.19. This allowed for a comparison of the area inside the rosette arm and outside the rosette arm. Using a scan rate of 0.4 Hz the scan lines were obtained at 5 sec intervals. The sample was an etched (0001) surface and the light source was the same quartz-halogen lamp as used in the rosette study above.

Figure 4.20 shows the measured average contact potential difference of the regions inside the rosette arm and outside the rosette arm as a function of time. The sample was illuminated at time $t = 0$. Before the sample was illuminated there was a difference of approximately 30 mV between the regions inside and outside the rosette arm. This difference was only observed on this occasion and is believed to be caused by stray laser light from the SPM measurement system that illuminated the sample. For both regions there was an increase in the contact potential difference starting at $t = 0$ and reached steady state at approximately $t = 350$ sec. The voltage increase inside the rosette arm was about 145 mV however the voltage increase outside the rosette arm was about 175 mV.

To understand these results a simple model of the near surface band structure can be used. The surface is presumed to have surface states which act as acceptors, as suggested by the work of Moormann et al. [109]. Dislocations are modeled as introducing an energy level within the band gap which acts as an acceptor as in Read's model [77]. To account for the difference in the density of dislocation in the rosette arm and outside of this region, the rosette arm is modeled as having dislocations and the region outside the rosette arm is modeled as not having any dislocations. Figures 4.21 and 4.22 show simplified band structure diagrams for the areas outside the rosette arm

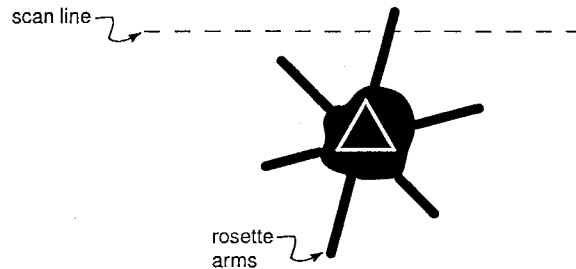


Figure 4.19: Schematic diagram of the approximate location of the scan line that was measured repeatedly throughout time-dependent surface photovoltage experiment.

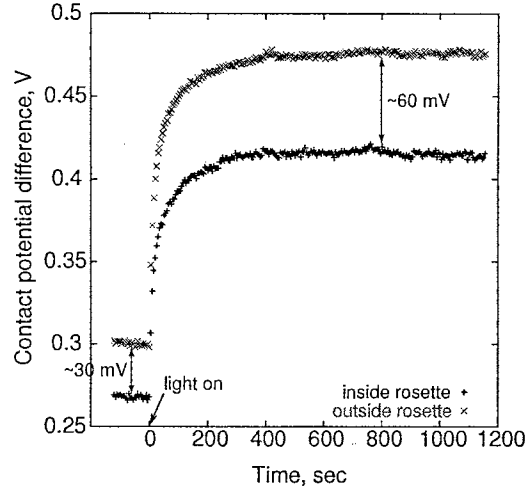


Figure 4.20: Measured contact potential difference in regions inside the rosette arm and outside the rosette arm as a function of the time after the sample was illuminated.

and inside the rosette arm. Figure 4.21(a) shows the band structure in the near surface without illumination in the region outside the rosette structure. The occupation of surface states by electrons causes the conduction and valence bands to bend upward in the near surface. With illumination, Fig. 4.21(b), some of the electrons that were in the surface states acquire enough energy from the incident photons to go into the conduction band which lessens the amount of band bending. A decrease in the amount of band bending causes an increase in the contact potential difference because the contact potential difference is the work function of the metal coated probe minus the sum of the band bending, electron affinity and Fermi level relative to the conduction band for ZnO. Figure 4.22 shows the band structure inside the rosette where there was a higher dislocation density. The dislocation energy level is believed to be partially occupied with electrons as shown by the slightly lower contact potential difference (0.27 V) than outside the rosette area (0.3 V). As previously mentioned, this was probably caused by stray laser light from the SPM measurement system. With illumination, Fig. 4.22(b), some of the electrons in the surface states acquire enough energy from the incident photons to go into the conduction band however some of these electrons are attracted to the acceptor sites of the dislocation. This causes the conduction and valence bands to flatten however not as much as in the region outside the rosette arms because of the electrons at the dislocation. The surface photovoltage decrease after the light was turned off was not recorded properly because there was some drift of the scanning head. Because the light source was a broad band light source, the analysis presented at the end of Sec. 2.5 can not be used however the results obtained suggest that this may be an interesting area of research to pursue.

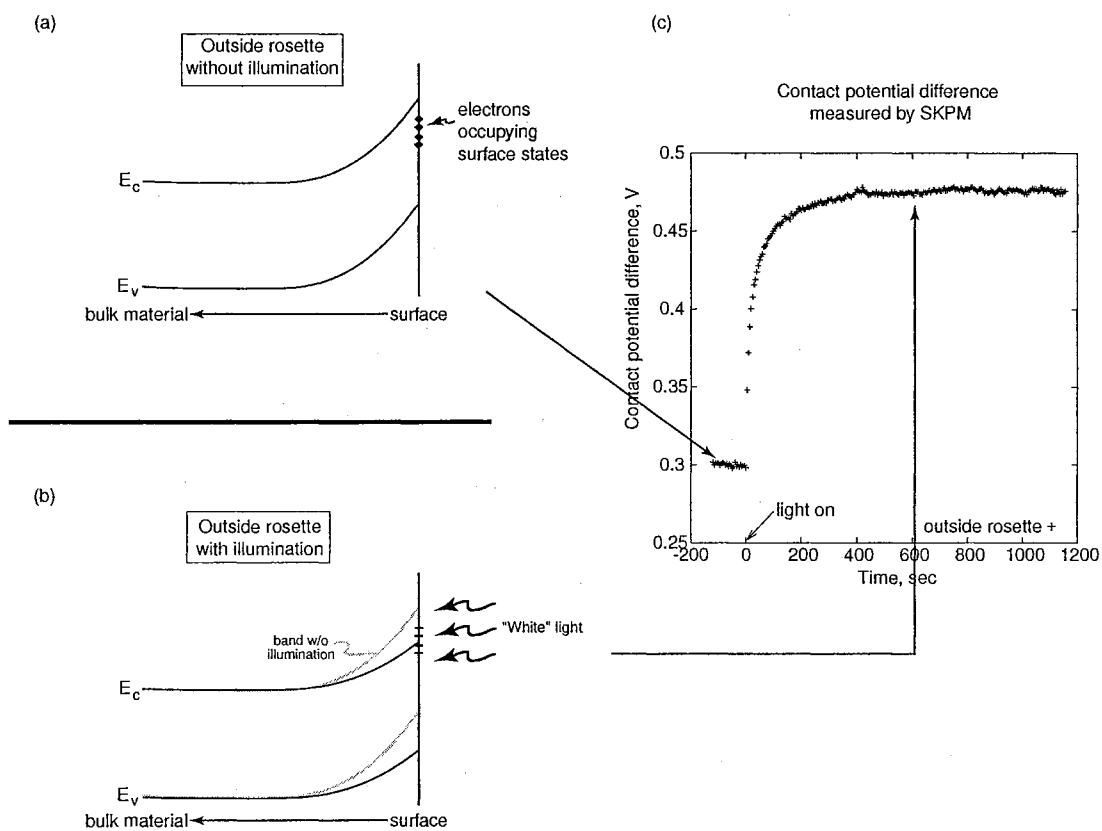


Figure 4.21: Simplified band structure diagram for the area outside the rosette. (a) shows the band structure in darkness and (b) with illumination. (c) shows the changes in the contact potential difference caused by the illumination.

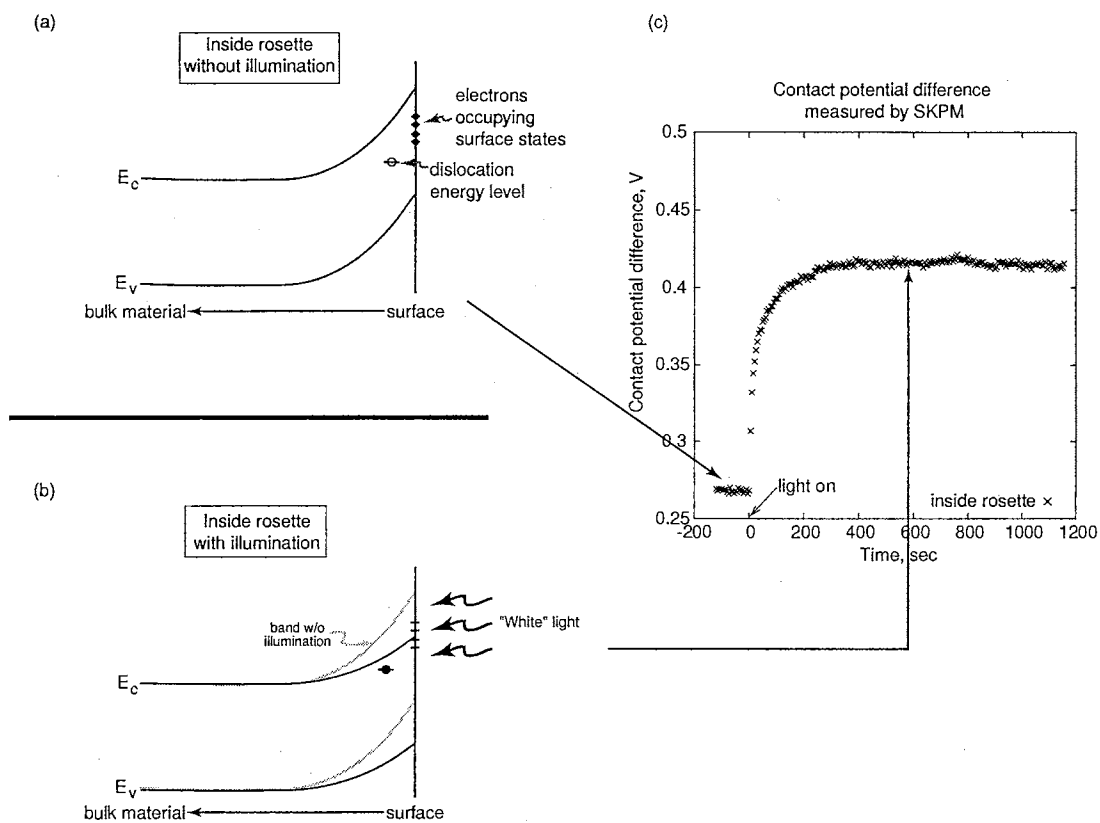


Figure 4.22: Simplified band structure diagram for the area inside the rosette. (a) shows the band structure in darkness and (b) with illumination. (c) shows the changes in the contact potential difference caused by the illumination.

Chapter 5

Conclusions and Future Work

5.1 Conclusions

The near surface mechanical behavior of ZnO has been investigated by nanoindentation. The studies included the effects of surface finish, variation of mechanical behavior with crystallographic direction and the effects of illumination. The use of scanning Kelvin probe microscopy with sample illumination as a technique to observe indentation dislocation rosettes was demonstrated.

1. Surfaces of (0001) ZnO crystals were prepared by mechanical polishing with $1/4\ \mu\text{m}$ and $1\ \mu\text{m}$ diamond abrasives, chemomechanical polishing and chemical etching. Pop-in was seen to occur for both the chemomechanical polished and etched surface but not for the mechanically polished surfaces. Pop-in was attributed to dislocation nucleation and the onset of yielding. The load at which pop-in occurred was found to be higher for the chemomechanically polished surface than the etched surface. Measured hardness values were found to be dependent on surface preparation, with an increased hardness observed with increased surface preparation severity, and also exhibited a near surface depth dependence. Hardness values obtained at the deepest indentation depths, approximately 260 nm, were consistent with previous results obtained by microindentation. Indentation modulus values showed no dependence with surface preparation with the exception of the $1\ \mu\text{m}$ abrasive mechanical polished surface which exhibited a lower modulus. The indentation modulus values were consistent with theoretical results obtained by including the piezoelectric effect of ZnO. Cross-sectional TEM results on the $1/4\ \mu\text{m}$ diamond abrasive mechanical polished (0001) surface showed dislocation loops extending to a depth of about 80 nm. No dislocations were observed for the chemomechanical polished (0001) surface.

2. The near surface mechanical behavior of chemomechanical polished $(000\bar{1})$ and prismatic planes were also investigated by nanoindentation. The indentation modulus, hardness and load at which pop-in occurred for the $(000\bar{1})$ were similar to the values obtained for the chemomechanical polished (0001) surface. The $\{10\bar{1}0\}$ and $\{11\bar{2}0\}$ surfaces exhibited pop-in at a load which was comparable to that on the polar surfaces however the displacement during pop-in was higher for the prismatic surfaces than the polar surfaces. Measured hardness values of the prismatic planes were about half of the values obtained for the (0001) surface over the depth range investigated, 50 – 260 nm, which is consistent with previous microindentation results. Indentation of the prismatic surfaces should involve principally slip on $\{0001\}$ planes which for many other hexagonal materials is the easiest slip plane. The indentation modulus of the prismatic surfaces was similar to that of the polar surfaces.

3. The effects of broad band illumination on the near surface mechanical response of etched (0001) surfaces and chemomechanical polished $\{10\bar{1}0\}$ surfaces were investigated. On both surfaces illumination was found to increase the load at which pop-in occurred and the near surface hardness. Illumination increased the load at which pop-in occurred on the (0001) surface approximately 40% above that obtained in darkness and approximately 25% on the $\{10\bar{1}0\}$ surface. Measured hardness for indentation depths up to about 100 nm increased 7 – 20% for the (0001) surface and 4 – 9% for the $\{10\bar{1}0\}$ surface. Beyond this depth no differences in hardness were measured. The increase in hardness of the near surface with illumination is attributed to charging of dislocations from surface states. The difference between the increase of hardness for the (0001) and $\{10\bar{1}0\}$ surfaces is probably caused by different slip systems involved for the two cases.

4. The use of scanning Kelvin probe microscopy with sample illumination to observe indentation rosettes was shown. The rosette pattern consisted of regions with a lower surface potential consisting of a central zone around the indentation and six arms emanating along the $\langle 11\bar{2}0 \rangle$ directions. These directions are consistent with slip on the $\{10\bar{1}1\}$ or $\{10\bar{1}2\}$ planes which had been identified in previous indentation studies of ZnO. The length of the longest rosette arm was found to be proportional to the square root of the maximum indentation force minus the average load at pop-in. Preliminary results on the time dependence of the surface potential in the rosette arm and outside of the rosette were also presented.

5.2 Proposed future work

- On the (0001) surface the indentation modulus for the 1 μm abrasive mechanical polish sample was lower than the other surface preparations. Although a reduction of the piezoelectric effect because of damage in the near surface could account for some of the lower modulus, this could not account for all of the measured effect. Indentations on another batch of samples may show that these samples had an anomalously low modulus.
- The cross-sectional TEM of the 1/4 μm abrasive mechanical polish sample showed dislocation loops extending to about 80 nm below the surface. Further TEM analysis of this sample could identify the slip systems of the dislocations.
- To identify slip systems involved during nanoindentation of the polar and prismatic surfaces focused ion beam milling could be used to prepare cross-sectional TEM samples of the indentations.
- The increase of the load at which pop-in occurs with illumination is an interesting result that requires further study. Currently there is not agreement on the conditions which give rise to dislocation nucleation however all of the existing models do not include anything related to illumination.
- The use of scanning Kelvin probe microscopy around indentations on $\{10\bar{1}0\}$ and $\{11\bar{2}0\}$ ZnO surfaces could be used to observe the rosette pattern. The rosette pattern on these surfaces will probably be different than the rosette pattern on the (0001) surface because of different slip systems being activated. SKPM could also be used to observe indentation rosettes on other semiconductors such as GaN and GaAs. The time dependence of the contact potential difference after illumination with a laser could be used to measure quantitative differences between the regions inside the rosette and outside the rosette. These differences include the density of surface states, surface state occupation, electronic cross-section and photonic cross-section.

Bibliography

- [1] T. E. Mitchell and A. H. Heuer. Dislocations and mechanical properties of ceramics. In F. R. N. Nabarro and J. P. Hirth, editors, *Dislocations in Solids*, volume 12. Elsevier Science, 2004.
- [2] D. C. Look. Recent advances in ZnO materials and devices. *Materials Science and Engineering B*, 80:383–387, 2001.
- [3] F. Hamdani, M. Yeadon, D. J. Smith, H. Tang, W. Kim, A. Salvador, A. E. Botchkarev, J. M. Gibson, A. Y. Polyakov, M. Skowronski, and H. Morkoç. Microstructure and optical properties of epitaxial GaN on ZnO (0001) grown by reactive molecular beam epitaxy. *Journal of Applied Physics*, 83(2):983–990, 1998.
- [4] X. Gu, M. A. Reshchikov, A. Teke, D. Johnstone, H. Morkoç, B. Nemeth, and J. Nause. GaN epitaxy on thermally treated c-plane bulk ZnO substrates with O and Zn faces. *Applied Physics Letters*, 84(13):2268–2270, 2004.
- [5] X. Gu, S. Sabuktagin, A. Teke, D. Johnstone, H. Morkoç, B. Nemeth, and J. Nause. Effect of thermal treatment on ZnO substrate for epitaxial growth. *Journal of Materials Science: Materials in Electronics*, 15:373–378, 2004.
- [6] R. Khanna, K. Ip, K. K. Allums, K. Baik, C. R. Abernathy, S. J. Pearton, Y. W. Heo, D. P. Norton, F. Ren, R. Dwivedi, T. N. Fogarty, and R. Wilkins. Effects of high dose proton irradiation on the electrical performance of ZnO Schottky diodes. *physica status solidi (a)*, 201(12):R79–R82, 2004.
- [7] M. Kadota and H. Kando. Small and low-loss IF SAW filters using zinc oxide film on quartz substrate. *IEEE Transactions on Ultrasonics, Ferroelectrics, and Frequency Control*, 51(4):464–469, 2004.
- [8] J. Molarius, J. Kaitila, T. Pensala, and M. Ylilammi. Piezoelectric ZnO films by r.f. sputtering. *Journal of Materials Science: Materials in Electronics*, 14:431–435, 2003.

- [9] R. L. Hoffman, B. J. Norris, and J. F. Wager. ZnO-based transparent thin-film transistors. *Applied Physics Letters*, 82(5):733–735, 2003.
- [10] K. Tamura, K. Nakahara, M. Sakai, D. Nakagawa, N. Ito, M. Sonobe, H. Takasu, H. Tampo, P. Fons, K. Matsubara, K. Iwata, A. Yamada, and S. Niki. InGaN-based light emitting diodes fabricated with transparent Ga-doped ZnO as ohmic *p*-contact. *physica status solidi (a)*, 201(12):2704–2707, 2004.
- [11] B. Sang, K. Dairiki, A. Yamada, and M. Konagai. High-efficiency amorphous silicon solar cells with ZnO as front contact. *Japanese Journal of Applied Physics*, 38:4983–4988, 1999.
- [12] I.-S. Jeong, J. H. Kim, and S. Im. Ultraviolet-enhanced photodiode employing *n*-ZnO/*p*-Si structure. *Applied Physics Letters*, 83(14):2946–2948, 2003.
- [13] Ya. I. Alivov, J. E. Van Nostrand, D. C. Look, M. V. Chukichev, and B. M. Ataev. Observation of 430 nm electroluminescence from ZnO/GaN heterojunction light-emitting diodes. *Applied Physics Letters*, 83(14):2943–2945, 2003.
- [14] D. C. Reynolds, D. C. Look, B. Jogai, C. W. Litton, T. C. Collins, W. C. Harsch, and G. Cantwell. Neutral-donor-bound-exciton complexes in ZnO crystals. *Physical Review B*, 57(19):12151, 1998.
- [15] R. E. Sherrieff, D. C. Reynolds, D. C. Look, B. Jogai, J. E. Hoelscher, T. C. Collins, G. Cantwell, and W. C. Harsch. Photoluminescence measurements from the two polar faces of ZnO. *Journal of Applied Physics*, 88:3454–3457, 2000.
- [16] D. A. Lucca, D. W. Hamby, M. J. Klopstein, G. Cantwell, C. J. Wetteland, J. R. Tesmer, and M. Nastasi. Effects of polishing on the photoluminescence of single crystal ZnO. *Annals of the CIRP*, 50:397–400, 2001.
- [17] D. A. Lucca, D. W. Hamby, M. J. Klopstein, and G. Cantwell. Chemomechanical polishing effects on the room temperature photoluminescence of bulk ZnO: Exciton-LO phonon interaction. *physica status solidi (b)*, 229:845–848, 2002.
- [18] D. W. Hamby, D. A. Lucca, M. J. Klopstein, and G. Cantwell. Temperature dependent exciton photoluminescence of bulk ZnO. *Journal of Applied Physics*, 93:3214–3217, 2003.
- [19] D.A. Lucca, M.J. Klopstein, G. Cantwell, C.J. Wetteland, J.R. Tesmer, and M. Nastasi. Ion channeling study of subsurface damage in polished ZnO. In P.M. Lonardo, editor, *PRIME 2001*, pages 359–362, Genoa, Italy, 2001.

- [20] R. W. K. Honeycombe. *The Plastic Deformation of Metals*. Edward Arnold (Publishers) Ltd., London, 2nd edition, 1984.
- [21] Yu. A. Osip'yan, V. F. Petrenko, A. V. Zaretskii, and R. W. Whitworth. Properties of II-VI semiconductors associated with moving dislocations. *Advances In Physics*, 35(2):115–188, 1986.
- [22] B. Wolf, A. Belger, D. C. Meyer, and P. Paufler. On the impact of light on nanoindentation of ZnSe. *physica status solidi (a)*, 187(2):415–426, 2001.
- [23] E. Dieulesaint and D. Royer. *Elastic Waves in Solids – Applications to Signal Processing*. John Wiley and Sons, New York, 1980.
- [24] V. R. Regel, N.L. Sizova, M.A. Chernysheva, S.I. Dohnovskaya, I.P. Kuzmina, O.A. Lazarevskaya, and V.A. Nikitenko. Microhardness and resistivity anisotropy of ZnO plastic deformation. *Crystal Research and Technology*, 17:1579–1584, 1982.
- [25] S. O. Kucheyev, J. E. Bradby, J. S. Williams, C. Jagadish, and M. V. Swain. Mechanical deformation of single-crystal ZnO. *Applied Physics Letters*, 80:956–958, 2002.
- [26] J. E. Bradby, S. O. Kucheyev, J. S. Williams, C. Jagadish, M. V. Swain, P. Munroe, and M. R. Phillips. Contact-induced defect propagation in ZnO. *Applied Physics Letters*, 80:4537–4539, 2002.
- [27] ISO 14577: Metallic materials – Instrumented indentation test for hardness and materials parameters. *International Organization for Standardization*, 2002.
- [28] J. S. Ahearn, J. J. Mills, and A. R. C. Westwood. Effect of electrolyte pH and bias voltage on the hardness of the (0001) ZnO surface. *Journal of Applied Physics*, 49:96–102, 1978.
- [29] J. T. Czernuszka and N. Pratt. Cathodoluminescence-mode imaging of dislocations in zinc oxide. *Philosophical Magazine Letters*, 61:83–90, 1990.
- [30] T. B. Bateman. Elastic moduli of single-crystal zinc oxide. *Journal of Applied Physics*, 33:3309–3312, 1962.
- [31] G. Simmons and H. Wang. *Single Crystal Elastic Constants and Calculated Aggregate Properties: A Handbook*. MIT Press, Cambridge, 1971.
- [32] L. B. Kobiakov. Elastic, piezoelectric and dielectric properties of ZnO and CdS single crystals in a wide range of temperatures. *Solid State Communications*, 35(3):305–310, 1980.

- [33] J. S. Field and M. V. Swain. A simple predictive model for spherical indentation. *Journal of Materials Research*, 8(2):297–305, 1993.
- [34] A. C. Fischer-Cripps. A review of analysis methods for sub-micron indentation testing. *Vacuum*, 58:569–585, 2000.
- [35] W. C. Oliver and G. M. Pharr. An improved technique for determining hardness and elastic modulus using load and displacement sensing indentation experiments. *Journal of Materials Research*, 7:1564–1583, 1992.
- [36] V. Alberts, J. H. Neethling, and A. W. Leitch. Correlation between structural, optical, and electrical properties of GaAs grown on (001) Si. *Journal of Applied Physics*, 75:7258–7265, 1994.
- [37] P. Girault, J. F. Barbot, and C. Blanchard. Electrical property of n-Hg_{0.8}Cd_{0.2}Te plastically deformed. *Journal of Materials Science Letters*, 14:449–451, 1995.
- [38] K. Guergouri, N. Brihi, and R. Triboulet. Study of the effect of dislocations introduced by indentation on Cd(111) and Te(111) faces on the electrical and optical properties of CdTe. *Journal of Crystal Growth*, 209:709–715, 2000.
- [39] I. N. Sneddon. The relation between load and penetration in the axisymmetric Boussinesq problem for a punch of arbitrary profile. *International Journal of Engineering Science*, 3:47–57, 1965.
- [40] J. J. Vlassak and W. D. Nix. Measuring the elastic properties of anisotropic materials by means of indentation experiments. *Journal of the Mechanics and Physics of Solids*, 42(8):1223–1245, 1994.
- [41] J. J. Vlassak, M. Ciavarella, J. R. Barber, and X. Wang. The indentation modulus of elastically anisotropic materials for indenters of arbitrary shape. *Journal of the Mechanics and Physics of Solids*, 51:1701–1721, 2003.
- [42] J. G. Swadener, B. Taljat, and G. M. Pharr. Measurement of residual stress by load and depth sensing indentation with spherical indenters. *Journal of Materials Research*, 16:2091–2102, 2001.
- [43] J. J. Vlassak and W. D. Nix. Indentation modulus of elastically anisotropic half spaces. *Philosophical Magazine A*, 67(5):1045–1056, 1993.

- [44] H. A. Elliott. Three-dimensional stress distributions in hexagonal aeolotropic crystals. *Cambridge Philosophical Society*, 44:522–533, 1948.
- [45] H. A. Elliott. Axial symmetric stress distribution in aeolotropic hexagonal crystals. the problem of the plane and related problems. *Proceedings of the Cambridge Philosophical Society*, 45:621–630, 1949.
- [46] M. T. Hanson. The elastic field for conical indentation including sliding friction for transverse isotropy. *Journal of Applied Mechanics*, 59:S123–S130, 1992.
- [47] I. N. Sneddon. Fourier-transform solution of a Boussinesq problem for a hexagonally aeolotropic elastic half-space. *Quarterly Journal of Mechanics and Applied Mathematics*, 45(4):607–616, 1992.
- [48] I. N. Sneddon. *Fourier Transforms*. Dover, New York, 1951.
- [49] B.A. Kudriavtsev, V.Z. Parton, and V.I. Rakitin. Fracture mechanics of piezoelectric materials. axisymmetric crack on the boundary with a conductor. *Journal of Applied Mathematics and Mechanics (Prikladnaya Matematika i Mekhanika)*, 39(2):328–338(352–362), 1975.
- [50] G. M. Pharr, W. C. Oliver, and F. R. Brotzen. On the generality of the relationship among contact stiffness, contact area, and elastic modulus during indentation. *Journal of Materials Research*, 7(3):613–617, 1992.
- [51] S. Matysiak. Axisymmetric problem of punch pressing into a piezoelectroelastic halfspace. *Bulletin of the Polish Academy of Sciences Technical Series*, 33(1-2):25–33, 1985.
- [52] A. E. Giannakopoulos and S. Suresh. Theory of indentation of piezoelectric materials. *Acta Materialia*, 47(7):2153–2164, 1999.
- [53] H. S. Leipner, D. Lorenz, A. Zeckzer, and P. Grau. Dislocation-related pop-in effect in gallium arsenide. *physica status solidi (a)*, 183:R4–R6, 2001.
- [54] K. Miyahara, S. Matsuoka, and N. Nagashima. Nanoindentation measurement for a tungsten (001) single crystal. *JSME International Journal A*, 41(4):562–568, 1998.
- [55] K. Sangwal. On the reverse indentation size effect and microhardness measurement of solids. *Materials Chemistry and Physics*, 63:145–152, 2000.
- [56] Q. Ma and D. R. Clarke. Size dependent hardness of silver single crystals. *Journal of Materials Research*, 10:853–863, 1995.

- [57] N. A. Fleck, G. M. Muller, M. F. Ashby, and J. W. Hutchinson. Strain gradient plasticity: theory and experiment. *Metallurgica Materialia*, 42:475–487, 1994.
- [58] N. A. Fleck and J. W. Hutchinson. A reformulation of strain gradient plasticity. *Journal of the Mechanics and Physics of Solids*, 49:2245–2271, 2001.
- [59] M. F. Ashby. The deformation of plastically non-homogeneous materials. *Philosophical Magazine*, 21:399–424, 1970.
- [60] L. Carlsson and C. Svensson. Increase of flow stress in ZnO under illumination. *Solid State Communications*, 7:177–179, 1969.
- [61] B. Wolf, D. Meyer, A. Belger, and P. Paufler. Photoplastic effects in nanoindentation experiments. *Philosophical Magazine A*, 82(10):1865–1872, 2002.
- [62] K. Guergouri, E. Teyar, and R. Triboulet. Study of the effect of polarity and of dislocations on the electrical and optoelectronic properties of p-type $\text{Cd}_{0.96}\text{Zn}_{0.04}\text{Te}$. *Journal of Crystal Growth*, 216:127–133, 2000.
- [63] T. Behr, D. Hommel, H. Cerva, J. Nürnberger, V. Beyersdorfer, and G. Landwehr. Structural and electrical properties of ZnSe laser diodes optimized by transmission electron microscopy, reflection high energy electron diffraction, X-ray diffraction and C-V profiling. *Journal of Crystal Growth*, 150:743–748, 1995.
- [64] D. Hommel, B. Jobst, T. Behr, G. Bilger, V. Beyersdorfer, E. Kurtz, and G. Landwehr. Correlation between electrical and structural properties of chlorine doped ZnSe epilayers grown by molecular beam epitaxy. *Journal of Crystal Growth*, 138:331–337, 1994.
- [65] M. Yasutake, D. Aoki, and M. Fujihira. Surface potential measurement using the Kelvin probe force microscope. *Thin Solid Films*, 273:279–283, 1996.
- [66] M. Nonnenmacher, M. P. O’Boyle, and H. K. Wickramasinghe. Kelvin probe force microscopy. *Applied Physics Letters*, 58:2921–2923, 1991.
- [67] A. Efimov and S. R. Cohen. Simulation and correction of geometric distortions in scanning Kelvin probe microscopy. *Journal of Vacuum Science and Technology A*, 18(4):1051–1055, 2000.
- [68] T. Usunami, M. Arakawa, S. Kishimoto, T. Mizutani, T. Kagawa, and H. Iwamura. Cross-sectional potential imaging of compound semiconductor heterostructure by Kelvin probe force microscopy. *Japanese Journal of Applied Physics*, 37:1522–1526, 1998.

- [69] G. H. Buh, H. J. Chung, C. K. Kim, J. H. Yi, I. T. Yoon, and Y. Kuk. Imaging of a silicon pn junction under applied bias with scanning capacitance microscopy and Kelvin probe force microscopy. *Applied Physics Letters*, 77(1):106–108, 2000.
- [70] L. Kelvin. Contact electricity of metals. pages 82–120, 1897.
- [71] O. Vatel and M. Tanimoto. Kelvin probe force microscopy for potential distribution measurement of semiconductor devices. *Journal of Applied Physics*, 77:2358–2362, 1995.
- [72] B. Bhushan and A. V. Goldade. Kelvin probe microscopy measurements of surface potential change under wear at low loads. *Wear*, 244:104–117, 2000.
- [73] M. Saint Jean, S. Hudlet, C. Guthmann, and J. Berger. Van der Waals and capacitive forces in atomic force microscopy. *Journal of Applied Physics*, 86(9):5245–5248, 1999.
- [74] S. M. Sze. *Physics of Semiconductor Devices*. Wiley, New York, 2nd edition, 1981.
- [75] J. M. R. Weaver and H. K. Wickramasinghe. Semiconductor characterization by scanning force microscope surface photovoltage microscopy. *Journal of Vacuum Science and Technology B*, 9(3):1562–1565, 1991.
- [76] G. Koley and M. G. Spencer. Surface potential measurements on GaN and AlGaIn/GaN heterostructures by scanning Kelvin probe microscopy. *Journal of Applied Physics*, 90(1):337–344, 2001.
- [77] W. T. Read. Theory of dislocations in germanium. *Philosophical Magazine*, 45:775–796, 1954.
- [78] A. Krtischil, A. Dadgar, and A. Krost. Decoration effects as origin of dislocation-related charges in gallium nitride layers investigated by scanning surface potential microscopy. *Applied Physics Letters*, 82(14):2263–2265, 2003.
- [79] C. Shi, P. M. Asbeck, and E. T. Yu. Piezoelectric polarization associated with dislocations in wurtzite GaN. *Applied Physics Letters*, 74(4):573–575, 1999.
- [80] J. P. Hirth and J. Lothe. *Theory of Dislocations*. John Wiley & Sons, New York, 2nd edition, 1982.
- [81] D. J. Griffiths. *Introduction to Electrodynamics*. Prentice Hall, Upper Saddle River, NJ, 3rd edition, 1999.

- [82] G. F. Bai, V. F. Petrenko, and I. Baker. Study of electrical properties of dislocations in ZnS using electric force microscopy. *Materials Research Society Symposium Proceedings*, 578:255–260, 2000.
- [83] G. F. Bai, V. F. Petrenko, and I. Baker. On the electrical properties of dislocations in ZnS using electric force microscopy. *Scanning*, 23:160–164, 2001.
- [84] V. F. Petrenko and R. W. Whitworth. Charged dislocations and the plastic deformation of II-VI compounds. *Philosophical Magazine A*, 41(5):681–699, 1980.
- [85] L. Kronik and Y. Shapira. Surface photovoltage phenomena: theory, experiment, and applications. *Surface Science Reports*, 37:1–206, 1999.
- [86] C.L. Balestra, J. Lagowski, and H.C. Gatos. Determination of surface state parameters from surface photovoltage transients. *Surface Science*, 64:457–464, 1977.
- [87] J. Lagowski, C. L. Balestra, and H. C. Gatos. Determination of surface state parameters from surface photovoltage transients: CdS. *Surface Science*, 29:203–212, 1972.
- [88] Technical report, Eagle-Picher Technologies, 2000.
- [89] C. Tromas, J. Colin, C. Coupeau, J. C. Girard, J. Woirgard, and J. Grilhe. Pop-in phenomenon during nanoindentation in MgO. *The European Physical Journal*, 8:123–128, 1999.
- [90] K. L. Johnson. *Contact Mechanics*. Cambridge University Press, Cambridge, 1985.
- [91] M. Göken and M. Kempf. Pop-ins in nanoindentation – the initial yield point. *Zeitschrift für Metallkunde*, 92:1061–1067, 2001.
- [92] M. H. Zhao, Z. L. Wang, and S. X. Mao. Piezoelectric characteristics of individual zinc oxide nanobelt probed by piezoresponse force microscope. *Nano Letters*, 4(4):587–590, 2004.
- [93] K. Maeda, O. Ueda, Y. Murayama, and K. Sakamoto. Mechanical properties and photomechanical effect in GaP single crystals. *Journal of Physics and Chemistry of Solids*, 38:1173–1179, 1977.
- [94] P. B. Hirsch, P. Pirouz, S. G. Roberts, and P. D. Warren. Indentation plasticity and polarity of hardness on {111} faces of GaAs. *Philosophical Magazine B*, 52(3):759–784, 1985.
- [95] S. G. Roberts. Hardness anisotropy and polarity in indium antimonide. *Philosophical Magazine A*, 54(1):37–45, 1986.

- [96] W. W. Gerberich, J. C. Nelson, E. T. Lilleodden, P. Anderson, and J. T. Wyrobek. Indentation induced dislocation nucleation: The initial yield point. *Acta Materialia*, 44:3585–3598, 1996.
- [97] D. Lorenz, A. Zeckzer, U. Hilpert, P. Grau, H. Johansen, and H. S. Leipner. Pop-in as homogeneous nucleation of dislocations during nanoindentation. *Physical Review B*, 67:172101–1 – 172101–4, 2003.
- [98] J. Li, K. J. Van Vliet, T. Zhu, S. Yip, and S. Suresh. Atomistic mechanisms governing elastic limit and incipient plasticity in crystals. *Nature*, 418:307–310, 2002.
- [99] J. Li, T. Zhu, S. Yip, K. J. Van Vliet, and S. Suresh. Elastic criterion for dislocation nucleation. *Materials Science and Engineering A*, 365:25–30, 2004.
- [100] R. E. Miller and A. Acharya. A stress-gradient based criterion for dislocation nucleation in crystals. *Journal of the Mechanics and Physics of Solids*, 52:1507–1525, 2004.
- [101] Y. Gaillard, C. Tromas, and J. Woignard. Study of the dislocation structure involved in a nanoindentation test by atomic force microscopy and controlled chemical etching. *Acta Materialia*, 51:1059–1065, 2003.
- [102] J. S. Ahearn, J. J. Mills, A. R. C. Westwood, and D. A. Kalivoda. Influence of surface charge on the hardness of ZnO. In N. P. Suh and N. Saka, editors, *Fundamentals of Tribology*, pages 295–316, Massachusetts Institute of Technology, Cambridge, Massachusetts, 1978. MIT Press.
- [103] B. S. Simpkins, D. M. Schaadt, and E. T. Yu. Scanning Kelvin probe microscopy of surface electronic structure in GaN grown by hydride vapor phase epitaxy. *Journal of Applied Physics*, 91(12):9924–9929, 2002.
- [104] G. Koley and M. G. Spencer. Scanning Kelvin probe microscopy characterization of dislocations in III-Nitrides grown by metalorganic chemical vapor deposition. *Applied Physics Letters*, 78(19):2873–2875, 2001.
- [105] M. J. Klopstein, D. A. Lucca, and G. Cantwell. Effects of illumination on the response of (0001)ZnO to nanoindentation. *physica status solidi (a)*, 196(1):R1–R3, 2003.
- [106] Yu. A. Osip’yan and V. F. Petrenko. Investigation of the mechanism of the motion of charged dislocations in ZnSe. *Soviet Physics JETP*, 48(1):147–152, 1978.

- [107] D. Kramer, H. Huang, M. Kriese, J. Robach, J. Nelson, A. Wright, D. Bahr, and W. W. Gerberich. Yield strength predictions from the plastic zone around nanocontacts. *Acta Materialia*, 47:333–343, 1999.
- [108] L. Carlsson. Orientation and temperature dependence of the photoplastic effect in ZnO. *Journal of Applied Physics*, 42:676–680, 1971.
- [109] H. Moormann, D. Kohl, and G. Heiland. Work function and band bending on clean cleaved zinc oxide surfaces. *Surface Science*, 80:261–264, 1979.
- [110] J. W. Harding and I. N. Sneddon. The elastic stresses produced by the indentation of the plane surface of a semi-infinite elastic solid by a rigid punch. *Proceedings of the Cambridge Philosophical Society*, 41:16–26, 1945.
- [111] A. E. Giannakopoulos. Strength analysis of spherical indentation of piezoelectric materials. *Journal of Applied Mechanics*, 67:409–416, 2000.

Appendix A

Determination of Area Function and Instrument Compliance for Nanoindentation

Both the area function of the indenter and the compliance of the nanoindentation instrument are determined by using the method of Oliver and Pharr [35]. Parts of the ISO 14577 (Metallic materials – Instrumented indentation test for hardness and materials parameters) are based on this technique.

Oliver and Pharr developed a technique for determining both the area function of the indenter and the compliance of the nanoindentation instrument by indentations in reference materials whose elastic modulus is assumed to be known. The two reference materials used are fused silica and single crystal aluminum. The sample and the nanoindentation instrument are modeled as two linear springs in series, so the total measured compliance is given by:

$$C_{\text{total}} = C_f + C_s \quad (\text{A.1})$$

where C_{total} is the total measured compliance i.e., $1/S$, C_f is the compliance of the load frame of the nanoindentation instrument, and C_s is the compliance of the sample. The compliance of the sample is related to the elastic modulus and the projected area of contact (A) by:

$$C_s = \frac{\sqrt{\pi}}{2E_r} \frac{1}{\sqrt{A}} \quad (\text{A.2})$$

where E_r is the “reduced” modulus and is given by $\frac{1}{E_r} = \frac{1-\nu^2}{E} + \frac{1-\nu_i^2}{E_i}$ where ν and E are Poisson’s ratio and elastic modulus for the sample and ν_i and E_i are the same for the indenter. Substituting

the value of the sample compliance, Eq. A.2 into Eq. A.1 gives:

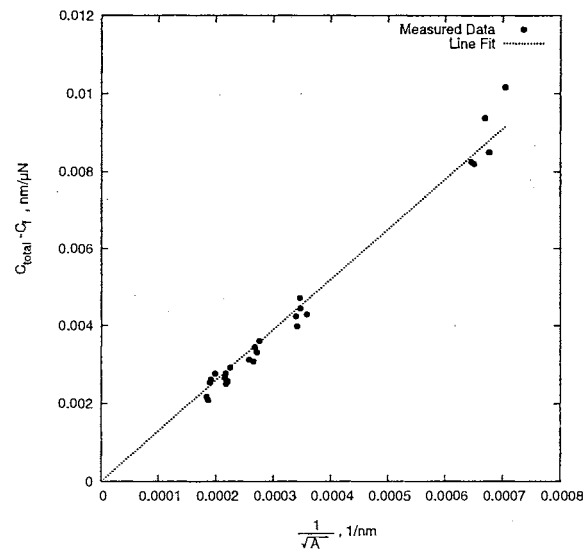
$$C_{\text{total}} = C_f + \frac{\sqrt{\pi}}{2E_r} \frac{1}{\sqrt{A}} \quad (\text{A.3})$$

From Eq. A.3 we see that a plot of the total measured compliance vs. $1/\sqrt{A}$ should be linear with an intercept equal to the frame compliance. In order to get a good estimate of the frame compliance deep indents should be made so that the second term on the right side of Eq. A.3 is small. In order to obtain the area function and frame compliance an iterative procedure is used on a data collected for a range of deep indentations.

1. Assume $A(h_c) = 24.5h_c^2$
2. From a plot of C_{total} vs. $A^{-1/2}$ obtain an estimate of C_f
3. Calculate contact area from $A = \frac{\pi}{4} \frac{1}{E_r^2(C_{\text{total}} - C_f)}$
4. Fit a curve to the equation $A(h_c) = 24.5h_c^2 + C_1h_c + C_2h_c^{1/2} + C_3h_c^{1/4}$
5. Goto step 2 and repeat until the area function and frame compliance converge

For the deeper indentations this procedure yields a good estimate for the frame compliance but the area function obtained should not be extended to shallow indentations. Instead shallower indentations are made in fused silica to determine the area function in this range. The iteration converges more quickly since the frame compliance is known from the indentations in aluminum.

A series of indentations at depths from about 200-900 nm was made in electropolished (100)Al. This data was then used to calculate the frame compliance of the instrument using software by Hysitron Inc. Figure A.1 shows the total measured compliance minus the frame compliance (0.002 nm/ μ N) vs. one on the square root of the area. Plotted in this way the line should go through the origin which it does. The value of the frame compliance is comparable to that of another commercial nanoindenter [35], 0.001 nm/ μ N. The slope of the best fit line is 13 nm²/ μ N which gives a reduced elastic modulus of 68 GPa. This is about 8% smaller than the literature value for aluminum [35].



Appendix B

Indentation of a Transversely Isotropic Piezoelectric Halfspace

B.1 Development of equations

The development of the piezoelectric equations for a transversely isotropic halfspace, $z > 0$, is based on the papers by B.A. Kudriavtsev, V.Z. Parton and V.I. Rakitin (referred to as KPR paper) [49], A.E. Giannakopoulos and S. Suresh [52] and S. Matysiak [51]. The exposition below will closely follow the KPR paper and differences from this paper will be noted.

Starting with Eq. 2.1 in the KPR paper (no change)

$$\begin{aligned}\frac{\partial \sigma_{rr}}{\partial r} + \frac{\partial \sigma_{rz}}{\partial z} + \frac{\sigma_{rr} - \sigma_{\theta\theta}}{r} &= 0 \\ \frac{\partial \sigma_{rz}}{\partial r} + \frac{\partial \sigma_{zz}}{\partial z} + \frac{\sigma_{rz}}{r} &= 0 \\ \frac{\partial D_r}{\partial r} + \frac{1}{r} D_r + \frac{\partial D_z}{\partial z} &= 0\end{aligned}\tag{2.1 in KPR paper}$$

and also Eq. 2.2 (no change)

$$\begin{aligned}\sigma_i &= c_{ij}\varepsilon_j - e_{ik}E_k \\ D_k &= e_{ik}\varepsilon_i + \epsilon_{kl}E_k\end{aligned}\tag{2.2 in KPR paper}$$

The electric field is related to the potential by the following:

$$E_r = -\frac{\partial\phi}{\partial r}$$

$$E_z = -\frac{\partial\phi}{\partial z}$$

The KPR paper omits the minus sign in the above equation. This mistake then propagates through the rest of the paper. Eq. 2.3 should become:

$$\begin{aligned}\sigma_{rr} &= c_{11} \frac{\partial u_r}{\partial r} + c_{12} \frac{u_r}{r} + c_{13} \frac{\partial u_z}{\partial z} + e_{31} \frac{\partial\phi}{\partial z} \\ \sigma_{\theta\theta} &= c_{12} \frac{\partial u_r}{\partial r} + c_{11} \frac{u_r}{r} + c_{13} \frac{\partial u_z}{\partial z} + e_{31} \frac{\partial\phi}{\partial z} \\ \sigma_{zz} &= c_{13} \left(\frac{\partial u_r}{\partial r} + \frac{u_r}{r} \right) + c_{33} \frac{\partial u_z}{\partial z} + e_{33} \frac{\partial\phi}{\partial z} \\ \sigma_{rz} &= c_{44} \left(\frac{\partial u_r}{\partial z} + \frac{\partial u_z}{\partial r} \right) + e_{15} \frac{\partial\phi}{\partial r} \\ D_r &= e_{15} \left(\frac{\partial u_r}{\partial z} + \frac{\partial u_z}{\partial r} \right) - \epsilon_{11} \frac{\partial\phi}{\partial r} \\ D_z &= e_{31} \left(\frac{\partial u_r}{\partial r} + \frac{u_r}{r} \right) + e_{33} \frac{\partial u_z}{\partial z} - \epsilon_{33} \frac{\partial\phi}{\partial z}\end{aligned}\tag{2.3 in KPR paper, corrected}$$

In addition to the sign error there is also a typographical error in Eq. 2.4.

$$\begin{aligned}c_{11} \left(\frac{\partial^2 u_r}{\partial r^2} + \frac{1}{r} \frac{\partial u_r}{\partial r} - \frac{u_r}{r^2} \right) + c_{44} \frac{\partial^2 u_r}{\partial z^2} + (c_{44} + c_{13}) \frac{\partial^2 u_z}{\partial r \partial z} \\ + (e_{31} + e_{15}) \frac{\partial^2 \phi}{\partial r \partial z} &= 0 \\ c_{44} \left(\frac{\partial^2 u_z}{\partial r^2} + \frac{1}{r} \frac{\partial u_z}{\partial r} \right) + c_{33} \frac{\partial^2 u_z}{\partial z^2} + (c_{44} + c_{13}) \frac{\partial}{\partial z} \left(\frac{\partial u_r}{\partial r} + \frac{u_r}{r} \right) \\ + e_{15} \left(\frac{\partial^2 \phi}{\partial r^2} + \frac{1}{r} \frac{\partial \phi}{\partial r} \right) + e_{33} \frac{\partial^2 \phi}{\partial z^2} &= 0 \\ e_{15} \left(\frac{\partial^2 u_z}{\partial r^2} + \frac{1}{r} \frac{\partial u_z}{\partial r} \right) + e_{33} \frac{\partial^2 u_z}{\partial z^2} + (e_{15} + e_{31}) \frac{\partial}{\partial z} \left(\frac{\partial u_r}{\partial r} + \frac{u_r}{r} \right) \\ - \epsilon_{11} \left(\frac{\partial^2 \phi}{\partial r^2} + \frac{1}{r} \frac{\partial \phi}{\partial r} \right) - \epsilon_{33} \frac{\partial^2 \phi}{\partial z^2} &= 0\end{aligned}\tag{B.1}$$

Because of the way that the dual integral equations will be solved below, it is convenient to introduce non-dimensional lengths, ζ , and ρ where,

$$\rho \equiv r/a \quad \zeta \equiv z/a$$

Using the above definitions Eqs. B.1 become,

$$\begin{aligned}
& c_{11} \left(\frac{\partial^2 u_r}{\partial \rho^2} + \frac{1}{\rho} \frac{\partial u_r}{\partial \rho} - \frac{u_r}{\rho^2} \right) + c_{44} \frac{\partial^2 u_r}{\partial \zeta^2} + (c_{44} + c_{13}) \frac{\partial^2 u_z}{\partial \rho \partial \zeta} \\
& \quad + (e_{31} + e_{15}) \frac{\partial^2 \phi}{\partial \rho \partial \zeta} = 0 \\
& c_{44} \left(\frac{\partial^2 u_z}{\partial \rho^2} + \frac{1}{\rho} \frac{\partial u_z}{\partial \rho} \right) + c_{33} \frac{\partial^2 u_z}{\partial \zeta^2} + (c_{44} + c_{13}) \frac{\partial}{\partial \zeta} \left(\frac{\partial u_r}{\partial \rho} + \frac{u_r}{\rho} \right) \\
& \quad + e_{15} \left(\frac{\partial^2 \phi}{\partial \rho^2} + \frac{1}{\rho} \frac{\partial \phi}{\partial \rho} \right) + e_{33} \frac{\partial^2 \phi}{\partial \zeta^2} = 0 \quad (\text{B.2}) \\
& e_{15} \left(\frac{\partial^2 u_z}{\partial \rho^2} + \frac{1}{\rho} \frac{\partial u_z}{\partial \rho} \right) + e_{33} \frac{\partial^2 u_z}{\partial \zeta^2} + (e_{15} + e_{31}) \frac{\partial}{\partial \zeta} \left(\frac{\partial u_r}{\partial \rho} + \frac{u_r}{\rho} \right) \\
& \quad - \epsilon_{11} \left(\frac{\partial^2 \phi}{\partial \rho^2} + \frac{1}{\rho} \frac{\partial \phi}{\partial \rho} \right) - \epsilon_{33} \frac{\partial^2 \phi}{\partial \zeta^2} = 0
\end{aligned}$$

Use the Hankel transforms of Eq. 3.1 (note that the transform of u_r involves J_1 and the other two use J_0).

$$\begin{aligned}
u_r(\rho, \zeta) &= \int_0^\infty U(\zeta, \xi) J_1(\xi \rho) d\xi \\
u_z(\rho, \zeta) &= \int_0^\infty V(\zeta, \xi) J_0(\xi \rho) d\xi \\
\phi(\rho, \zeta) &= \int_0^\infty \Phi(\zeta, \xi) J_0(\xi \rho) d\xi
\end{aligned} \quad (3.1 \text{ in KPR paper})$$

Plugging these into Eq. B.2 the following is obtained:

$$\begin{aligned}
& \int_0^\infty \left[-c_{11} \xi^2 U - (c_{13} + c_{44}) \xi \frac{\partial V}{\partial \zeta} - (e_{31} + e_{15}) \xi \frac{\partial \Phi}{\partial \zeta} + c_{44} \frac{\partial^2 U}{\partial \zeta^2} \right] J_1(\xi \rho) d\xi = 0 \\
& \int_0^\infty \left[-c_{44} \xi^2 V + c_{33} \frac{\partial^2 V}{\partial \zeta^2} + (c_{13} + c_{44}) \xi \frac{\partial U}{\partial \zeta} - e_{15} \xi^2 \Phi + e_{33} \frac{\partial^2 \Phi}{\partial \zeta^2} \right] J_0(\xi \rho) d\xi = 0 \\
& \int_0^\infty \left[-e_{15} \xi^2 V + e_{33} \frac{\partial^2 V}{\partial \zeta^2} + (e_{15} + e_{31}) \xi \frac{\partial U}{\partial \zeta} + \epsilon_{11} \xi^2 \Phi - \epsilon_{33} \frac{\partial^2 \Phi}{\partial \zeta^2} \right] J_0(\xi \rho) d\xi = 0
\end{aligned}$$

Let us introduce notation for the integrals,

$$I_n = \int_0^\infty J_n(\xi \rho) d\xi$$

The above integrals become:

$$\begin{aligned}
\left[c_{44} \frac{\partial^2 U}{\partial \zeta^2} - c_{11} \xi^2 U - (c_{13} + c_{44}) \xi \frac{\partial V}{\partial \zeta} - (e_{31} + e_{15}) \xi \frac{\partial \Phi}{\partial \zeta} \right] I_1 &= 0 \\
\left[(c_{13} + c_{44}) \xi \frac{\partial U}{\partial \zeta} - c_{44} \xi^2 V + c_{33} \frac{\partial^2 V}{\partial \zeta^2} - e_{15} \xi^2 \Phi + e_{33} \frac{\partial^2 \Phi}{\partial \zeta^2} \right] I_0 &= 0 \\
\left[(e_{15} + e_{31}) \xi \frac{\partial U}{\partial \zeta} - e_{15} \xi^2 V + e_{33} \frac{\partial^2 V}{\partial \zeta^2} + \epsilon_{11} \xi^2 \Phi - \epsilon_{33} \frac{\partial^2 \Phi}{\partial \zeta^2} \right] I_0 &= 0
\end{aligned} \tag{B.3}$$

The particular solution may be written as:

$$\begin{aligned}
U &= \alpha e^{-k\xi\zeta} \\
V &= \beta e^{-k\xi\zeta} \\
\Phi &= \gamma e^{-k\xi\zeta}
\end{aligned} \tag{B.4}$$

Substituting Eqs. B.4 into Eqs. B.3 and dropping the I terms,

$$\begin{aligned}
[c_{44} k^2 \xi^2 \alpha - c_{11} \xi^2 \alpha + (c_{13} + c_{44}) k \xi^2 \beta + (e_{31} + e_{15}) k \xi^2 \gamma] e^{-k\xi\zeta} &= 0 \\
[-(c_{13} + c_{44}) k \xi^2 \alpha - c_{44} \xi^2 \beta + c_{33} k^2 \xi^2 \beta - e_{15} \xi^2 \gamma + e_{33} k^2 \xi^2 \gamma] e^{-k\xi\zeta} &= 0 \\
[-(e_{15} + e_{31}) k \xi^2 \alpha - e_{15} \xi^2 \beta + e_{33} k^2 \xi^2 \beta + \epsilon_{11} \xi^2 \gamma - \epsilon_{33} k^2 \xi^2 \gamma] e^{-k\xi\zeta} &= 0
\end{aligned} \tag{B.5}$$

Since $\xi \neq 0$ and the exponential term is not equal to zero Eqs. B.5 can be written as:

$$\begin{bmatrix} c_{44} k^2 - c_{11} & (c_{13} + c_{44}) k & (e_{31} + e_{15}) k \\ -(c_{13} + c_{44}) k & c_{33} k^2 - c_{44} & e_{33} k^2 - e_{15} \\ -(e_{31} + e_{15}) k & e_{33} k^2 - e_{15} & -\epsilon_{33} k^2 + \epsilon_{11} \end{bmatrix} \begin{bmatrix} \alpha \\ \beta \\ \gamma \end{bmatrix} = \begin{bmatrix} 0 \\ 0 \\ 0 \end{bmatrix}$$

This is the matrix a_{ij} in the KPR paper (Eq. 3.2) but some of the values of a_{ij} have a different sign. For ZnO setting the determinant equal to zero gives two real roots $\pm k_1$ and four complex roots $\pm \delta \pm i\omega$. The constants α , β and γ can be obtained from:

$$\begin{aligned}
\alpha &= a_{12} a_{23} - a_{13} a_{22} \\
\beta &= -a_{11} a_{23} - a_{12} a_{13} \\
\gamma &= a_{11} a_{22} + a_{12}^2
\end{aligned}$$

where the a 's are obtained by using either k_1 , or $\delta + i\omega$. This results in: $\alpha_1 = \alpha(k_1)$, $\beta_1 = \beta(k_1)$, $\gamma_1 = \gamma(k_1)$, $\alpha_{21} + \alpha_{22} = \alpha(\delta + i\omega)$, $\beta_{21} + \beta_{22} = \beta(\delta + i\omega)$, $\gamma_{21} + \gamma_{22} = \gamma(\delta + i\omega)$. The three functions U, V, Φ are given by:

$$\begin{bmatrix} U \\ V \\ \Phi \end{bmatrix} = \begin{bmatrix} \alpha_1 \\ \beta_1 \\ \gamma_1 \end{bmatrix} A_1(\xi) e^{-k_1 \xi \zeta} + \text{Re} \left\{ \begin{bmatrix} \alpha_{21} + i\alpha_{22} \\ \beta_{21} + i\beta_{22} \\ \gamma_{21} + i\gamma_{22} \end{bmatrix} [B_1(\xi) + iC_1(\xi)] e^{-\xi \zeta (\delta + i\omega)} \right\}$$

$$\begin{aligned} u_r(\rho, \zeta) &= \int_0^\infty [\alpha_1 A_1(\xi) e^{-k_1 \xi \zeta} + (\alpha_{21} B_1(\xi) - \alpha_{22} C_1(\xi)) e^{-\delta \xi \zeta} \cos(\omega \xi \zeta) \\ &\quad + (\alpha_{22} B_1(\xi) + \alpha_{21} C_1(\xi)) e^{-\delta \xi \zeta} \sin(\omega \xi \zeta)] J_1(\xi \rho) d\xi \\ u_z(\rho, \zeta) &= \int_0^\infty [\beta_1 A_1(\xi) e^{-k_1 \xi \zeta} + (\beta_{21} B_1(\xi) - \beta_{22} C_1(\xi)) e^{-\delta \xi \zeta} \cos(\omega \xi \zeta) \\ &\quad + (\beta_{22} B_1(\xi) + \beta_{21} C_1(\xi)) e^{-\delta \xi \zeta} \sin(\omega \xi \zeta)] J_0(\xi \rho) d\xi \\ \phi(\rho, \zeta) &= \int_0^\infty [\gamma_1 A_1(\xi) e^{-k_1 \xi \zeta} + (\gamma_{21} B_1(\xi) - \gamma_{22} C_1(\xi)) e^{-\delta \xi \zeta} \cos(\omega \xi \zeta) \\ &\quad + (\gamma_{22} B_1(\xi) + \gamma_{21} C_1(\xi)) e^{-\delta \xi \zeta} \sin(\omega \xi \zeta)] J_0(\xi \rho) d\xi \end{aligned}$$

On the surface $\zeta = 0$ the displacements and stresses are given by:

$$\begin{aligned} u_r(\rho, \zeta = 0) &= \int_0^\infty [\alpha_1 A_1(\xi) + \alpha_{21} B_1(\xi) - \alpha_{22} C_1(\xi)] J_1(\xi \rho) d\xi \\ u_z(\rho, \zeta = 0) &= \int_0^\infty [\beta_1 A_1(\xi) + \beta_{21} B_1(\xi) - \beta_{22} C_1(\xi)] J_0(\xi \rho) d\xi \\ \phi(\rho, \zeta = 0) &= \int_0^\infty [\gamma_1 A_1(\xi) + \gamma_{21} B_1(\xi) - \gamma_{22} C_1(\xi)] J_0(\xi \rho) d\xi \\ \sigma_{zr}(\rho, \zeta = 0) &= \int_0^\infty [m_1 A_1(\xi) + m_2 B_1(\xi) - m_3 C_1(\xi)] \xi J_1(\xi \rho) d\xi \\ \sigma_{zz}(\rho, \zeta = 0) &= \int_0^\infty [n_1 A_1(\xi) + n_2 B_1(\xi) + n_3 C_1(\xi)] \xi J_0(\xi \rho) d\xi \end{aligned} \tag{B.6}$$

where

$$\begin{aligned}
m_1 &= -e_{15}\gamma_1 - c_{44}(\beta_1 + k_1\alpha_1) \\
m_2 &= -e_{15}\gamma_{21} - c_{44}(\beta_{21} - \alpha_{22}\omega + \alpha_{21}\delta) \\
m_3 &= -e_{15}\gamma_{22} - c_{44}(\beta_{22} + \alpha_{21}\omega + \alpha_{22}\delta) \\
n_1 &= c_{13}\alpha_1 - c_{33}k_1\beta_1 - e_{33}k_1\gamma_1 \\
n_2 &= c_{13}\alpha_{21} - c_{33}(\beta_{21}\delta - \beta_{22}\omega) - e_{33}(\gamma_{21}\delta - \gamma_{22}\omega) \\
n_3 &= -c_{13}\alpha_{22} + c_{33}(\beta_{22}\delta + \beta_{21}\omega) + e_{33}(\gamma_{22}\delta + \gamma_{21}\omega)
\end{aligned}$$

Using the condition that the surface of the half-space does not have a shear stress the equation for σ_{zr} gives the relationship $C_1 = \frac{m_1}{m_3}A_1 + \frac{m_2}{m_3}B_1$ thus the dual integral equations are:

$$\begin{aligned}
u_z(\rho, \zeta = 0) &= \int_0^\infty \left[\left(\beta_1 + \frac{m_1}{m_3}\beta_{22} \right) A_1(\xi) + \left(\beta_{21} + \frac{m_2}{m_3}\beta_{22} \right) B_1(\xi) \right] J_0(\xi\rho) d\xi \\
&= f(\rho) + b \quad 0 \leq \rho \leq 1 \\
\phi(\rho, \zeta = 0) &= \int_0^\infty \left[\left(\gamma_1 + \frac{m_1}{m_3}\gamma_{22} \right) A_1(\xi) + \left(\gamma_{21} + \frac{m_2}{m_3}\gamma_{22} \right) B_1(\xi) \right] J_0(\xi\rho) d\xi \\
&= \phi_0 \quad 0 \leq \rho < 1 \\
\sigma_{zz}(\rho, \zeta = 0) &= \int_0^\infty \left[\left(n_1 + \frac{m_1}{m_3}n_3 \right) A_1(\xi) + \left(n_2 + \frac{m_2}{m_3}n_3 \right) B_1(\xi) \right] \xi J_0(\xi\rho) d\xi \\
&= 0 \quad \rho > 1 \\
D_z(\rho, \zeta = 0) &= \int_0^\infty \left[\left(l_1 + \frac{m_1}{m_3}l_3 \right) A_1(\xi) + \left(l_2 + \frac{m_2}{m_3}l_3 \right) B_1(\xi) \right] \xi J_0(\xi\rho) d\xi \\
&= 0 \quad \rho > 1
\end{aligned} \tag{B.7}$$

where

$$\begin{aligned}
l_1 &= e_{31}\alpha_1 - e_{33}k_1\beta_1 + e_{33}k_1\gamma_1 \\
l_2 &= e_{31}\alpha_{21} - e_{33}\beta_{21}\delta + e_{33}\beta_{22}\omega + e_{33}\gamma_{21}\delta - e_{33}\gamma_{22}\omega \\
l_3 &= -e_{31}\alpha_{22} + e_{33}\beta_{21}\omega + e_{33}\beta_{22}\delta - e_{33}\gamma_{21}\omega - e_{33}\gamma_{22}\delta
\end{aligned}$$

The solution of the dual integral equations (Eqs. B.7) proceeds as outlined in Matysiak's paper [51] for the case of a conducting indenter. A paper by Harding and Sneddon [110] is also helpful

and will be used. The case of the insulating indenter will be shown further below. First it is more convenient to rename $B_1(\xi)$, $A_2(\xi)$ and to define constants for the coefficients so Eqs. B.7 become

$$\begin{aligned}
u_z(\rho, \zeta = 0) &= \int_0^\infty [M_1 A_1(\xi) + M_2 A_2(\xi)] J_0(\xi \rho) d\xi = f(\rho) + b \quad 0 \leq \rho \leq 1 \\
\phi(\rho, \zeta = 0) &= \int_0^\infty [M_3 A_1(\xi) + M_4 A_2(\xi)] J_0(\xi \rho) d\xi = \phi_0 \quad 0 \leq \rho < 1 \\
\sigma_{zz}(\rho, \zeta = 0) &= \int_0^\infty [M_5 A_1(\xi) + M_6 A_2(\xi)] \xi J_0(\xi \rho) d\xi = 0 \quad \rho > 1 \\
D_z(\rho, \zeta = 0) &= \int_0^\infty [M_7 A_1(\xi) + M_8 A_2(\xi)] \xi J_0(\xi \rho) d\xi = 0 \quad \rho > 1
\end{aligned} \tag{B.8}$$

where

$$\begin{aligned}
M_1 &= \left(\beta_1 - \frac{m_1}{m_3} \beta_{22} \right) & M_2 &= \left(\beta_{21} - \frac{m_2}{m_3} \beta_{22} \right) \\
M_3 &= \left(\gamma_1 - \frac{m_1}{m_3} \gamma_{22} \right) & M_4 &= \left(\gamma_{21} - \frac{m_2}{m_3} \gamma_{22} \right) \\
M_5 &= \left(n_1 + \frac{m_1}{m_3} n_3 \right) & M_6 &= \left(n_2 + \frac{m_2}{m_3} n_3 \right) \\
M_7 &= \left(l_1 + \frac{m_1}{m_3} l_3 \right) & M_8 &= \left(l_2 + \frac{m_2}{m_3} l_3 \right)
\end{aligned}$$

Using Crammer's rule Eqs. B.8 can be written compactly as:

$$\begin{aligned}
\int_0^\infty A_\alpha(\xi) J_0(\xi \rho) d\xi &= F_\alpha(\rho) \quad 0 \leq \rho < 1 \\
\int_0^\infty \xi A_\alpha(\xi) J_0(\xi \rho) d\xi &= 0 \quad \rho > 1 \quad \alpha = 1, 2
\end{aligned} \tag{B.9}$$

where

$$\begin{aligned}
F_1(\rho) &= \frac{M_4 f(\rho) - M_2 \phi_0 + M_4 b}{M_1 M_4 - M_2 M_3} \\
F_2(\rho) &= \frac{-M_3 f(\rho) + M_1 \phi_0 - M_3 b}{M_1 M_4 - M_2 M_3}
\end{aligned} \tag{B.10}$$

The solution to Eqs. B.9 is well known. If the function $F_\alpha(\rho) = \sum_n Z_n \rho^n$ then solution for the A_α 's is given by:

$$A_\alpha(\xi) = \frac{1}{\sqrt{\pi}} \sum_n \frac{\Gamma(\frac{1}{2}n + 1)}{\Gamma(\frac{1}{2}n + \frac{3}{2})} Z_n \left\{ \cos \xi + \xi \int_0^1 u^{n+1} \sin(\xi u) du \right\} \quad \alpha = 1, 2$$

Consider an axisymmetric punch profile given by $f(\rho) = c_0 + c_1 \rho + c_2 \rho^2$ where c_0, c_1, c_2 are constants. Thus $F_\alpha(\rho) = K_0 + K_1 \rho + K_2 \rho^2$, each term will be considered in series.

For $F_\alpha = K_0$,

$$A_\alpha(\xi) = \frac{2K_0}{\pi} \left(\frac{\sin(\xi)}{\xi} \right) \tag{B.11}$$

For $F_\alpha = K_1 \rho$,

$$A_\alpha(\xi) = K_1 \left[\frac{\sin(\xi)}{\xi} + \frac{1}{\xi^2} (\cos(\xi) - 1) \right] \tag{B.12}$$

For $F_\alpha = K_2 \rho^2$,

$$A_\alpha(\xi) = \frac{8K_2}{3\pi} \left[\left(\frac{1}{\xi} - \frac{2}{\xi^3} \right) \sin(\xi) + \frac{2}{\xi^2} \cos(\xi) \right] \quad (\text{B.13})$$

B.1.1 Indentation with a conducting conical indenter

Let us consider the special case of a conical punch given by $f(\rho) = \epsilon(1 - \rho)$ then F_1 is given by

$$F_1(\rho) = \frac{M_4\epsilon - M_2\phi_0 + M_4b}{M_1M_4 - M_2M_3} + \frac{-M_4\epsilon\rho}{M_1M_4 - M_2M_3}$$

From which K_0 and K_1 can be identified,

$$K_0 = \frac{M_4\epsilon - M_2\phi_0 + M_4b}{M_1M_4 - M_2M_3} \quad K_1 = \frac{-M_4\epsilon}{M_1M_4 - M_2M_3}$$

The function A_1 can be computed from Eqs. B.11 and B.12,

$$A_1(\xi) = \left(\frac{2K_0}{\pi} + K_1 \right) \frac{\sin(\xi)}{\xi} + \frac{K_1}{\xi^2} (\cos(\xi) - 1)$$

In a similar way the function A_2 can be computed

$$\begin{aligned} \bar{K}_0 &= \frac{-M_3\epsilon + M_1\phi_0 - M_3b}{M_1M_4 - M_2M_3} & \bar{K}_1 &= \frac{M_3\epsilon}{M_1M_4 - M_2M_3} \\ A_2(\xi) &= \left(\frac{2\bar{K}_0}{\pi} + \bar{K}_1 \right) \frac{\sin(\xi)}{\xi} + \frac{\bar{K}_1}{\xi^2} (\cos(\xi) - 1) \end{aligned}$$

Consider the stress component σ_{zz} at the circle $\rho = 1$.

$$\begin{aligned} \sigma_{zz}(\rho = 1, \zeta = 0) &= \int_0^\infty [M_5 A_1(\xi) + M_6 A_2(\xi)] \xi J_0(\xi) d\xi \\ \sigma_{zz}(\rho = 1, \zeta = 0) &= \int_0^\infty \left(\frac{2}{\pi} K_0 M_5 + K_1 M_5 + \frac{2}{\pi} \bar{K}_0 M_6 + \bar{K}_1 M_6 \right) \sin(\xi) J_0(\xi) \\ &\quad + (K_1 M_5 + \bar{K}_1 M_6) \frac{\cos(\xi) - 1}{\xi} J_0(\xi) d\xi \end{aligned} \quad (\text{B.14})$$

The first term of the integral in Eq. B.14 diverges but the stress at $\rho = 1$ is finite so the term in parenthesis must be zero. This results in an expression for b ,

$$b = \epsilon \left(\frac{\pi}{2} - 1 \right) - \frac{M_1 M_6 - M_2 M_5}{M_4 M_5 - M_3 M_6} \phi_0$$

Returning to the stress component σ_{zz} ,

$$\begin{aligned} \sigma_{zz}(\rho, \zeta = 0) &= \int_0^\infty (K_1 M_5 + \bar{K}_1 M_6) \frac{\cos(\xi) - 1}{\xi} J_0(\xi \rho) d\xi \\ \sigma_{zz}(\rho, \zeta = 0) &= - (K_1 M_5 + \bar{K}_1 M_6) \cosh^{-1} \left(\frac{1}{\rho} \right) \end{aligned}$$

The force on the indenter is just the summation of the stress over the circular contact region on the surface of the solid.

$$\begin{aligned}
P &= -2\pi a^2 \int_0^1 \rho \sigma_{zz}(\rho, \zeta = 0) d\rho \\
P &= 2\pi a^2 \int_0^1 \rho (K_1 M_5 + \overline{K}_1 M_6) \cosh^{-1} \left(\frac{1}{\rho} \right) d\rho \\
P &= \pi a^2 (K_1 M_5 + \overline{K}_1 M_6) \\
P_{\text{conductor}} &= \pi a^2 \epsilon \frac{M_3 M_6 - M_4 M_5}{M_1 M_4 - M_2 M_3}
\end{aligned}$$

The above result agrees with Giannakopoulos and Suresh [52] up to a minus sign but this difference is just because of the sign convention used. The vector P is in the positive z direction i.e., into the solid.

B.1.2 Indentation with an insulating conical indenter

Things are a little easier when the indenter is an insulator. The dual integral equations are:

$$\begin{aligned}
u_z(\rho, \zeta = 0) &= \int_0^\infty [M_1 A_1(\xi) + M_2 A_2(\xi)] J_0(\xi \rho) d\xi = f(\rho) + b \quad 0 \leq \rho \leq 1 \\
D_z(\rho, \zeta = 0) &= \int_0^\infty [M_7 A_1(\xi) + M_8 A_2(\xi)] \xi J_0(\xi \rho) d\xi = 0 \quad 0 \leq \rho \leq 1 \\
\sigma_{zz}(\rho, \zeta = 0) &= \int_0^\infty [M_5 A_1(\xi) + M_6 A_2(\xi)] \xi J_0(\xi \rho) d\xi = 0 \quad \rho > 1 \\
D_z(\rho, \zeta = 0) &= \int_0^\infty [M_7 A_1(\xi) + M_8 A_2(\xi)] \xi J_0(\xi \rho) d\xi = 0 \quad \rho > 1
\end{aligned} \tag{B.15}$$

From D_z terms in Eqs. B.15 we find that $M_7 A_1(\xi) + M_8 A_2(\xi) = 0$ so then $A_1(\xi) = -\frac{M_8}{M_7} A_2(\xi)$.

The dual integral equations can be given by:

$$\begin{aligned}
\int_0^\infty A_2(\xi) J_0(\xi \rho) d\xi &= \frac{M_7(f(\rho) + b)}{M_2 M_7 - M_1 M_8} \quad 0 \leq \rho < 1 \\
\int_0^\infty A_2(\xi) \xi J_0(\xi \rho) d\xi &= 0 \quad \rho > 1
\end{aligned}$$

The solution to the above equations is the same as before,

$$A_2(\xi) = \frac{1}{\sqrt{\pi}} \sum_n \frac{\Gamma(\frac{1}{2}n + 1)}{\Gamma(\frac{1}{2}n + \frac{3}{2})} Z_n \left\{ \cos \xi + \xi \int_0^1 u^{n+1} \sin(\xi u) du \right\}$$

where as before,

$$F(\rho) = \sum_n Z_n \rho^n$$

The solutions above for $F_\alpha = K_0$, $K_1 \rho$, and $K_2 \rho^2$ can be used again with care taken as to the definitions for K_0 , K_1 , and K_2 . Let us again consider the conical punch $f(\rho) = \epsilon(1 - \rho)$. Here

K_0 and K_1 are given by:

$$K_0 = \frac{M_7(b + \epsilon)}{M_2M_7 - M_1M_8} \quad K_1 = -\frac{M_7\epsilon}{M_2M_7 - M_1M_8}$$

The expression for A_2 is the same as it was before,

$$A_2 = \left(\frac{2K_0}{\pi} + K_1 \right) \frac{\sin(\xi)}{\xi} + \frac{K_1}{\xi^2} (\cos(\xi) - 1)$$

This then can be substituted into the expression for σ_{zz} at the circle of contact $\rho = 1$

$$\begin{aligned} \sigma_{zz}(\rho = 1, \zeta = 0) &= \int_0^\infty \frac{M_6M_7 - M_8M_5}{M_7} A_2(\xi) \xi J_0(\xi) d\xi \\ \sigma_{zz}(\rho = 1, \zeta = 0) &= \int_0^\infty \left\{ \left(\frac{2K_0}{\pi} + K_1 \right) \sin(\xi) + \frac{K_1}{\xi} (\cos(\xi) - 1) \right\} \frac{M_6M_7 - M_8M_5}{M_7} J_0(\xi) d\xi \end{aligned}$$

The first term in the braces diverges but the stress is finite at this location so the constant of this term must be zero. This gives the result $b = \left(\frac{\pi}{2} - 1 \right) \epsilon$. The stress component σ_{zz} is given by:

$$\begin{aligned} \sigma_{zz}(\rho, \zeta = 0) &= \int_0^\infty \left\{ -\frac{M_6M_7 - M_8M_5}{M_2M_7 - M_1M_8} \epsilon \right\} \frac{J_0(\xi\rho)}{\xi} (\cos(\xi) - 1) d\xi \\ \sigma_{zz}(\rho, \zeta = 0) &= \left\{ -\frac{M_6M_7 - M_8M_5}{M_2M_7 - M_1M_8} \epsilon \right\} \cosh^{-1} \left(\frac{1}{\rho} \right) \end{aligned}$$

This gives a load on the indenter of,

$$P_{\text{insulator}} = \pi a^2 \epsilon \frac{M_8M_5 - M_6M_7}{M_2M_7 - M_1M_8}$$

This result also agrees with Giannakopoulos and Suresh up to a minus sign.

B.2 Summary of differences

A summary of the differences between the results of Giannakopoulos [111] and the present study are shown below.

- Differences in the values of a_{ij} in matrix, Eq. (14) in [111]

There is disagree on the sign of some of the terms of the a matrix but it does not make a difference in the results. When the $|a|$ is set equal to zero, the same result up to a minus sign is obtained.

- Differences in the values of the terms m_1 , m_2 , m_3 , and M_7

The difference in the m_1 term is that there is a k in the first term that should not be there. This is probably just a typographical error. The differences in m_2 and m_3 are shown in Table

B.1. This is probably not a typographical error and this difference will effect most all results that are obtained after this. Finally there is sign difference on the M_7 term which will effect some of the results for ZnO.

	m_2	m_3
Giannakopoulos [111]	$-e_{15} (\delta\gamma_{21} - \omega\gamma_{22})$ $-c_{44} (\delta\alpha_{21} - \omega\alpha_{22} + \beta_{21})$	$-e_{15} (\delta\gamma_{22} + \omega\gamma_{21})$ $-c_{44} (\delta\alpha_{22} + \omega\alpha_{21} + \beta_{22})$
This work	$-e_{15}\gamma_{21} - c_{44} (\delta\alpha_{21} - \omega\alpha_{22} + \beta_{21})$	$-e_{15}\gamma_{22} - c_{44} (\delta\alpha_{22} + \omega\alpha_{21} + \beta_{22})$

Table B.1: Differences in the terms m_2 and m_3 of Giannakopoulos [111] and this work.

#2

VITA

Matthew Joseph Klopstein

Candidate for the Degree of

Doctor of Philosophy

Thesis: INVESTIGATION OF THE NEAR SURFACE MECHANICAL BEHAVIOR OF SINGLE CRYSTAL ZnO BY NANOINDENTATION

Major Field: Mechanical Engineering

Biographical:

Personal Data: Born in Columbus, Ohio July 18, 1968, son of Joseph M. and Joyce N. Klopstein.

Education: Graduated from Worthington High School, Worthington, Ohio, 1986; Bachelor of Science in Mechanical Engineering from The Ohio State University, Columbus, Ohio, 1991; Master of Arts in Economics from The Ohio State University, Columbus, Ohio, 1992; Master of Science in Mechanical Engineering, Oklahoma State University, Stillwater, Oklahoma, 1997. Completed the requirements for the Doctor of Philosophy degree with a major in Mechanical Engineering at Oklahoma State University in December, 2004.

Professional Memberships: Student member of the American Society for Precision Engineering, member of Sigma Xi